eman ta zabal zazu

Universidad del País Vasco
Euskal Herriko Unibertsitatea

Electronic Tailoring of Graphene Nanostructures via On-Surface Synthesis

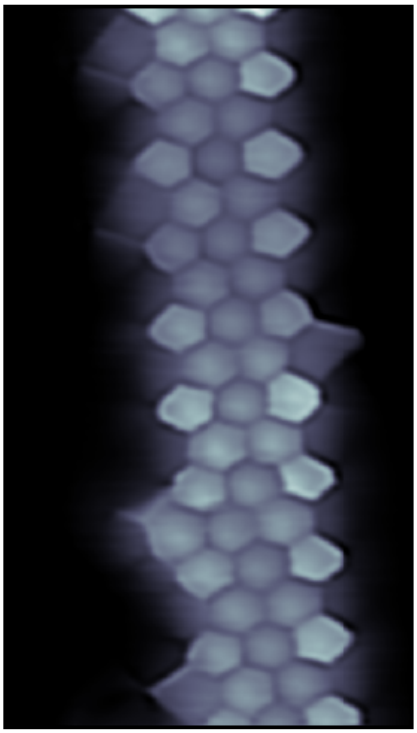

DOCTORAL THESIS

by Eduard Carbonell Sanromà

Supervised by José Ignacio Pascual Chico

Donostia, May 2016

This thesis has been carried out at CIC nanoGUNE

Als meus avis i iaios

Abstract

This thesis presents a thorough study on the electronic properties of several types of graphene nanoribbons (GNRs) produced by on-surface synthesis strategies on gold surfaces. The research has been performed mainly by Low Temperature Scanning Tunneling Microscopy and Spectroscopy (LT-STM/STS) in ultra high vacuum conditions. These results were obtained in collaboration with the group of Prof. Daniel Sánchez-Portal who performed first principle Density Functional Theory calculations. The novel molecular precursors used in this thesis were synthesized by the group of Prof. Diego Peña and the group of Yamaguchi-Sensei.

GNRs are a new class of material combining many of the superlative qualities of graphene with unique electronic properties arising from their nanometric dimensions. The presence of a tunable electronic bandgap or low dimensional magnetism is intrinsically related to the width and edge structure of the ribbon down to the atomic scale. In order to achieve atomic precision in the structure of the ribbons, we grow our ribbons using specially designed molecular precursors as building blocks. The reaction of the precursors is catalyzed by the metal surface and leads to ribbons with very low density of defects. This on-surface approach produced model systems that facilitate the study of the electronic properties of 7 armchair graphene nanoribbons (7-AGNRs), two chemically modified 7-AGNR species and hybrid ribbons combining pristine and boron modified 7-AGNR sections.

Two strategies were followed to chemically modify 7-AGNRs: using substitutional nitrile functional groups at the edges and using substitutional boron atoms within the backbone of the ribbon. The 7-AGNR species modified with edge cyano (CN) groups presented a case study of the use of functional groups to modify the electronic properties of GNRs. The strong electron withdrawing character of CN groups induced a charge redistribution within the ribbon backbone, leading to a very efficient n-like doping of the ribbon. The substitution of boron atoms within the backbone of 7-AGNRs backbone highlighted additional consequences of doping ribbons with other chemical species. On the one hand, the electronic structure was heavily modified by the appearance of a new acceptor band. On the other hand, the boron atoms lead to a higher ribbon-substrate interaction producing a buckling of the ribbon structure and a hibridization of the new acceptor band with gold's surface bands.

Another adopted strategy was the combination of pristine and chemically modified 7-AGNRs precursors to construct hybrid GNRs and GNR heterostructures. By combining boron substituted and pristine 7-AGNRs we embedded quantum wells within the pristine sections of the hybrid ribbons. The boron substitutes acted as very efficient scatterers of the pristine 7-AGNR valence band, selectively confining this band but leaving unaffected the band below.

Finally, we show the on-surface synthesis of other graphene nanostructures. Particularly, we demonstrated a new on-surface route to create benzoazulene moieties within the structure of a [18]annulene based polycyclic aromatic hydrocarbons. The benzoazulenes, which play a key role in the planarization of the molecule, resulted from two conjoined bay regions in the reacted molecular precursors. Moreover, the [18]annulene core was found to host peculiar pore localized states, which we associate to super atom molecular orbitals.

Resumen

Esta tesis presenta un estudio exhaustivo de las propiedades electrónicas de diversas clases de nanocintas de grafeno (GNRs) producidas mediante métodos de síntesis en superficie de oro. El estudio de estas cintas ha sido realizado mediante Microscopía y Espectroscopía de Efecto Túnel a bajas temperaturas (LT-STM/STS) y en condiciones de ultra alto vacío. Estos resultados fueron obtenidos en colaboración con el grupo del Prof. Daniel Sánchez-Portal, que realizó cálculos ab initio de Teoría del Funcional de la Densidad (DFT). Los nuevos precursores moleculares usados en esta tesis fueron sintetizados por el grupo del Prof. Diego Peña y el grupo de Yamaguchi-Sensei.

Los GNRs son una nueva clase de material que combina muchas de las cualidades superlativas del grafeno con propiedades únicas que emergen de sus dimensiones nanométricas. La presencia de un gap ajustable o de un magnetismo de baja dimensionalidad está intrínsecamente relacionada al ancho y la estructura de borde de la nanocinta al nivel atómico. Las nanocintas con borde de tipo zigzag (ZGNRs) se caracterizan por la presencia de estados de borde con spin polarizados. Las nanocintas con borde de tipo armchair (AGNRs) se caracterizan por su comportamiento semiconductor. En los AGNRs el bandgap se abre debido a la discretización de las bandas del grafeno. Además, el bandgap de la nanocinta decrece al incrementar el ancho de la cinta, lo que permite un cierto grado de ajuste de sus propiedades electrónicas. Es importante recalcar que las propiedades de las cintas están estrechamente ligadas a la perfección y precisión de su red cristalina, y que por tanto, la presencia de unos pocos defectos o imprecisiones degrada rápidamente las propiedades esperadas de cada cinta.

Para conseguir un alto grado de control en la estructura de los GNRs, crecemos nuestras cintas usando precursores moleculares específicamente diseñados para actuar como bloques básicos de construcción. Las nanocintas resultantes, con una estructura precisa a la escala atómica, se obtienen mediante la activación de reacciones catalizadas

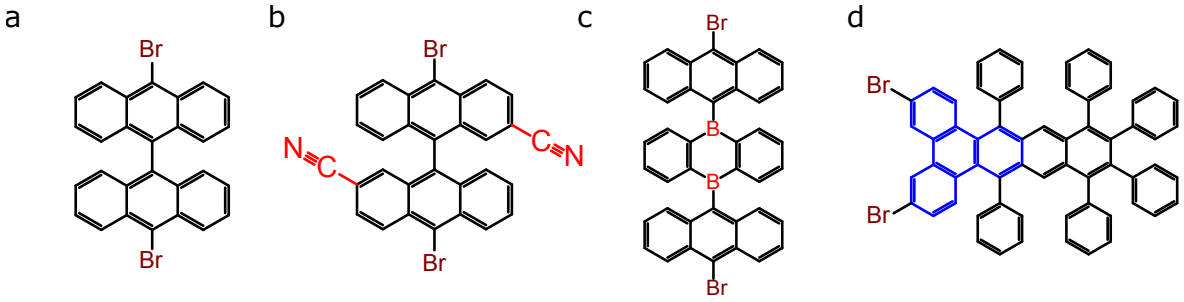

Figure 1: Estructuras químicas de los precursores usados para crecer (a) 7-AGNRs, (b) CN-7-AGNRs, (c) 2B-7-AGNRs y (d) trímeros con grupos bisazulenos.

por la superficie, típicamente oro. Las reacciones usadas en esta tesis se basan en el acople Ullmann de los precursores, donde después de una dehalogenación catalizada por la superficie, se enlazan dos precursores formando un enlace C-C. El paso subsiguiente se basa en la planarización de los polimeros formados mediante la eliminación del exceso de hidrógeno de las cadenas poliméricas. Esta reaccion, llamada ciclodeshidrogenación, reduce el estrés estérico de los polímeros, mendiante la rotura de enlaces C-H y la creación de enlances C-C, planarizando los polímeros y llegando a estructuras de GNRs atómicamente precisas.

Este método de síntesis en superficie ha producido sistemas modelo que facilitaron el estudio de las propiedades electrónicas de las nanocintas de grafeno armchair de ancho 7 (7-AGNRs), dos especies de 7-AGNR modificados químicamente y nanocintas híbridas

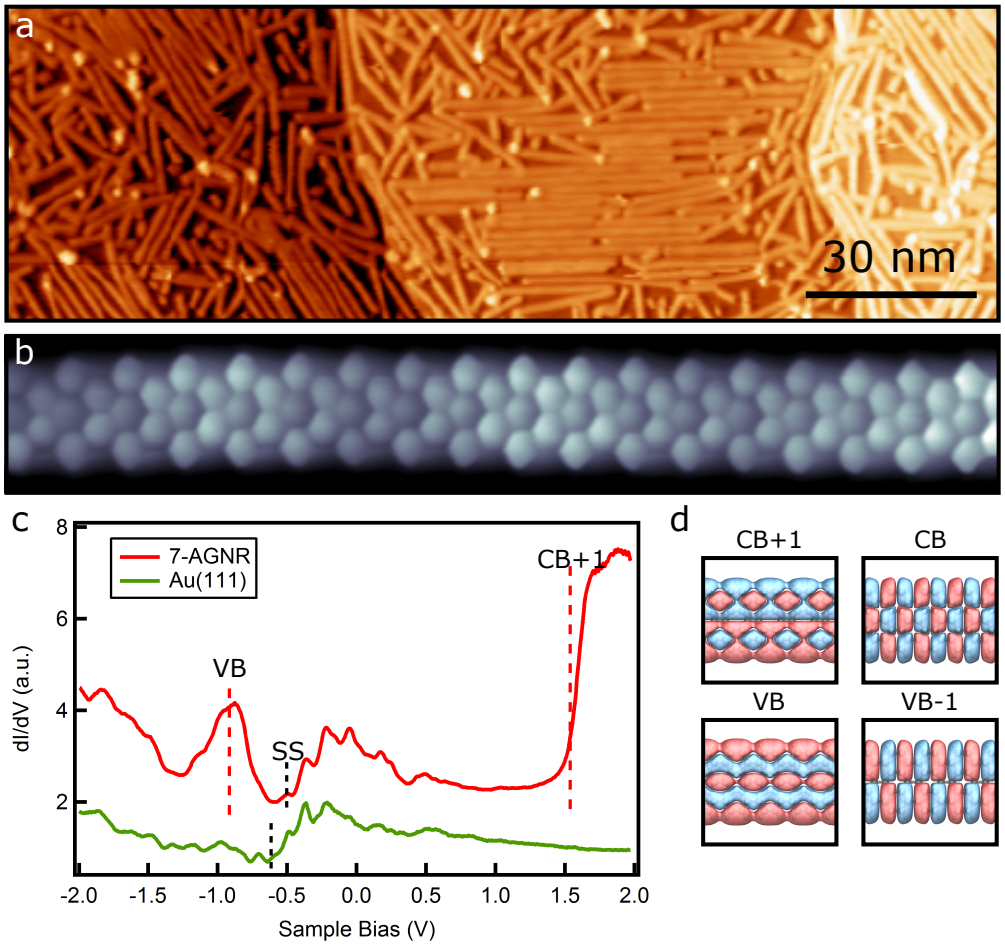

Figure 2: (a) Imagen STM mostrando una muestra con alto recubrimiento de 7-AGNRs. (b) Imagen de STM con punta de CO de un 7-AGNR, mostrando su estructura molecular. Las nanocintas crecidas tienen longitudes de decenas de nanometros sin defectos. (c) Espectro STS de un 7AGNR (rojo) y el sustrato de oro de referencia (verde). Las líneas discontinuas rojas marcan las señales correspondientes a la banda de valencia y la banda de conducción +1. Las líneas discontinuas negras muestran el inicio del estado de superficie del Au(111). (d) Funciones de ondas de las distintas bandas de un 7-AGNR, mostrando sus simetrías.

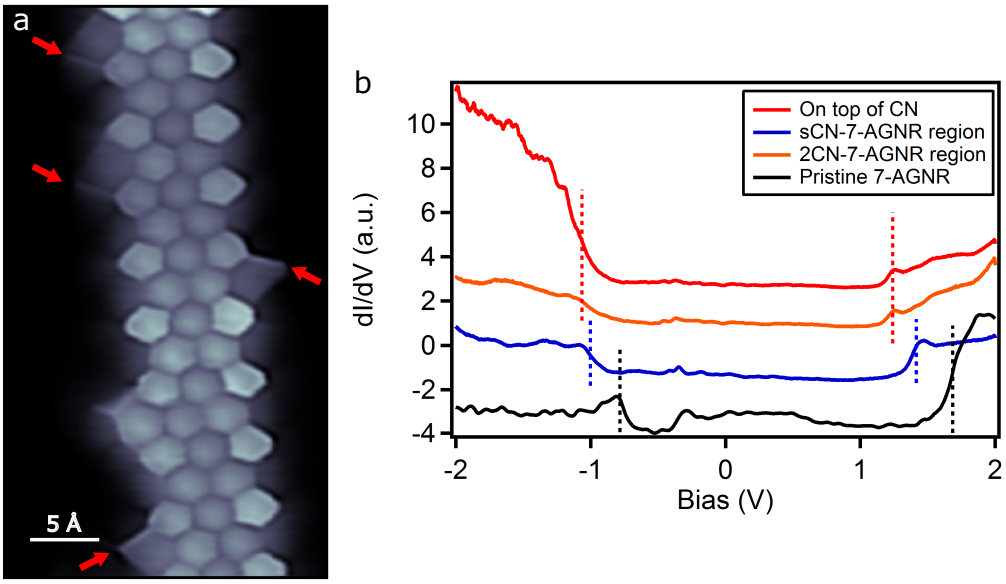

Figure 3: (a) Imagen de STM con punta de CO de un CN-7-AGNR, mostrando la estructura intramolecular del mismo .Las flechas rojas indican la presencia de grupos funcionales CN en los bordes de la nanocinta. (b) Espectro STS de un CN-7-AGNR en distintas posiciones de la nanocinta. En las posiciones con solo un CN, el dopaje n observado es menor que en las zonas con CN en ambos bordes. En negro se muestra un espectro de referencia para un 7-AGNR pristino.

crecidas mediante la combinación de secciones prístinas y secciones modificadas con boro.

Primeramente se estudió las nanocintas 7-AGNR pristinas, que se usaron como referencia a lo largo de todo este trabajo. Durante el crecimiento de muestras con alto recubrimiento se observó la fusión lateral de nanocintas, generando heteroestructuras de distintos anchos. Estas fusiones laterales se pueden incrementar calentando la muestra a temperaturas más elevadas. El proceso carece de control y en ocasiones se observaron cadenas de protusiones entre dos cintas no fusionadas. Proponemos que las protusiones son debidas a adatomos de oro atrapados entre las nanocintas. Además de su crecimiento, se describió ampliamente la estructura electrónica de los 7-AGNRs. Cocretamente, la espectroscopia STS de los 7-AGNR solo muestrea la banda de conducción +1 y la banda de valencia, debido a la simetría de la función de onda de las bandas de conducción y valencia -1.

En segundo lugar se usaron grupos funcionales de nitrilo substituidos en los bordes de las nanocintas. Este experimento sirvió como escenario base para estudiar el uso de grupos funcionales para modificar la estructura electronica de los 7-AGNRs. Las nanocintas resultantes presentaban en general la estructura deseada. Aun así, la observación de las cintas con puntas funcionalizadas con CO reveló la pérdida de grupos CN durante la reacción en superficie. Además, observamos ocasionalmente la cicloisomerización de grupos nitrilos , una reacción en superficie no citada hasta la fecha. En lo que respecta a las propiedades electronicas de los CN-7-AGNR, el fuerte carácter acceptor de los grupos CN indució una redistribución de la carga en el cuerpo principal de la nanocinta. Como resultado, el potencial electrostático de las nanocintas sufrió

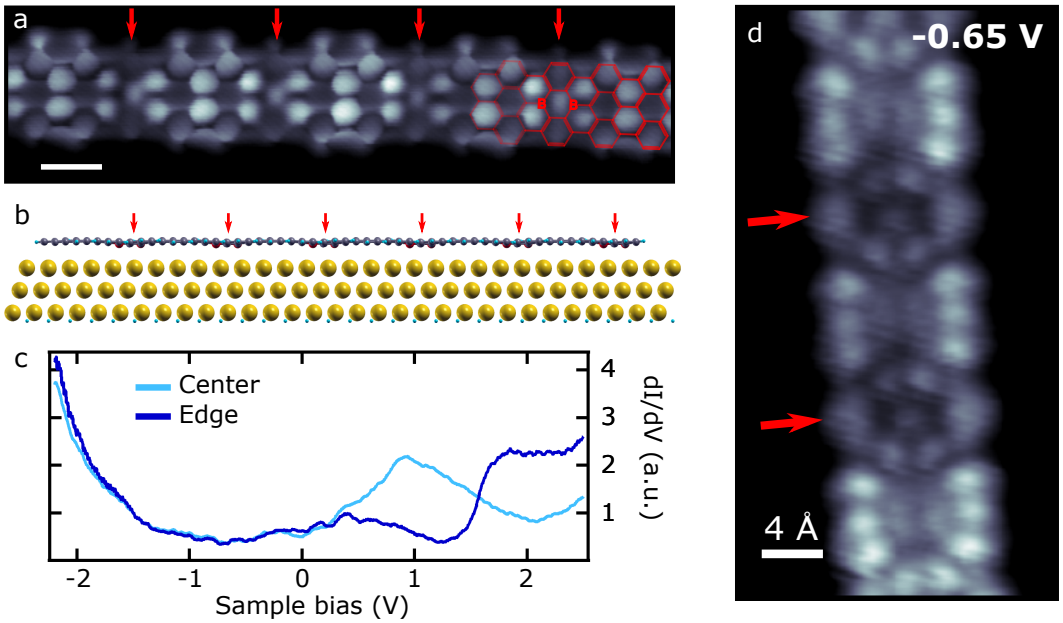

Figure 4: (a) Imagen de STM con punta de CO de un 2B-7-AGNR. En rojo se muestra la estructura molecular. (b) Estructura relajada mediante DFT de un 2B-7-AGNR encima de una losa de Au(111). La mayor interacción de la cinta con el oro genera una corrugación de la estructura. (c) Espectros STS de un 2B-7-AGNR, mostrando la banda aceptora en el centro de la nanocinta, que en contraste, no se observa en los bordes del 2B-7-AGNR. (d) Mapa espectroscópico de la banda de valencia de un 2B-7-AGNR, mostrando la forma de la densidad de estados local de esta banda. Las flechas rojas de los paneles *a*, *b* y *d* marcan las posiciones de los pares de boro.

una bajada con respecto a los 7-AGNRs, lo que incrementa la electronegatividad de la nanocinta. Así pues, los grupos funcionales nitrilo actuan como dopantes de tipo n en las nanocintas de grafeno.

La siguiente estrategia se centró en introducir átomos de boro en el cuerpo de un 7-AGNR. Debido a la mayor interacción entre cinta dopada y sustrato, la estructura de los 2B-7-AGNRs aparece corrugada. El cambio más prominente en la estructura electrónica de las cintas fue la introducción de una banda aceptora dentro del gap del GNR. Detectamos la banda de valencia de estas nanocintas, no observada hasta la fecha, combinando medidas de ARPES y STS. Eso nos permitió determinar el bandgap experimental de los 2B-7-AGNR. La mayor interacción entre cinta y sustrato tambien tuvo como consecuencia la hibridización de la banda aceptora con las bandas de la superficie. Estos resultados podrían ser relevantes para nanocintas modificadas químicamente, crecidas o transferidas a sustratos más reactivos.

Por otro lado, la mezcla de precursores nanocintas de grafeno pristinas y modificadas con boro permitió crecer nanocintas híbridas y heteroestructuras en los GNRs. En particular se observó el confinamento de la banda de valencia de los segmentos 7-AGNR pristinos encapsulados entre segmentos borinados. Los pares de átomos de boro actuaron como dispersores muy eficientes de la banda de valencia, mientras que la banda por debajo no se vió afectada. Los cálculos DFT mostraron que el origen de la selectividad en el confinamiento es debido a las distintas simetrias de las bandas de

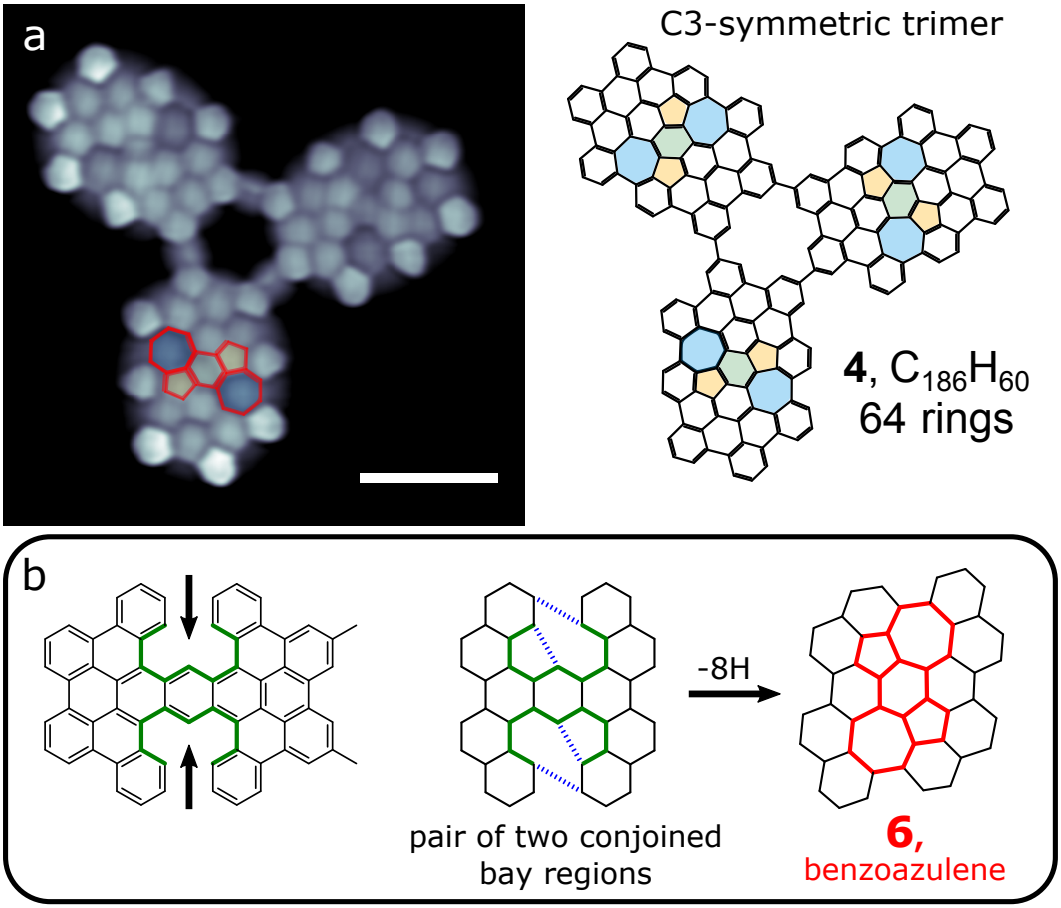

Figure 5: (a) Imagen de STM con punta de CO resolviendo la estructura intramolecular de un hidrocarburo policíclico aromático (PAH) de gran tamaño sintetizado por estrategias en superficie. En rojo se marca la estructura de un bisazuleno, componente clave para la planarización de este compuesto. A su lado se muestra la estructura química del PAH. (b) (b) Proceso de planarización del trímero. En verde se subrayan las regiones de bahía causantes de la formación del benzoazuleno.

la nanocinta pristina y los estados localizados de los segmentos borinados.

Finalmente, mostramos la síntesis en superficie de otras nanoestructuras de grafeno. En particular, demostramos una nueva ruta en superficie para crear grupos benzoazuleno dentro de la estructura de un hidrocarburo aromático policíclico basado en el [18]anuleno. Los benzoazulenos, los cuales juegan un papel crucial en la planarización de la molécula, resultaron de las regiones de bahía conjuntas presentes en los precursores moleculares reaccionados. Además, se observó que el núcleo [18]anuleno albergaba estados de poro localizados que asociamos a orbitales moleculares súper atómicos.

Acronyms and notation

AB	Acceptor Band
n-AGNR	n Armchair Graphene Nanoribbon
ARPES	Angle Resolved Photoemission Spectroscopy
Au	Gold
CB	Conduction Band
CN	Cyano
CO	Carbon monoxide
DBBA	10,10'-dibromo-9,9'-bianthryl
dI/dV	Differential conductance
2CN-DBBA	10,10'-dibromo-[9,9'-bianthracene]-2,2'-dicarbonitrile
2B-DBBA	9,10-bis(10-bromoanthracene-9-yl)-9,10-dihydro-9,10-diboraanthracene
DFT	Density Functional Theory
DOS	Density of States
E_F	Fermi Energy
f	Lock-in frequency
FC	Feedback Conditions
FT	Fourier Transform
GNR	Graphene Nanoribbon
GW	Green's Wavefunction Approximation
HOMO	Highest Occupied Molecular Orbital
I_t	Tunneling current
LDOS	Local Density of States
LDA	Local Density Approximation
LUMO	Lowest Unoccupied Molecular Orbital
OFC	Open Feedback Conditions
PDOS	Projected Density of States
QW	Quantum Well
STM	Scanning Tunneling Microscopy
STS	Scanning Tunneling Spectroscopy
UHV	Ultra High Vacuum
VB	Valence Band
V_s	Sample bias
V_{rms}	Lock-in oscillation amplitude
ZGNR	Zigzag Graphene Nanoribbon

Contents

Abstract **v**

Acronyms and notation **xiii**

Introduction **1**

1 The Experimental Techniques **5**
1.1 Scanning Tunneling Microscope principles 5
1.2 Intramolecular resolution with functionalized tips 9
1.3 The experimental setup 14

I Introduction to Graphene Nanoribbons **17**

2 Electronic Properties of Pristine Graphene Nanoribbons **21**
2.1 Armchair Graphene Nanoribbons 22
2.2 Zigzag Graphene Nanoribbons 25
2.3 Graphene Nanoribbons under Clar's Theory 28
2.4 Growth of Graphene Nanoribbons 31
2.5 Conclusions 33

3 Pristine 7-AGNR, a case study **35**
3.1 On-surface growth of 7-AGNRs on Au(111) 35
3.2 Electronic structure of 7-AGNR 41
3.3 Conclusions 45

II Doping of Graphene Nanoribbons **47**

4 Doping of Graphene Nanoribbons via Functional Group Edge Modification **51**
4.1 Growth of CN functionalized 7-AGNR 52
4.2 ***n***-like doping induced by CN groups 54
4.3 Conclusions 59

5 Role of substrate interactions in boron substituted 7-AGNR **61**
5.1 Growth of 2B-7-AGNR 62

5.2 Electronic structure and substrate-ribbon hybridization 63
5.3 Conclusions 69

6 Quantum dots embedded in hybrid 7-AGNR 71
6.1 Electronic properties of hybrid 7-AGNR 73
6.2 Confinement of the Valence Band 75
6.3 Electronic transport through a hybrid 7-AGNR 79
6.4 Conclusions 82

III On-surface synthesis of graphene nanostructures 83

7 On-surface synthesis of a chevron decorated ribbon 87

8 On-surface route for producing planar nanographenes with benzoazulene moieties 93
8.1 Synthesis of an [18]annulene based PAH 93
8.2 Planarization via benzoazulene formation 95
8.3 Electronic structure and pore states 97
8.4 Conclusions 101

9 Conclusions and Outlooks 103

References 117

Publications i

Acknowledgments iii

Introduction

Graphene is often regarded as a revolutionary material due to its many outstanding properties [1]. It is the thinnest, lightest and strongest material known, its stiffness is only surpassed by diamond and it is the material with the highest thermal conductivity known. Graphene has also the highest electron mobility, which origins from its unique electronic structure. As a result, graphene is envisioned as a base material for electronic devices. However, the absence of an electronic bandgap limits its use in logic applications. Many strategies have been concieved to open a bandgap in graphene. A method to achieve this purpose is creating graphene nanostructures, particularly Graphene Nanoribbons (GNRs).

GNRs are one dimensional stripes of graphene with edges typically, but not necessarily, passivated by hydrogen. GNRs potentially share many of their physical properties with graphene while their nanometer sized dimensions opens a bandgap and provides them with unique electronic properties. The miniaturization of graphene into these 1D structures changes the electronic structure not only due to finite size effects, but also from the addition of edges to the graphene sheet. The structure of these edges has a major impact on the properties of the resulting ribbons. There are two main types of GNRs depending on their edge structure, armchair and zigzag GNRs. Zigzag GNRs (ZGNRs) are gapless and host spin polarized edge states, while armchair GNRs (AGNRs) are majoritarily semiconductors and do not possess edge states [2]. GNRs can be envisioned as materials capable to overcome the main drawbacks of graphene in semiconductor and spintronic applications.

The properties of GNRs are deeply dependent on the atomic structure, ordering and defect density of their lattice [3, 4]. Therefore, the growth strategies for these materials require an almost atomic precision, which is not available in common top-down fabrication techniques. A more accurate approach is to use molecular precursors as building blocks to grow GNRs via on-surface reactions. This bottom-up fabrication process grants the selectivity needed to construct GNRs with well defined edges, widths and lattices, and as a result, well defined properties. The first graphene nanoribbon synthesized following this on-surface approach, the 7-AGNR [5], served as foundation for a myriad of experimental and theoretical works concerning GNRs and their potential applications.

Resembling bulk semiconductors, GNRs can be doped by introducing heteroatoms within their structure. The on-surface synthesis approach allows to incorporate with atomic precision dopant species in the ribbon lattice. This potentially translates in remarkable tuning possibilities for GNRs. However, it is worth noting that the impurity density achieved via this process is typically of the order of a few percent, which is several orders of magnitude higher than usual doping densities in bulk semiconductors.

Thus a thorough study of the effects and consequences of doping in GNR is necessary to achieve a real control on their electronic properties. A further parallelism with bulk semiconductors lays on GNRs heterojunctions. The combination of different molecular precursors of GNRs with distinct electronic properties has lead to p-n junctions [6], Type I heterojunctions [7] and embedded quantum dots [8]. These results bring GNRs a step closer to their proposed semiconductor and optoelectronic applications.

Low Temperature Scanning Tunneling Microscopy and Spectroscopy (LT-STM/STS) are very powerful techniques to study GNRs. Through specific functionalization of the STM tips, they achieve true atom and bond resolution. This allows us to determine the success of the GNR on-surface synthesis down to the atomic scale, which is essential to ensure the characteristic properties of these nanostructures. Moreover, the ability to locally probe the electronic structure of GNRs is invaluable to understand their electronic properties. In addition, the Ultra High Vacuum (UHV) equipment and the low temperature of the microscope stage (5 K) provides a controlled environment for the required on-surface reactions and the following spectroscopic investigation.

The interest on the on-surface synthesis approach also goes beyond the building of GNRs. Many polycyclic aromatic hydrocarbons (PAH) hold interest in the field of organic electronics. Solution synthesis has been succesfully employed to obtain PAHs with fascinating structures and functionalities following a bottom-up approach. However, the large size and the extremely low solubility of these molecules severely complicates their manipulation and characterization. STM and Atomic Force Microscopy are privileged tools to study insoluble nanographenes prepared by solution chemistry but they require the sublimation of the material on an adequate surface, which limits the size of the molecules that can be studied. Synthesizing these large molecules using on-surface reactions of smaller building blocks circumvents these limitations, allowing to study and characterize new graphene based nanostructures.

This thesis focuses on the LT-STM study of the electronic properties of AGNRs synthesized by on-surface processes. In particular we explore the doping of AGNRs and the underlying physics behind their different electronic properties. The majority of our work is reinforced with first principle DFT calculations, which allow us to further explore the physical insights of these nanostructures. The last chapters of this work steer away from GNRs, providing insights on new on-surface routes to synthesize large planar PAHs.

Outline

The contents of this thesis are organized as follows:

Chapter 1 introduces LT-STM and STS as experimental techniques. Special focus is given on the intramolecular resolution achieved with functionalized tips.

Part I serves as a review of the state of the art knowledge of graphene nanoribbons and their on-surface synthesis.

Chapter 2 gives a formal approach to the electronic properties of GNRs from a tight binding approach and also from the point of view of Clar's Theory. Finally, the on-surface synthesis process to grow GNRs is thoroughly explained and reviewed.

Chapter 3 focuses on the growth and electronic properties of 7-AGNR, which serves as reference framework for all the ensuing chapters.

Part II is devoted to the study of doping of 7-AGNRs via chemical modification.

Chapter 4 exhibits the n like doping induced by CN edge functionalized 7-AGNR using a novel molecular precursor.

Chapter 5 focuses on the electronic structure of boron substituted 7-AGNRs, highlighting the role of the ribbon-substrate interactions in the GNR's electronic properties.

Chapter 6 showcases the embedding of quantum dots within hybrid 7-AGNR grown by combining pristine and boron 7-AGNR precursors.

Part III shows the growth of other graphene nanostructures using two novel molecular precursors, with particular focus in their reaction process.

Chapter 7 describes the growth of a chevron decorated ribbon.

Chapter 8 highlights the synthesis of a large [18]annulene based PAH, planarizing through a novel on-surface route.

Chapter 9 Summarizes the results presented in this thesis, providing outlooks and perspectives for further research.

Contributions by others

The majority of the work here presented is the outcome of a collaborative effort of different research groups and people. All first principle DFT calculations of chapters 3 to 8 have been carried out by Dr. Pedro Brandimarte, Dr. Aran García-Lekue in the group of Dr. Daniel Sánchez-Portal. The novel molecular precursors used in chapter 4, 7 and 8 were synthesized by Manuel Vilas-Varela, in the group of Prof. Enrique Guitián, Prof. Dolores Pérez and Prof. Diego Peña. The molecular precursor used in chapters 5 and 6 was synthesized by Shohei Saito-Sensei in the group of Shigehiro Yamaguchi-Sensei. The ARPES measurements provided in Chapter 5 were done by Dr. Guillaume Vasseur, Prof. Jorge Lobo-Checa and Prof. Dimas García de Oteyza in the group of Prof. Enrique Ortega.

The STM data of this thesis has been mainly obtained by myself, however many coworkers were present and supported me during the course of the experiments involved in each chapter: Dr. Martina Corso, Dr. Richard Balog, Dr. Jeremy Hieulle, Dr. Jincheng Li, Ms. Ana Barragán, Dr. Shigeki Kawai, Mr. Mikel Iraola and Mr. Maciej Topyla. It is by our conjoined effort that I'm able to present these results.

Chapter 1

The Experimental Techniques

At the time of its design in 1982, the Scanning Tunneling Microscope (STM) allowed an unprecedented resolution of the topography of a flat sample [9]. One year later, the atomic resolution provided by the STM allowed to solve the mystery behind the 7×7 surface reconstruction of Si(111), one of the most intriguing problems in surface science at that time [10]. Shortly thereafter, the developers of the STM, Gerd Binning and Heinrich Rohrer, were granted the Physics Nobel Prize for their invention.

More than thirty years later, the STM has become a staple tool in surface science. Its working principle, the quantum tunneling effect, enables to locally probe not only the topography of a substrate or molecule, but also its electronic structure. Moreover, the synergistic combination of STM with UHV and low temperature equipments has led to the manipulation of single atoms [11] or molecules and the study of their electronic, vibrational and magnetic properties at the atomic scale.

In this chapter we are going to review the basic principles of the STM technique, some particular measurement methods and the experimental setup used during the course of this thesis.

1.1 Scanning Tunneling Microscope principles

The STM is based in the tunneling effect, a quantum mechanical phenomenon in which electrons have a probability to overcome a potential barrier that, classically, would be forbidden. In a STM, the potential barrier is the vacuum between the two metallic electrodes, tip and sample. By applying a voltage (V_T) between the electrodes we introduce a relative shift (eV_T) between the Fermi energies of the metals (Figure 1.1a), defining a trapezoidal tunneling barrier. The probability for an electron from the tip ($z = 0$) to tunnel to the sample (at position z) can be then described as [12]:

$$|\psi(z)|^2 = |\psi(0)|^2 e^{-2\kappa z} \quad , \quad \kappa = \sqrt{\frac{m_e}{\hbar^2}(\Phi_t + \Phi_s - eV_T)} \tag{1.1}$$

where $\psi(0)$ and $\psi(z)$ represent the electron wavefunction at positions 0 and z. κ represents the decay rate of the wavefunction inside the tunneling barrier (Figure 1.1a), m_e is the electron mass, $\hbar$ is the reduced Planck constant and Φ_t and Φ_s are the tip and metal workfunctions respectively. The exponential dependence of the tunneling probability is the reason behind the extreme z sensitivity of the STM, i.e. variations

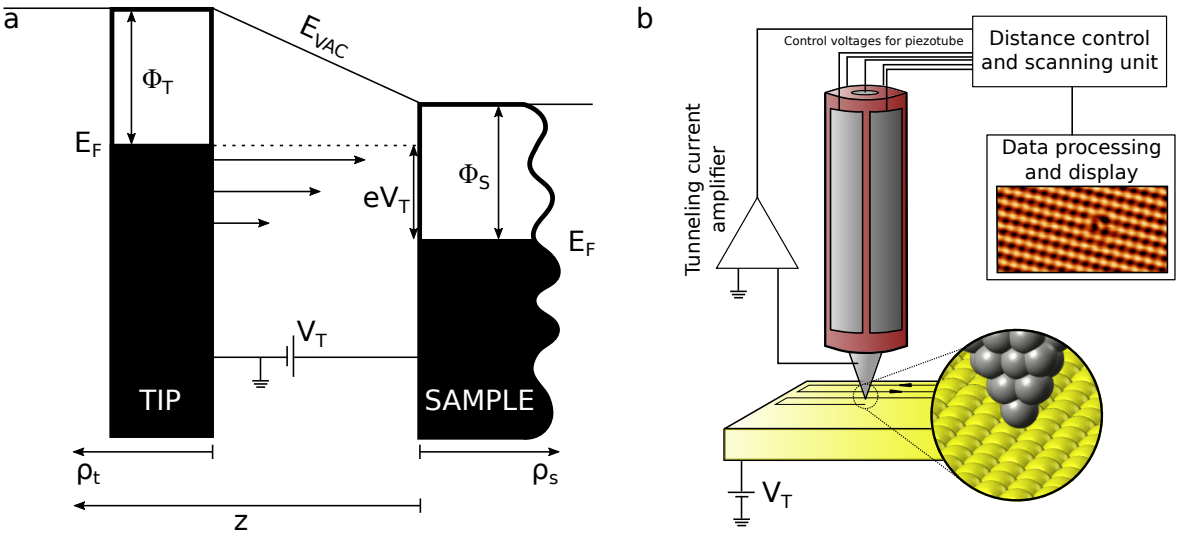

Figure 1.1: (a) STM tunnel junction energy diagram for a positive bias voltage V_T applied to the sample. Electrons tunnel from filled states of the tip (with an ideal flat LDOS ρ_t) to empty states of the sample with a LDOS ρ_t. The arrows depict the probability of a tunneling event to occur described by the transmission $T(z, E, eV)$. T normally peaks at E_F of the tip, when $V > 0$, and at E_F of the sample when $V < 0$. This implies that probing the unoccupied states of the sample is typically easier than probing the occupied states. (b) Schematic illustration of an STM experimental setup. The tip is scanned over the sample using piezoelectric elements while recording the tunneling current. The feedback adjusts the position of the tip to maintain a constant tunneling current. Finally, the tip trajectories are processed and displayed on a computer screen.

in tip-sample distance of 1 Å typically result in an order of magnitude change in the tunneling probability.

Beyond this one dimensional representation, one of the most used approaches to describe the tunneling current between two metals is the formalism developed by Bardeen [13]. Within it, tip and sample are treated as separate, unperturbed entities with states ψ_ν and ψ_μ respectively, and the approach between the electrodes is considered as a perturbation potential. The first-order expression for the tunneling current is:

$$I = \frac{2\pi e}{\hbar} \sum_{\mu,\nu} \{f_t(E_\nu - eV_T)[1 - f_s(E_\mu)] - [1 - f_t(E_\nu - eV_T)]f_s(E_\mu)\} \times |M_{\mu\nu}|^2 \delta(E_\mu - E_\nu) \tag{1.2}$$

where $f(E)$ is the Fermi distribution function, E_μ and E_ν are the energies of the states ψ_μ and ψ_ν. The tunneling current occurs between filled states of the tip to empty states of the sample as represented by the factor containing the Fermi distributions. The δ function ensures energy conservation, and thus only elastic tunneling processes are taken into account. $M_{\mu\nu}$ is the transition matrix element between states ψ_μ and ψ_ν, given by [13]:

$$M_{\mu\nu} = -\frac{\hbar^2}{2m_e} \int_S d\mathbf{S}(\psi_\mu^* \nabla\psi_\nu - \psi_\nu \nabla\psi_\mu^*) \tag{1.3}$$

where the integral is over the surface separating tip and sample within the tunneling junction. The finite summation of discrete states in equation 1.2 can be substituted for the integral over the energy using the concept of density of states [14]:

$$I = \frac{2\pi e}{\hbar} \int_{-\infty}^{\infty} \rho_t(E - eV_T)\rho_s(E)[f_t(E - eV_T) - f_s(E)] \times |M(E)|^2 dE \tag{1.4}$$

where ρ_t and ρ_s are the density of states of tip and sample respectively. Equation 1.4 can be simplified by approximating the Fermi Dirac distributions to step functions in the limit of $T = 0$ (also if $k_B T$ is smaller than the energy resolution):

$$I = \frac{2\pi e}{\hbar} \int_{E_F}^{E_F + eV_T} \rho_t(E - eV_T)\rho_s(E)|M(E)|^2 dE \tag{1.5}$$

Thus the tunneling current basically depends on the density of states of tip and sample in the given energy window. However, the determination of M is a daunting task since it does not only depend on the geometrical positions of the atoms of the tip and the sample but also on their wavefunctions at given energies. These parameters are usually unknown, but Tersoff and Hamann provided a solution by considering a model tip [15]. In this simplified representation, the only contribution to the tunneling current origins from the outermost tip atom, described by a spherical *s*-like orbital. Within this approximation, and for small biases, the transition matrix element can be evaluated and the tunneling current is given by:

$$I = \frac{32\pi^3 e^2 \Phi^2 R^2 V_T}{\hbar \kappa^4} e^{2\kappa R} \rho_t(E_F)\rho_s(\mathbf{r}_0, E) \tag{1.6}$$

where R is the curvature radius of the tip and $\mathbf{r}_0$ is the position of the center of curvature of the tip, i.e. the center of the outermost atom of the tip. Thus, for small biases the tunneling current is linearly dependent on the bias and the density of states of tip and sample. This result points out that the STM can be used not only to image the topography of a sample but also to probe its electronic structure.

STM imaging

As previously shown, the tunneling current depends exponentially on the tip-sample distance. Therefore, scanning the tip over the sample results in changes in the current that can be translated to the corrugation of the surface. In order to obtain STM images, the tip is scanned in the XY plane by using a set of piezoelectric electrodes that allow controlling the tip position with picometer precision (Figure 1.1b). The typical imaging method, the constant current mode, consists on keeping the tunneling current in a feedback loop and adjusting the tip-sample distance in order to maintain a defined tunneling current set-point. Therefore, the scanned image is a constant surface defined by the applied bias V_T and the DOS of the tip and sample integrated between $E_F + eV_T$ and E_F, as defined by equation 1.5. In the case of many metallic substrates, with approximately constant DOS close to the Fermi level, the image corresponds to the actual topography of the surface. However in the case of molecules or other adsorbates,

their constant current image is tipically a convolution of their structure and their DOS shape [16].

Another imaging mode is the constant height mode, in which the tip is scanned over the sample without feedback, at a fixed height and bias. The tunneling current is then recorded to produce the image. This method is tipically used to record spectroscopic maps in small flat areas, since the obtained signal tends to appear less convoluted with the topographic features of the sample [17, 18]. It is also the preferred imaging mode when resolving the atomic structure of molecules using CO functionalized tips, either by using Non Contact Atomic Force Microscopy [19] (NC-AFM) or plain STM, as described later in this chapter.

Scanning Tunneling Spectroscopy

The sensitivity of the STM to the DOS opens the possibility to obtain spectroscopic information from both the occupied and empty states of the sample. Combined with the extremely local character of the tunneling process, the STM is a powerful tool capable of mapping the LDOS with atomic resolution.

Starting from a more general form of equation 1.5 [20, 21], the tunneling current can be expressed as:

$$I(V) \propto \int_{E_F}^{E_F+eV} \rho_s(E)\rho_t(E-eV)T(z,E,eV)dE \tag{1.7}$$

where $T(z,E,eV)$ is a factor describing the tunneling transmission dependence on the tip-sample distance z, the energy and the applied bias voltage. By differentiating equation 1.7 with respect to the bias voltage we obtain:

$$\begin{aligned}\frac{dI}{dV} \propto\ & \rho_t(E_F)\rho_s(E_F+eV)T(z,E_F+eV,eV)+ \\ & +\rho_t(E_F-eV)\rho_s(E_F)T(z,E_F,eV)+ \\ & + \int_{E_F}^{E_F+eV} \rho_t(E-eV)\rho_s(E)\frac{dT(z,E,eV)}{dV}dE+ \\ & + \int_{E_F}^{E_F+eV} \rho_s(E)\frac{d\rho_t(E-eV)}{dV}T(z,E,eV)dE\end{aligned} \tag{1.8}$$

If we assume a constant ρ_t and a constant transmission coefficient in the considered energy window, equation 1.8 simplifies into:

$$\frac{dI}{dV} \propto \rho_t(E_F)\rho_s(E_F+eV)T(z,E_F+eV,eV) + \rho_t(E_F-eV)\rho_s(E_F)T(z,E_F,eV)$$

Since T typically peaks at the E_F of the tip, when $V>0$, and at E_F of the sample when $V<0$ [20], the conductance is dominated by the first term of equation 1.9 when $V>0$, and by the second term when $V<0$. Thus, the differential conductance of the

empty states is proportional to the DOS of the sample at a given energy determined by eV. On the other hand, the differential conductance of the filled states depends on the DOS of the tip at eV.

In STS, tips are typically modified by indentation until their density of states is rather flat all over the energy window of interest. The experimental acquisition of the dI/dV signal is normally done using a Lock-In amplifier. A small modulation is applied to the tunneling voltage V_T, by adding a sinusoidal voltage $V_{mod}sin(\omega t)$. Consequently the tunneling current is modulated, and can be expressed as a Taylor series:

$$I(V_T + V_{mod}sin(\omega t)) \sim I(V_T) + \frac{dI(V_T)}{dV}V_{mod}sin(\omega t) + \frac{1}{2}\frac{d^2I(V_T)}{dV^2}V_{mod}^2 sin^2(\omega t) + ... \quad (1.9)$$

By means of the Lock-In amplifier, the amplitude of the first harmonic frequency can be extracted, and thus a signal proportional to the differential conductance dI/dV is acquired. Spectra are typically acquired in open feedback conditions, by setting a set-point starting current and bias and keeping the tip at a fixed XYZ position. The dI/dV signal is then recorded while sweeping V_T over the energy window of interest. While this method provides clear spectra in the energy region of one or two volts around E_F, the tunneling transmission drastically increases at larger $|V_T|$ hindering the recognition of DOS features.

Another method to acquire a dI/dV spectrum is to keep the feedback on, thus maintaining a constant tunneling current while sweeping V_T. In this method the transmission is high at lower biases and decreases for increasing $|V_T|$, allowing for an easier recognition of DOS features at larger biases, while making it difficult close to E_F.

Finally, the dI/dV signal can be mapped over a region if scanning at relatively slow speeds. These dI/dV maps can be acquired in constant current or constant height modes and provide the spatial distribution of the LDOS at a given energy.

1.2 Intramolecular resolution with functionalized tips

Although STM is able to easilt image single atoms, resolving the atomic structure of a molecule is a much more difficult task. The convolution between the molecule structure and LDOS normally results on orbital shapes [16, 22]. This limitation was recently overcome by R. Temirov *et al.* [23] using STM and shortly after by L. Gross *et al.* using non contact Atomic Force Microscopy (nc-AFM) [19]. Both works used a similar approach to obtain an unprecedented chemical resolution: the use of a functionalized tip.

Intramolecular Imaging

In the case of nc-AFM, intramolecular resolution of pentacene was achieved by picking up a CO molecule with the STM/AFM tip. The tip was then brought to close proximity of pentacene in constant height mode. At small tip-molecule distances, the AFM qPlus sensor [24], recorded sharp changes in the frequency shift over the molecule, which resulted in the intramolecular resolution observed in Figure 1.2a. The contrast

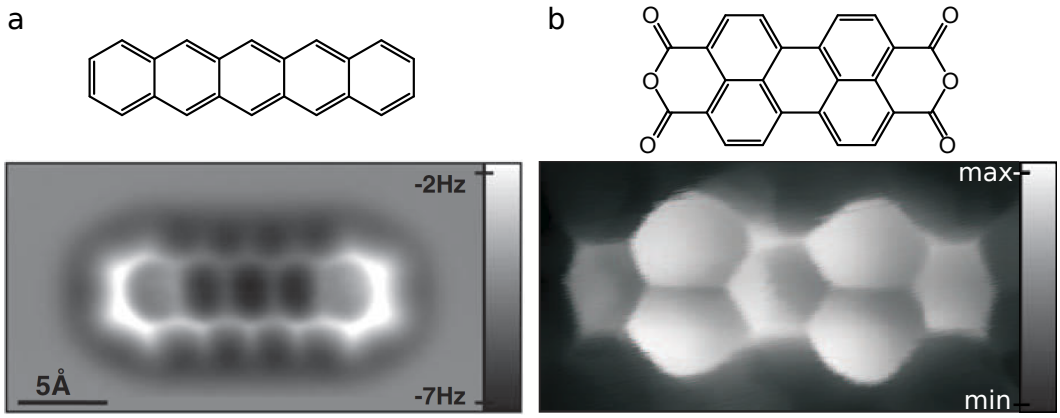

Figure 1.2: (a) Pentacene chemical structure and atomically resolved NC-AFM frequency shift image adapted from [19]. More negative frequency shifts (dark) imply less repulsive regions and frequency shifts closer to zero or positive values (bright) translate into more repulsive regions. (b) Chemical structre and atomically resolved STHM conductance image of PTCDA (3,4,9,10-perylenetetracarboxylic-dianhydride) adapted from [27]. The contrast is inverted compared to the NC-AFM in panel *a*. Carbon ring regions appear with higher conductance (bright), while atomic and bond positions appear with smaller conductance (darker).

actually arises from the repulsive forces originating from the Pauli repulsion between CO and the studied molecule [19]. This only occurs when short range forces, i.e. Pauli repulsion, have significant contributions over the long range forces, namely the electrostatic and van der Waals forces [19, 25]. The CO tip plays a key role in this process, as it allows reaching smaller tip-molecule distances, which would otherwise result in contact and molecule pick up in the case of a metal tip.

The intramolecular resolution observed by STM, first called Scanning Tunneling Hydrogen Microscopy (STHM) [23], was first achieved by trapping a H_2 or D_2 single molecule beneath the STM tip. Molecular hydrogen condensates on the sample surface at low temperatures and is trapped benath the tip at biases below a certain vibrational transition [26–29]. Using H_2 as probing tip and acquiring constant height dI/dV maps at low biases (-5 mV for Figure 1.2b), the atomic contrast arises from changes in the conductance over the sample molecule (Figure 1.2b). The origin of these changes in conductance is again the Pauli repulsion between the trapped hydrogen and the molecule [27]. However, in this case, the hydrogen acts as a transducer, converting the sensed repulsive forces to changes in the junction conductance. Following works generalized the observed contrast in STHM to other probe molecules, such as CO, Xe and CH_4 [30].

The transducing mechanism, which yields differences in conductance between atomic sites and ring sites, was first ascribed to the depletion of the tip DOS caused by the Pauli repulsion [27]. As the tip drags the hydrogen molecule over sample molecule, the hydrogen is squeezed against the tip, balancing both Pauli repulsion between molecule and H_2 and H_2 and tip. The overlap between H_2 and tip wavefunctions causes a depletion of the tip DOS due to the Pauli exclusion principle, yielding a lower conductance over the atomic sites, where the repulsion is stronger.

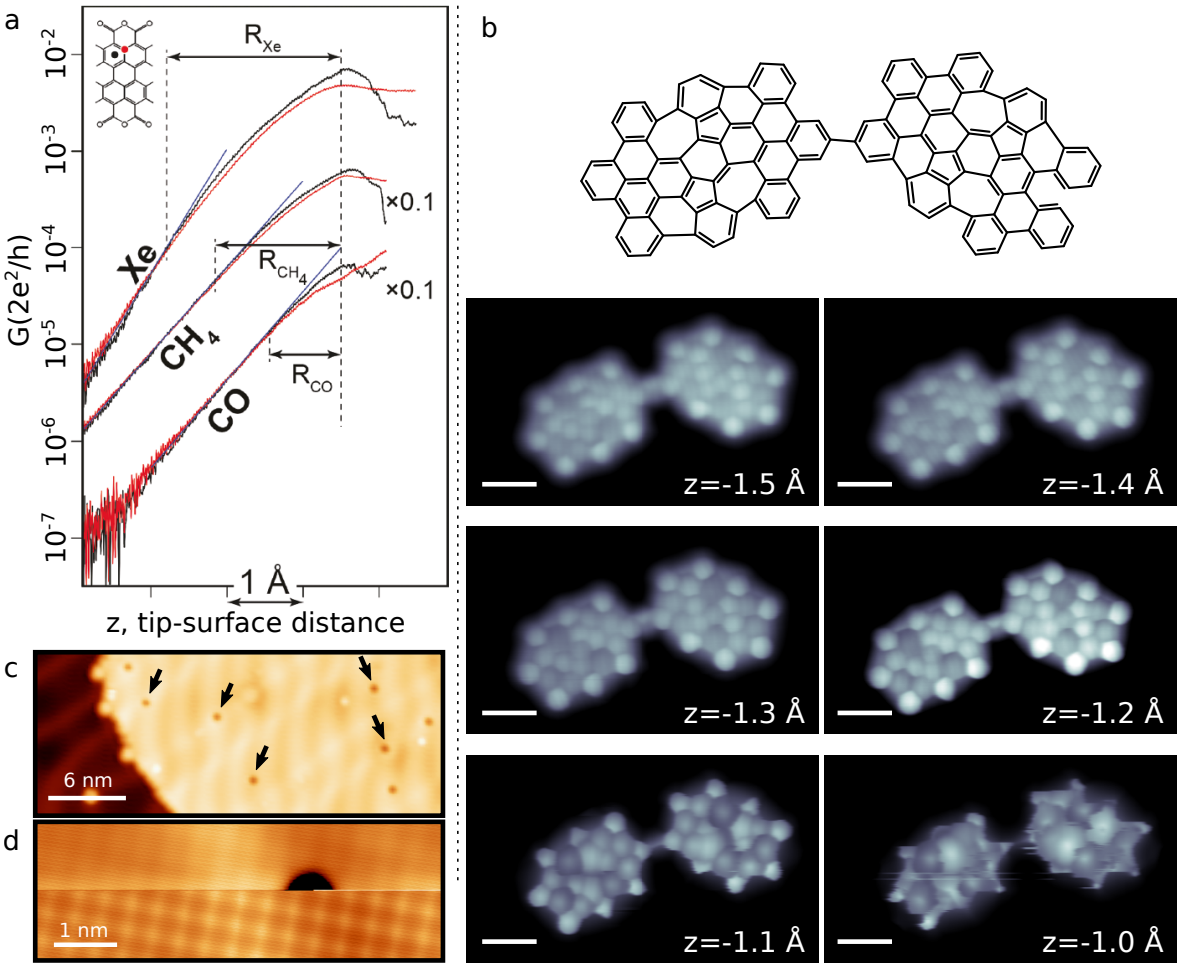

Figure 1.3: (a) Conductance approach curves at two different PTCDA sites (red carbon atom, black center carbon ring) for different probe molecules, adapted from [30]. The CO and CH_4 curves are multiplied by 0.1. R represents the range for imaging with intramolecular resolution. We note that R_{CO} is barely 1 Å in good agreement with our observations in panel *d*. (b) Top: Molecular structure of a dimer observed in Part III of this thesis. Bottom: Intramolecular resolved dI/dV maps with a CO tips of the dimer, at different tip-sample heights. At the farthest distance (z=-1.5 Å), the intramolecular features smear out, and the resolution starts to fade. The optimal imaging region is closer, between z=-1.3 Å and z=-1.2 Å. Beyond that the repulsion between molecule and CO is too strong, the image is distorted and the dimer moves. All scale bars correspond to 7 Å (V_s= 5 mV V_{rms}= 12 mV f=700 Hz; Open feedback parameters: I_t= 100 pA V_s= 5 mV). (c) CO recognition on top of a NaCl island deposited on top of Au(111). Black arrows point the dark spots associated with CO molecules (I_t= 52 pA V_s= 2 V). (d) Change in resolution upon CO pick up on top of a NaCl island (I_t= 110 pA V_s= 1 V).

However, recent works provided a simpler model for the transducing mechanism of the probe particle. Within the model of Hapala *et al.* [31,32], the probe molecule (CO or Xe) is mechanically in response to the forces acting over it, specially the Pauli repulsion. This model considers constant DOS of tip, probing molecule and sample during

the scanning process, in contrast to previous interpretations by Weiss *et al.* [27]. The relaxation typically results in lateral displacements of the probe molecule and the consequences of these rearrangements are twofold. On the one hand, the lateral relaxations translate to lower conductances on top of the atomic sites and bond positions, as the probing molecule is pushed aside from the repulsive potentials generated at those sites. Inside the carbon rings, the tip cannot laterally relax since it lays within the potential "basin" formed by the ring and thus, the conductance is larger. This is the origin of the transducing effect that provides intramolecular resolution in STM, the lateral relaxations of the probe particle. On the other hand, the sharpness of the features observed in atomically resolved STM and AFM images is also related to the lateral displacements of the tip. At the borders of the potential basins produced by the Pauli repulsion, the probe molecule relaxation changes strongly upon small variations of the tip positions respect to the molecule sample. This results in sharp features from blunt potential profiles.

The distance range in which CO-tips achieve intramolecular resolution is typically of $\sim$ 1 Å (Figure 1.3a), defined as the tip-surface distances producing optimal contrast of atomic and carbon ring sites [30]. Images at farther distances suffer loss of intramolecular resolution while closer images start to distort due to strong displacements of the CO and/or the sample molecule (Figure 1.3b). From Figure 1.3a, we can extract that R_{CO} corresponds to tunnel junction resistances between $\sim$150 MΩ and $\sim$15 MΩ. This fits nicely with the behavior observed in Figure 1.3b: the tunneling resistance of the image at z=-1.2 Å averages around $\sim$40 MΩ while the image at z=-1.0 Å averages around$\sim$20 MΩ.

Tip-functionalization procedure

The intramolecular resolved images acquired in this thesis were done by using CO tips in constant height dI/dV maps. In order to facilitate the CO recognition and pick up, we deposited NaCl islands on the sample precovered with the molecular especies to study. The CO appears as dark depressions on top of the islands, as seen in Figure 1.3c. Moreover, the CO is loosely bound to the NaCl which ensures an easy pick up by just scanning over the molecule. Figure 1.3d shows the CO pick up and the subsequent change in topographic resolution, allowing to easily resolve the NaCl atomic structure.

Imaging of molecular states

The high stability of CO tips allows dI/dV mapping of molecular states at energies far from E_F. The CO tip does not only allow imaging closer to the sample, but also increses the lateral resolution of the conductance maps [22]. The reason behind the higher resolution is the mixing of the metal tip states with the CO orbitals 1.4a. This provides the tip with a certain p-wave character, that modulates the tunneling current according to the relative symmetries of tip and sample. Figure 1.4b sketches this process as the overlap of one of CO π orbitals with the wavefunction of a ribbon band. The overlap causes the appearance of current maxima at the nodal planes of the wavefunction, and current minima on top of the wavefunction lobes [22].

In practice, the contrast observed in dI/dV maps acquired with CO-tips is the

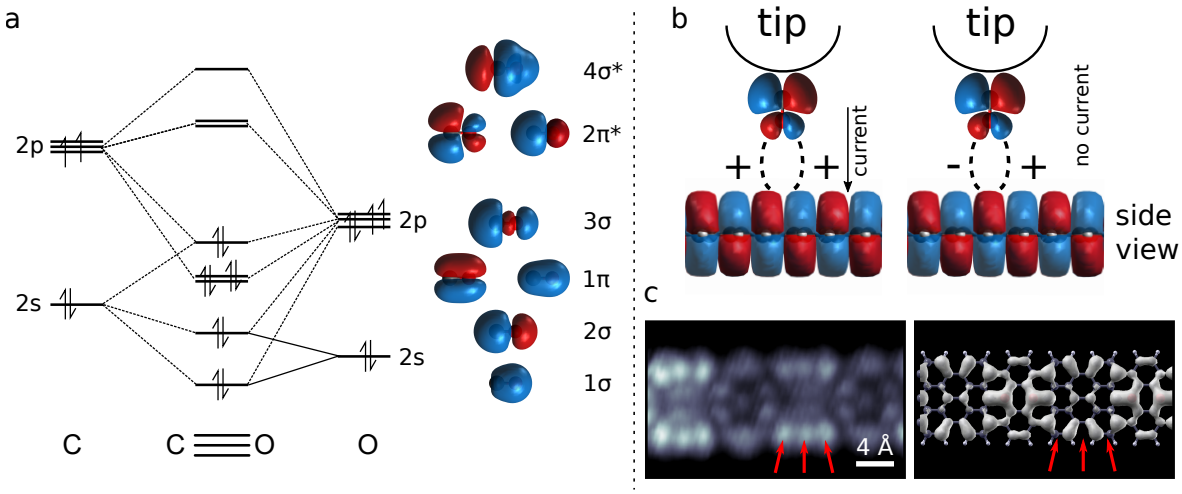

Figure 1.4: (a) Molecular orbital energy diagram for a CO molecule. 1π and $2\pi^*$ orbitals provide the p-wave character to the CO tip. (b) Symmetry mechanism governing the contrast in CO functionalized tips. Contributions to the tunneling current from $+$ and $-$ lobes of the π tip orbital add up on top of the sample nodal planes. On the contrary, these contributions cancel each other on top of a sample orbital lobe. (c) Left: Constant height dI/dV map of the valence band of a 2B-7-AGNR using a CO tip. Right: Calculated LDOS of the 2B-7-AGNR valence band. Red arrow highlight the three lobes in conductance, corresponding to the three minima in LDOS.

result of the convolution of all CO orbitals. This complicates the correspondence of the wavefunction/LDOS of a state with its conductance image without the support of STM image simulations. Figure 1.4c shows a constant height dI/dV map of the 2B-7-AGNR valence band acquired with a CO functionalized tip, and its calculated LDOS. The map roughly corresponds to maxima of conductance appearing at the positions of the LDOS minima. For instance, we can resolve three lobes radially distributed (red arrows), while the LDOS shows three equally spaced minima.

To conclude, we have reviewed the potential of using functionalized tips to resolve the atomic structure of molecules. In particular, CO tips provide the best resolution while being exceptionally stable [30]. The transducing effect governing the atomic resolution in STM is particularly powerful and simple and allows obtaining good resolutions in a feedback-less image. Due to the *p*-wave character provided by the CO, this functionalization is also useful in increasing the resolution of dI/dV maps.

1.3 The experimental setup

The experimental results presented in this thesis were acquired in a Low-Temperature STM designed by Prof. Gerard Meyer and Dr. Sven Zöphel and built by Christian Roth and Dr. Mico Alemany in 2003. The ultra high vacuum (UHV) system consists on two independent chambers (Figure 1.6). The preparation chamber is outfitted with standard UHV equipment tools: sputter gun, mass spectrometer, quartz balance and a commercial 4-fold Knudsen cell evaporator. The STM chamber hosts the STM head in contact with a LHe cryostat with an equilibrium temperature of 5K. The head is a Besocke "beetle" type [33] (Figure **??**), isolated from mechanical vibrations using stainless steel springs, eddy current damped. The whole setup is lifted by pneumatic feet to further damp low frequency vibrations. Moreover, the whole microscope lays on top of a 30 Tm reinforced concrete slab that can be also pneumatically lifted, effectively decoupling the microscope from the building vibrations. The measurements are carried using CREATEC DSP and HV Amplifier units. Spectroscopic measurements are acquired using an external Stanford Research SR830 lock-in amplifier. The STM data has been analyzed with WSxM software [34].

The substrate used on all experiments was Au(111) monocrystal. The sample is

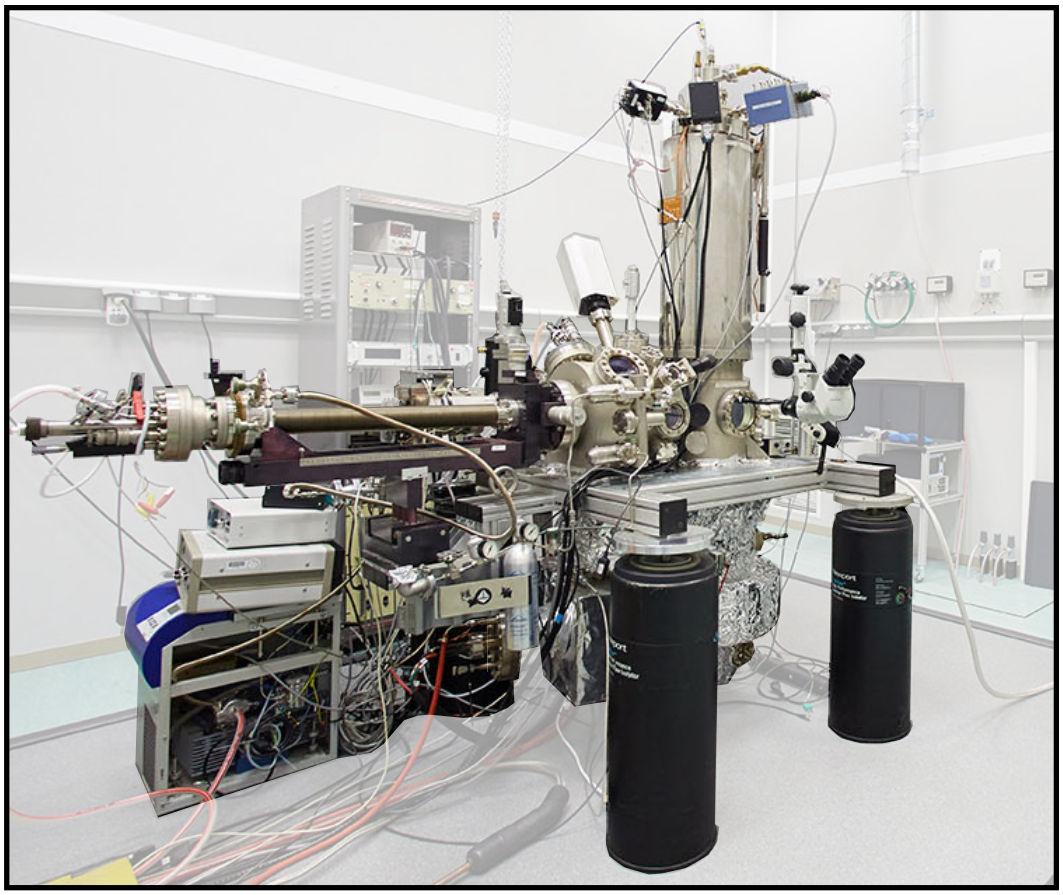

Figure 1.5: Photograph of the CREATEC UHV-LT-STM system (MILANO) used during this thesis.

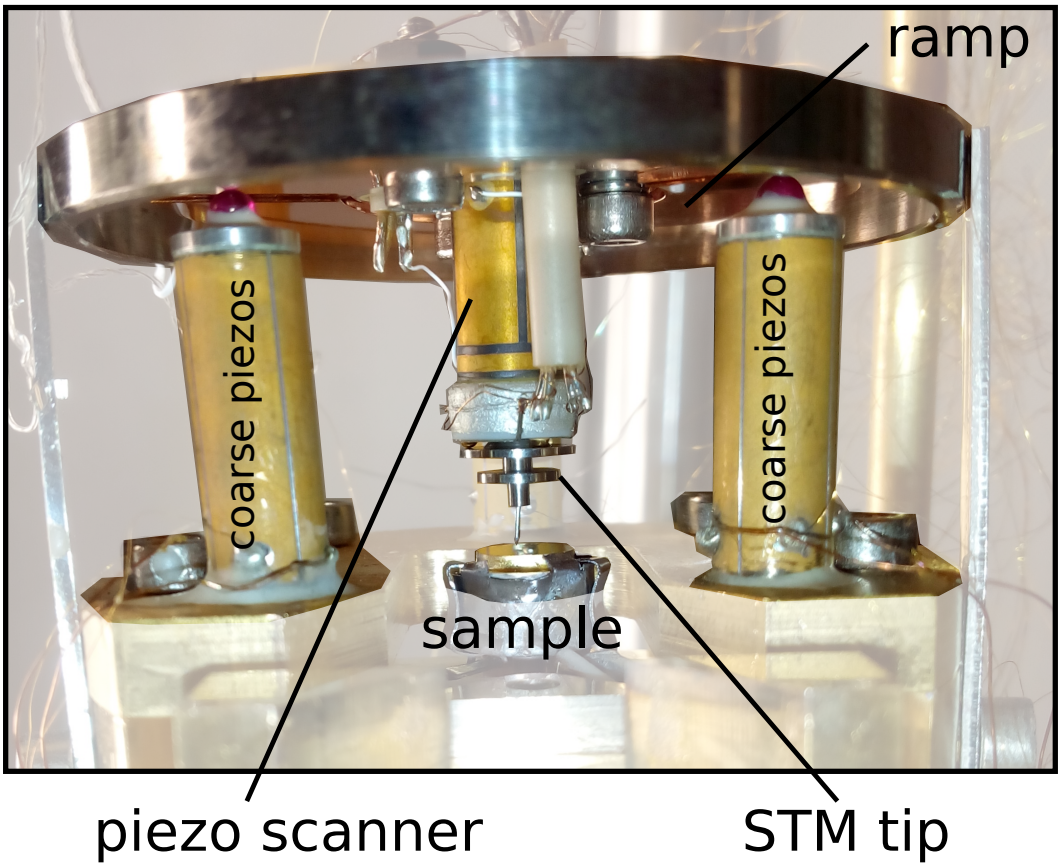

Figure 1.6: Photograph of the disassembled STM head.

sputtered with ionized Neon, accelerated to kinetic energies in the order of 1.5 keV. The surface is then reconstructed by anneling it to ∼730 K via direct current heating. The sample temperature is controlled by a thermocouple in contact with the sample. The sputter-annealing cycles are repeated until the sample is atomically clean and flat, displaying its characteristic herringbone reconstruction [35]. The heating mechanism of our UHV equipment allows a precise temperature control during molecular depositions and annealing steps, which is particularly useful in on-surface reaction studies.

Part I

Introduction to Graphene Nanoribbons

The electronic properties of Graphene Nanoribbons mostly derive from their graphene matrix. Thus GNRs can be described by just applying different boundary conditions to an infinite 2D graphene sheet. In the tight binding approach, this is suffices to characterize the edge states in zigzag nanoribbons and the bandgap of most of armchair graphene nanoribbons [2]. A more visual framework to understand the properties of GNRs is analizing the aromaticiy of representative GNR structures under Clar's formalism [36–38].

Preserving these electronic properties requires an almost flawless ribbon lattice and edge structure. The on-surface synthesis approach particularly shines in achieving this requirements. By using smaller molecular precursors as building blocks, and by taking advantage of the catalytic properties of a metal substrate, several GNRs have been successfully synthesized [5, 39–44].

The first ribbon synthesized by this process was the 7-AGNR by J. Cai and coworkers [5], which allowed a precise experimental study of its electronic properties [45, 46] and served as reference framework for the study of other ribbons, both doped and undoped.

In the following chapters we are going to review the electronic structure of AGNRs and ZGNRs as a topologic transformation of the graphene band structure. The properties of GNRs will also be described from a more qualitative perspective using Clar's formalism. Additionally, the atomically precise growth of these ribbons via on-surface synthesis will also be presented. To conclude this part, we will focus on the growth and electronic properties of 7-AGNR using STM.

Chapter 2

Electronic Properties of Pristine Graphene Nanoribbons

Graphene is a two-dimensional crystal made of a single layer of carbon atoms arranged in a honeycomb lattice. Its structure can be described by the primitive vectors $\boldsymbol{a_1}$ and $\boldsymbol{a_2}$, with $a_{cc} \simeq 1.42\,\text{Å}$ as the carbon-carbon distance:

$$\boldsymbol{a_1} = \frac{a_{cc}}{2}(3, \sqrt{3}) \qquad \boldsymbol{a_2} = \frac{a_{cc}}{2}(3, -\sqrt{3}) \tag{2.1}$$

and a two-atomic base, where the vectors $\boldsymbol{\delta_{1-3}}$ define the the positions of the first neighboring atoms (Figure 2.1a). Alternatively, we can describe the carbon sheet as two triangular sublattices A and B. The Brillouin Zone of graphene is a hexagon rotated 30 degrees (Figure 2.1b), with primitive reciprocal vectors $\boldsymbol{b_1}$ and $\boldsymbol{b_2}$:

$$\boldsymbol{b_1} = \frac{2\pi}{3a_{cc}}(1, \sqrt{3}) \qquad \boldsymbol{b_2} = \frac{2\pi}{3a_{cc}}(1, -\sqrt{3}) \tag{2.2}$$

The carbon atoms are sp^2 hybridized, with the remaining valence electron in the p_z orbital coupling with its neighbors in extended conjugated states and leading to the creation of π-bands. Close to the Γ point, the bands can be described as quadratic functions of k_x and k_y while at the M points, the bands possess a saddle point. However, the most characteristic feature of graphene is its band structure close to the $\text{K}_\pm$. At these positions the π-bands can be approximated to [47]:

$$E(\boldsymbol{K}_\pm + \boldsymbol{k}) \simeq \hbar v_F |\boldsymbol{k}| + \mathcal{O}[(k/K)^2] \quad \text{and} \quad v_F = 3ta_{cc}/2 \tag{2.3}$$

where t is the nearest-neighbor hopping energy (usually $t \approx 2.7$ eV) and v_F is the Fermi velocity, which amounts to $v_F \approx 10^6$ m/s [47, 48]. An important consequence from Equation 2.3 is that the band dispersion is linear, i.e. the Fermi velocity in graphene is independent of the carrier mass or momentum, and, as a result, we can consider graphene electrons as massless Dirac fermions. As seen in Figure (2.1c) near $\text{K}_\pm$, the bands can be visualized as electron-hole symmetric cones, the so-called Dirac cones. Since the π-bands are half-filled, they join exactly at E_F, and as a result graphene is considered a semimetal.

The electronic structure of GNRs can be understood as the projection and discretization of the graphene 2D band structure onto the crystallographic direction of

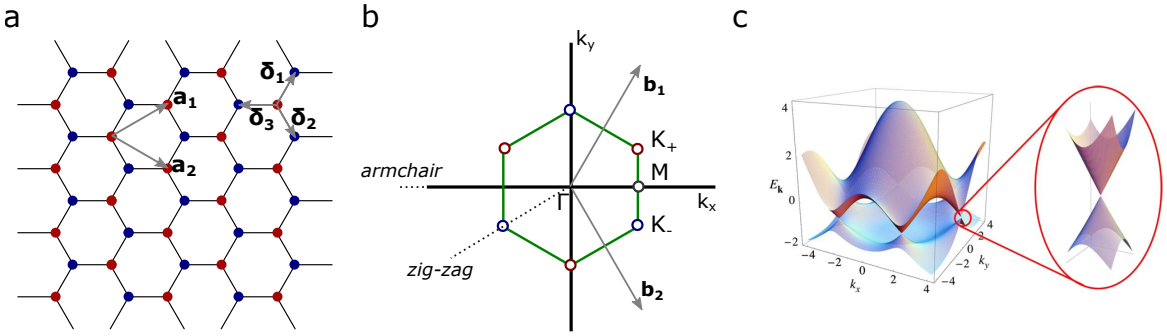

Figure 2.1: (a) Graphene lattice and its primitive vectors $\boldsymbol{a_1}$ and $\boldsymbol{a_2}$. The vectors $\boldsymbol{\delta_1} = \frac{a_{cc}}{2}(1, \sqrt{3})$, $\boldsymbol{\delta_2} = \frac{a_{cc}}{2}(1, -\sqrt{3})$ and $\boldsymbol{\delta_3} = a_{cc}(-1, 0)$ define the nearest-neighbors and define the translations between the two triangular sublattices defined by red and blue atoms.(b) Reciprocal space of Graphene and its reciprocal primitive vectors $\boldsymbol{b_1}$ and $\boldsymbol{b_2}$. The Dirac points are located at $K_{\pm} = \left(\frac{2\pi}{3a_{cc}}, \pm\frac{2\pi}{3a_{cc}\sqrt{3}}\right)$ and the M point is located at $M = \left(\frac{2\pi}{3a_{cc}}, 0\right)$. Dashed lines indicate the growth directions of armchair and zigzag GNRs in the reciprocal space. (c) Band structure of graphene from [47]. The close up shows the linear behavior of the bands close to the Dirac points. The slope of these cones correspond to the Fermi velocity v_F.

the nanoribbon growth direction. In the graphene sheet, the growth direction of Armchair Graphene Nanoribbons (AGNRs) is defined by the translational vectors $\boldsymbol{\delta_{1-3}}$, while the Zigzag Graphene Nanoribbons (ZGNRs) growth directions is that of the primitive vectors $\boldsymbol{a_1}$ and $\boldsymbol{a_2}$. Therefore, AGNRs follow the ΓM direction and ZGNRs the ΓK direction.

2.1 Armchair Graphene Nanoribbons

For AGNRs, the discretization of the band structure can be solved from the boundary conditions imposed by the edges of the ribbon. As seen in Figure 2.2a, a N-AGNR is composed by N carbon dimer lines, each of these carbon atoms belonging to two different sublattices A and B. At $N = 0$ and $N = N+1$, the carbon atoms are missing and are replaced by Hydrogen atoms. For simplicity we are going to set the unit cell size of the ribbon $a = 1$, unless the contrary is specified. Considering the ribbon infinite along its growth axis, we can suppose a general form for the electronic wavefunctions of the two sublattices:

$$\begin{aligned} \psi_{m,A} &= Ae^{ik_\perp m} + Be^{-ik_\perp m} \\ \psi_{m,B} &= Ce^{ik_\perp m} + De^{-ik_\perp m} \end{aligned} \tag{2.4}$$

where *m,A(B)* stands for the mth position in the GNR A (B) sublattice, $k_\perp$ is the wavenumber in the direction perpedincular to the ribbon growth axis, and A, B, C, D are arbitrary coefficients. Since for $N = 0$ and $N = N+1$ the carbon rows are missing in both sublattices A and B, we have the following boundary conditions:

$$\psi_{0,A} = \psi_{0,B} = \psi_{N+1,A} = \psi_{N+1,B} = 0 \tag{2.5}$$

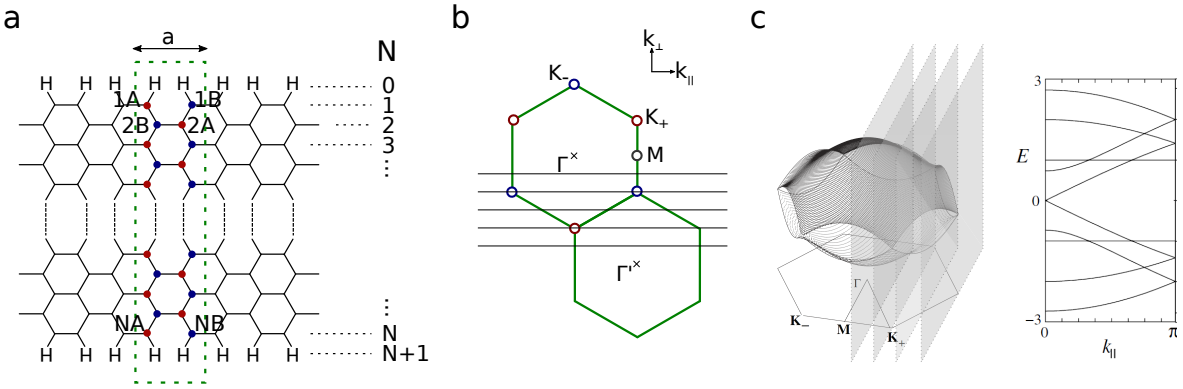

Figure 2.2: (a) Lattice structure of a generic N-AGNR, where N accounts for the number of carbon dimer lines. Hydrogen atoms substitute the carbon atoms at $N = 0$ and $N = N + 1$. The unit cell of the AGNR has a lenght $a = 3a_{cc}$ and is highlighted in green. (b) Reciprocal lattice of graphene showing the discrete values of $k_\perp$ for $N = 5$ ($N = 3p + 2$). The cuts cross over the Dirac points and thus, the ribbon is gapless. (c) Three dimensional representation of the graphene band structure (right, from [2]) and the discrete $k_\perp$ plane cuts for a 5-AGNR. The projection of the band structure onto the planes[1] gives rise to the 1D bands for the 5-AGNR (left, from [2]).

That lead to (likewise for sublattice B):

$$\psi_{0,A} = A + B = 0 \Rightarrow A = -B$$
$$\psi_{N+1,A} = Ae^{ik_\perp(N+1)} + Be^{-ik_\perp(N+1)} = 0 \quad \text{if} \quad \eta = e^{ik_\perp(N+1)} \Rightarrow A\eta = -B\eta^{-1} \tag{2.6}$$

From these two relations we extract that:

$$\eta^2 = 1 = e^{2ik_\perp(N+1)} \tag{2.7}$$

Which finally leads to the discrete $k_\perp$ condition:

$$k_\perp = \frac{r}{N+1}\pi \quad \text{for} \quad r = 1, 2, ..., N. \tag{2.8}$$

Or if we rescale it to the AGNR unit cell longitudinal size a:

$$k_\perp = \frac{2\pi}{a/\sqrt{3}}\frac{r}{N+1} \quad \text{for} \quad r = 1, 2, ..., N. \tag{2.9}$$

This discretization relation defines the possible electron momenta across the ribbon. It can be easily visualized as equidistant plane cuts in the reciprocal space of graphene (Figure 2.2b). The AGNR bands are the result of the intersection of the graphene bands with the planes defined by the discrete values of $k_\perp$. From this approach, we can also see that, whenever $N = 3p + 2$ (where p is a positive integer), the AGNR will be gapless, since the plane cuts pass through the Dirac points of graphene.

[1] The strictically correct representation is the projection of the band structure of graphene with invariance along the armchair axis (or zigzag for ZGNRs), as displayed in Figure 6 from Wakabayashi et al. [2]

This can also be demonstrated from the analytic solution of the eigenenergies of the AGNR bands obtained by solving the first neighbor tight-binding Hamiltonian [2]:

$$E_s = s\sqrt{1 + 2\epsilon_p \cos\left(\frac{k_\parallel}{2}\right) + \epsilon_p^2} \tag{2.10}$$

where $s = \pm 1$ and $s = 1$ and $s = -1$ correspond to the conductance and valence band respectively, and $\epsilon_p = 2\cos k_\perp$. Whenever $N = 3p + 2$ then $E_s = 0$ at $k_\parallel = 0$ and the AGNR is semimetallic. From Figure 2.2b and c we can also infer that the bandgap of the AGNR will be determined by the plane cut closest to the K_+ points. Furthermore, this bandgap will decrease for increasing width of the ribbon, as seen in Equation 2.9. In the tight-binding approximation, the bandgaps E_g^{TB} can be defined as [49]:

$$E_{g,3p}^{TB} = t\left[4\cos\frac{p\pi}{3p+1} - 2\right], \quad E_{g,3p+1}^{TB} = t\left[2 - 4\cos\frac{(p+1)\pi}{3p+2}\right], \quad E_{g,3p+2}^{TB} = 0 \tag{2.11}$$

As seen in Figure 2.3a, the $N = 3p$ and $N = 3p + 1$ nanoribbons follow a similar trend, while the $N = 3p + 2$ family is gapless, as defined in Equation 2.10. However, the tight binding approximation considers all carbon atoms in the ribbon to have equal properties, which is potentially inaccurate the closer these atoms are to the edge. For the AGNR, the bond lengths along the growth direction are shortened by $\sim 3.5\%$, which causes a 12% increase in the hopping term t [49]. It is possible to perturbatively solve the Hamiltonian of this system by considering that the hopping energy in the direction parallel to the dimer lines is $t_1^\parallel = t_N^\parallel \equiv t(1 + \delta)$ at the lattice positions $N = 1$and N. The first order approximation, which agrees nicely with first principle LDA calculations, gives the following bandgap expressions [49]:

$$\begin{aligned} E_{g,3p} &= E_{g,3p}^{TB} - \frac{8\delta t}{3p+1}\sin^2\frac{p\pi}{3p+1}, \\ E_{g,3p+1} &= E_{g,3p+1}^{TB} + \frac{8\delta t}{3p+2}\sin^2\frac{(p+1)\pi}{3p+2}, \\ E_{g,3p+2} &= E_{g,3p+2}^{TB} + \frac{2\delta t}{p+1} \end{aligned} \tag{2.12}$$

and result, for $\delta = 0.12$ (Figure 2.3b), in a clear splitting of the $3p$ and $3p+1$ bandgap trends, and the opening of a bandgap for the $3p + 2$ family. Therefore AGNRs are typically classified in three different families depending on their N-width, and their bandgaps follow $E_{g,3p+1} > E_{g,3p} > E_{g,3p+2}$. It's important to note that LDA simplifies the exchange-correlation potential, which plays an important role in nanostructures due to the stronger electron-electron interactions. As a result, AGNR bandgaps obtained by LDA are significantly smaller than the experimentally observed. More precise calculations, based on many-body perturbation theory, such as Green's Wavefunctions (GW), yield more accurate results [50] at expenses of higher computational cost. As a final remark, when comparing first principle calculations of free-standing nanoribbons with experimental results, the reduction of the bandgap due to the screening provided by the surface has to be taken into account as well [45, 51].

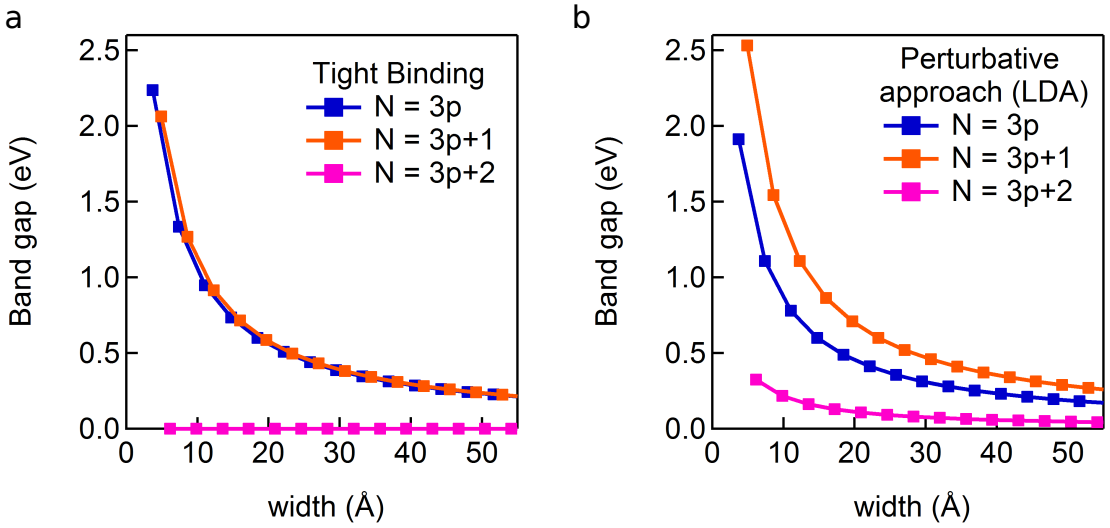

Figure 2.3: (a) Energy bandgaps for different N-AGNR within the tight binding model, with $t = 2.7$ eV. Two trends are observed, the gapless $3p+2$ family, and the families $3p$ and $3p+1$ with bandgaps inversely proportional with the ribbon width. (b) Same as in panel *a*, but considering the difference in hopping energies δ at the edges of the ribbon as a perturbation ($\delta = 0.12$ eV) [49]. The $3p$ and $3p+1$ families split in two different trends and a small bangap opens in the case of the $3p+2$ family. The results agree nicely with LDA first principle calculations [49].

2.2 Zigzag Graphene Nanoribbons

The electronic structure of ZGNRs is not as simple as the one of AGNRs. As seen in Figure 2.4a, the hydrogen atoms placed at lattice positions $N = 0$ and $N = N+1$, belong to different sublattices. Again for simplicity, we set the unit cell of the ribbon $a = 1$. The boundary condition for the generic wavefunctions:

$$\psi_{m,A} = Ae^{ik_\perp m} + Be^{-ik_\perp m} \quad , \quad \psi_{m,B} = Ce^{ik_\perp m} + De^{-ik_\perp m} \tag{2.13}$$

is $\psi_{0,B} = \psi_{N+1,A} = 0$. And thus:

$$\psi_{0,B} = C + D = 0 \Rightarrow C = -D$$
$$\psi_{N+1,A} = Ae^{ik_\perp(N+1)} + Be^{-ik_\perp(N+1)} = 0 \quad \text{if} \quad \eta = e^{ik_\perp(N+1)} \Rightarrow A\eta = -B\eta^{-1} \tag{2.14}$$

In contrast with AGNR, we cannot extract the discrete values of $k_\perp$ from the boundary conditions, but it can be shown [2] that the condition for $k_\perp$ is:

$$\sin[k_\perp N] + g_k sin[k_\perp(N+1)] = 0 \quad \text{with} \quad g_k = 2\cos(k_\parallel/2) \tag{2.15}$$

which implies that $k_\perp$ is both a function of the nanoribbon width and also the wavenumber along the ZGNR growth axis $k_\parallel$. Consequently, the $k_\perp$ cuts in the Brillouin Zone of graphene are not straight lines (Figure 2.4b). The bands defined by these cuts are shown in Figure 2.4c. They are degenerated at $k_\parallel = \pi$ as expected from the two-dimensional projection of the graphene band structure (Figure 2.5a, right).

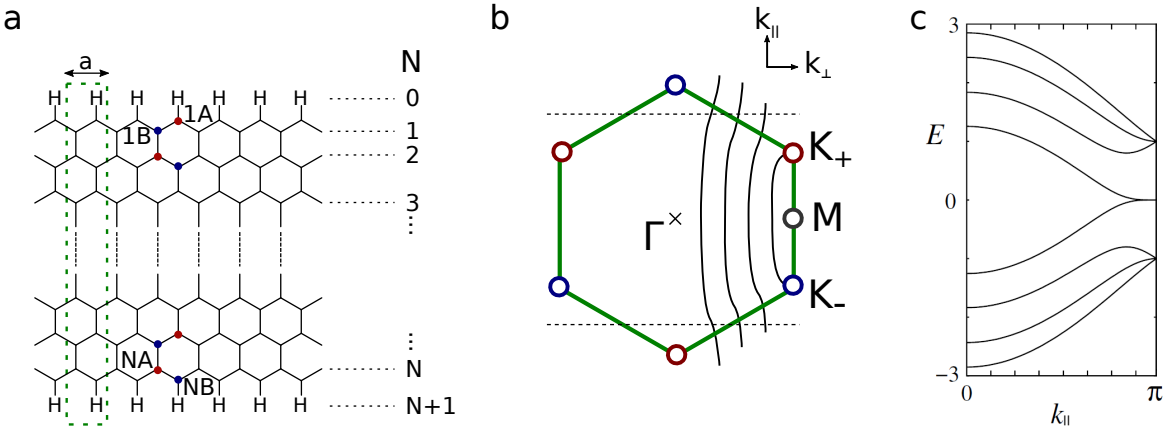

Figure 2.4: (a) Lattice structure of a N-ZGNR, where N stands for the number of zigzag lines. At $N = 0$ and $N = N + 1$, the carbon atoms are substituted by Hydrogen atoms. It is worth noting, that edge carbon atoms at $N = 1$ and N belong to different sublattices. The longitudinal cell size is $a = \sqrt{3}a_{cc}$. (b) Reciprocal lattice of graphene showing the discrete values of $k_\perp$ for $N = 4$ and the reciprocal unit cell of a ZGNRs in dashed lines. The cuts, solutions from Equation 2.15, are not linear, in contrast with AGNR. Also note the change in orientation of $k_\perp$ and $k_\parallel$ respect to Figure 2.2b. (c) Band structure of a 4-ZGNR (from [2]). The bands show degeneracy at $k_\parallel = \pi$, but also in the vicinity of $k_\parallel = \pi$ in the case of the CB and the VB.

However, the CB and VB bands show also degeneration after a certain critical $k_\parallel$ (Figure 2.4c and Figure 2.5a), which is not a feature of the two dimensional projection of the graphene band structure (Figure 2.5a). This critical k_c is given by [2]:

$$k_c = \pm 2 \arccos\left(\frac{1}{2 + 2/N}\right) \tag{2.16}$$

k_c marks the momenta in which the CB and VB join and it has two possible values between $0 < k_\parallel < 4\pi/3$ (or $0 < k_\parallel < \pi$ due to band folding). As seen in Figure 2.5b, these two values, k_{Lc} and k_{Rc}, define two regions where the CB and VB evolve into localized states: $k_{Lc} < k_\parallel < \pi$ and $k_{Rc} > k_\parallel > \pi$. This occurs because in these regions of the reciprocal space, there are only N-1 cuts instead of N (see Figure 2.5c for N=4). Two states arise as the CB and VB can no longer be defined as $k_\perp$ solutions of equation 2.15. These states are strongly localized at the edges of the ribbon [2, 52–54] for $k_c < k_\parallel < \pi$. Moreover, the wavefunctions of these so called edge states have only amplitude in one of the two sublattices of the ZGNR each [2, 52, 53].

These edges states origin from two imaginary $k_\perp$ solutions for equation 2.15 in the Brillouin Zone of graphene at $k_\perp = 0$ and $k_\perp = \pi$ (Figure 2.5c). They are solutions of Equation 2.15 in the following regions:

$$k_\perp = \begin{cases} \pi \pm i\zeta, & k_{Lc} < |k_\parallel| < \pi \\ 0 \pm i\zeta, & \pi < |k_\parallel| < k_{Rc} \end{cases} \tag{2.17}$$

and lead to wavefunctions for the edge states that decay toward the inner sites of the ZGNR [2, 53].

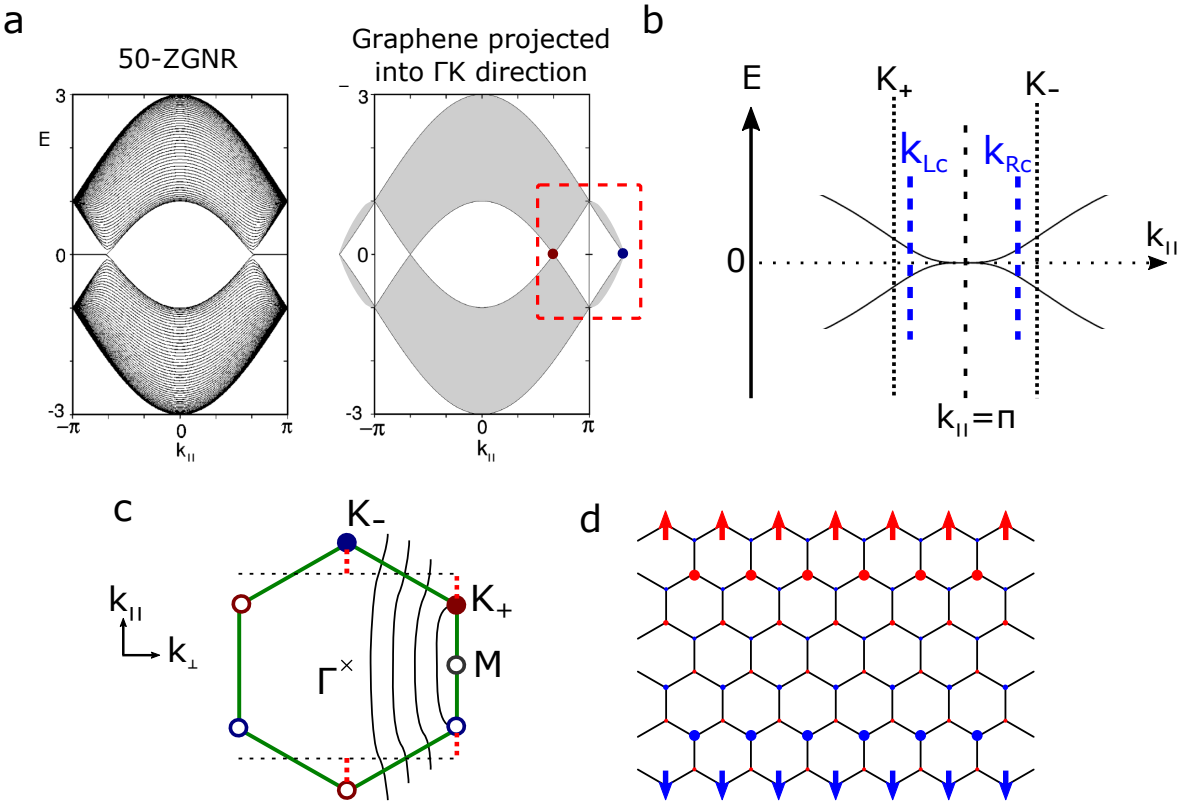

Figure 2.5: (a) Band structure of a 50-ZGNR (left) and the 2D projection of the graphene band structure into the ΓK direction (right) up to $k_{\parallel} = \pm 4\pi/3$ (adapted from [54]). The comparison between both band dispersions clearly shows that the ZGNR flat bands do not origin from the intrinsic band structure of graphene. (b) Energy diagram for a 4-ZGNR in the vicinity of the reciprocal space zone highlighted by dashed red in panel *a*. Dashed lines display the critical $k_{L,Rc}$ between which the extended bands become localized edge states. For large N, the critical k_c tends to the Dirac $K_{\pm}$, as seen in the band structure of 50-ZGNR in panel *a*. (c) Reciprocal lattice of graphene showing the discrete values of $k_{\perp}$ for $N = 4$ and and the reciprocal unit cell of a ZGNRs in dashed lines. Dashed red lines show the regions where $k_{\perp} = 0 + i\zeta$ and $k_{\perp} = \pi + i\zeta$ are solutions of equation 2.15, giving rise to the localized edge states in ZGNRs. $K_{\pm}$ Dirac points with filled circles are the ones displayed in the red highlighted area in panel *a*. (d) Sketch showing the magnetic structure of a 6-ZGNR edge state.

The presence of these edge states creates a strong DOS peak at the Fermi level, which is the responsible of the magnetic polarization of the edge states. This can be understood taking into account the edge state nature, with amplitude only in one of the sublattices, and the relatively small electron-phonon coupling in ZGNRs [55]. Due to the sharp DOS caused by the edge states, very small electron-electron repulsions give rise to magnetic moments specially strong at $N = 1$ and quickly decaying towards the center of the ribbon [2, 52].

Moreover, the magnetic moments in ZGNR arrange in an antiferromagnetic phase. Since each ribbon edge belongs to a different sublattices, the magnetic moments associated with the edge state accumulate in a particular sublattice. Because the total

magnetization of the ZGNR is zero, the other edge, and hence the other sublattice, shows the opposite spin orientation (Figure 2.5d). As a result the edge states are considered spin-polarized and the magnetic interaction opens a small bandgap between the edge states. [2, 49].

2.3 Graphene Nanoribbons under Clar's Theory

GNRs can be considered as large polycyclic aromatic hydrocarbons (PAHs), and thus, their different electronic properties can also be discussed using Clar's theory of the aromatic sextet [56]. According to this widely accepted theory, the most important Kekulé resonant structure of a PAH is that with the highest amount of aromatic disjoint π-sextets (Clar formula). These π-sextets are defined as six π-electrons localized in a single benzene-like ring separated from adjacent rings by C-C single bonds. The Clar formula is the most stable bond configuration [57] and characterizes best the local density of π states [58] and the bond length alternations [59].

The electronic configuration of graphene can be described using three equivalent Clar formulas, where one every three carbon hexagon is a π-sextet (or Clar sextet). This creates a Clar sextet ($\sqrt{3} \times \sqrt{3}$) superstructure as seen in Figure 2.6. Systems such as graphene, where all π electrons belong to a Clar sextet and have no localized double bonds, are called all-benzenoid PAHs and they show high stabilities. Although GNRs are normally non all-benzenoid PAHs, i.e. they show some localized double bonds, we can classify them into pseudo-all-benzenoid ribbons or non-benzenoid ribbons [37]. Pseudo-all-benzenoid ribbons are those that posses none or a constant amount of localized double bonds independent on their width while non-benzenoid ribbons are those whose number of localized double bonds increases with increasing width. We can further classify pseudo-all-benzenoid ribbons depending on the number of different equivalent Clar formulas they have, namely one unique Clar formula, two Clar formulas and more than two Clar formulas. Note that following this classification graphene is a (pseudo)-all-benzenoid system with more than two Clar formulas.

Figure 2.7 shows the previous classification applied to AGNRs. The three different families described in section 2.1 are in this case classified in terms of the number of equivalent Clar fomulas. The ribbons in $3p$ family have only one Clar formula, and in fact they are all-benzenoids, with no localized double bonds. The ribbons in $3p + 1$ family are pseudo-all-benzenoids and have exactly two Clar formulas and they are

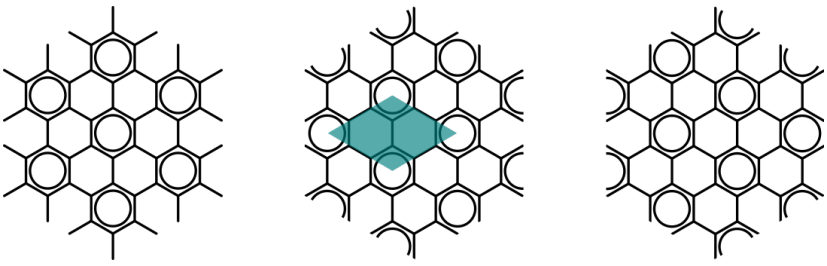

Figure 2.6: The three equivalent Clar formulas of graphene. The ($\sqrt{3}\times\sqrt{3}$) superstructure is highlighted in cyan.

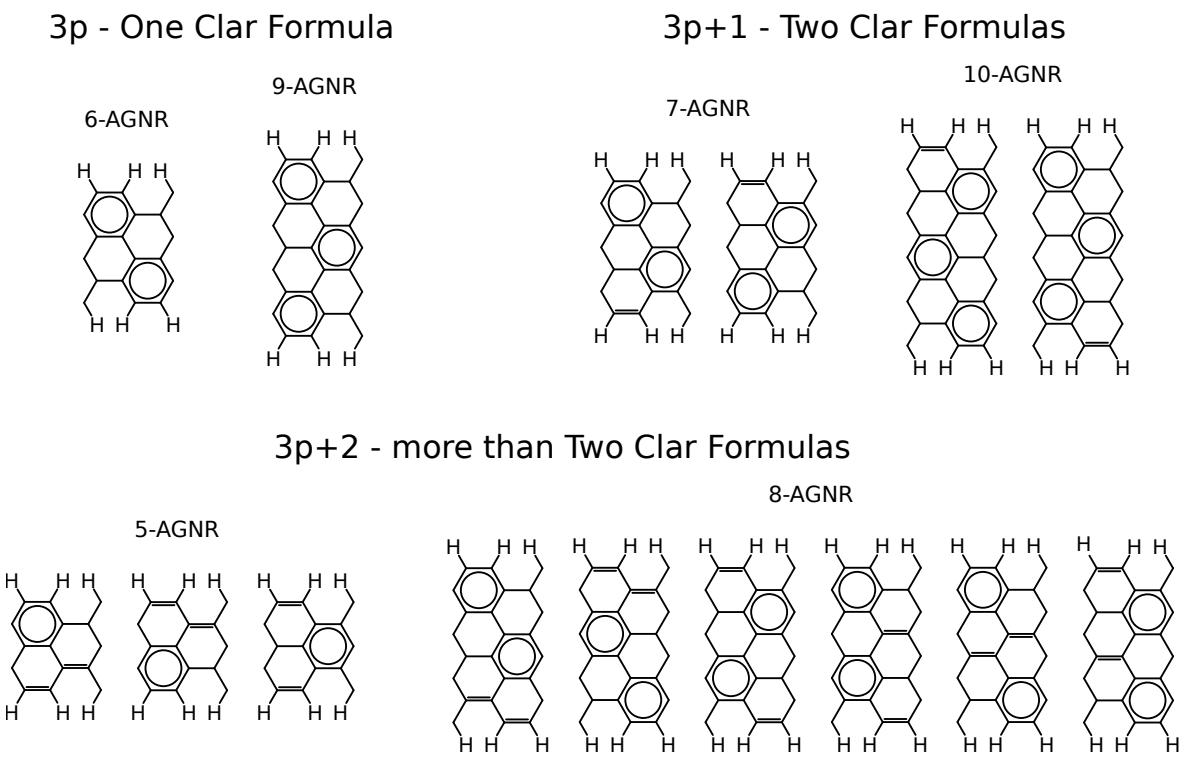

Figure 2.7: AGNR classification in terms of number of Clar Formulas. $3p$ ribbons possess only one formula, shown for the unit cell of 6 and 9-AGNRs. $3p+1$ ribbons possess two compatible Clar formulas. In each of these formulas there is a localized double bond at the edge of the ribbon, as seen in the formulas of 7 and 10 AGNRs. $3p+2$ ribbons have more than two Clar formulas, namely $3p$. As a result, their Clar sextets are mainly delocalized around all carbon hexagons.

pseudo-all-benzenoids with one localized double bond for any given p. Finally, the ribbons in $3p+2$ family are also pseudo-all-benzenoid, with two localized double bonds and $3p$ equivalent Clar formulas.

It is worth noting the relation between the different bandgap trends obtained by LDA in Figure 2.3a and the different Clar classes in Figure 2.7. Ribbons of the $3p+2$ family show a delocalization of Clar sextets all over the ribbon, similar as in the case of graphene (which falls in the same category as $3p+2$ ribbons). Hence, we can qualitatively understand the smaller bandgap trend for these ribbons. On the other hand $3p$ and $3p+1$ families show larger bandgaps due to the localization of their Clar sextets in either one or two Clar formulas. The larger bandgaps in the $3p+1$ family can be understood by the presence of a localized double bond at the edges of the ribbon in each Clar formula. This decreases the overall conjugation of the ribbon and increases slightly the bandgap.

We can use the same framework to describe ZGNRs and more precisely, the origin of their localized edge states. ZGNRs can host only a limited amount of Clar sextets, even for infinitely long ribbons. The formation of Clar sextets breaks the longitudinal symmetry of the ribbon, and splits the structure into two quinoidal conformations, i.e. two double bonds per carbon hexagon (Figure 2.8a). As a result we can consider ZGNR as non-benzenoid. However, if we allow the introduction of unpaired electrons

(radicals) into the structure, we can obtain pseudo-benzenoid structures (Figure 2.8b). Thus, for wide enough ribbons this is the preferred conformation as it reduces the overall ribbon energy. We can now visualize the origin of the edge states in ZGNR, since the radicals will give rise to localized edge states at the Fermi level. As they are unpaired spins, the spin polarized nature of the edge state can also be explained with Clar's formalism.

a

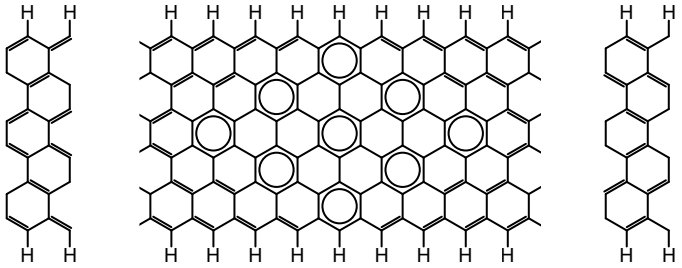

b

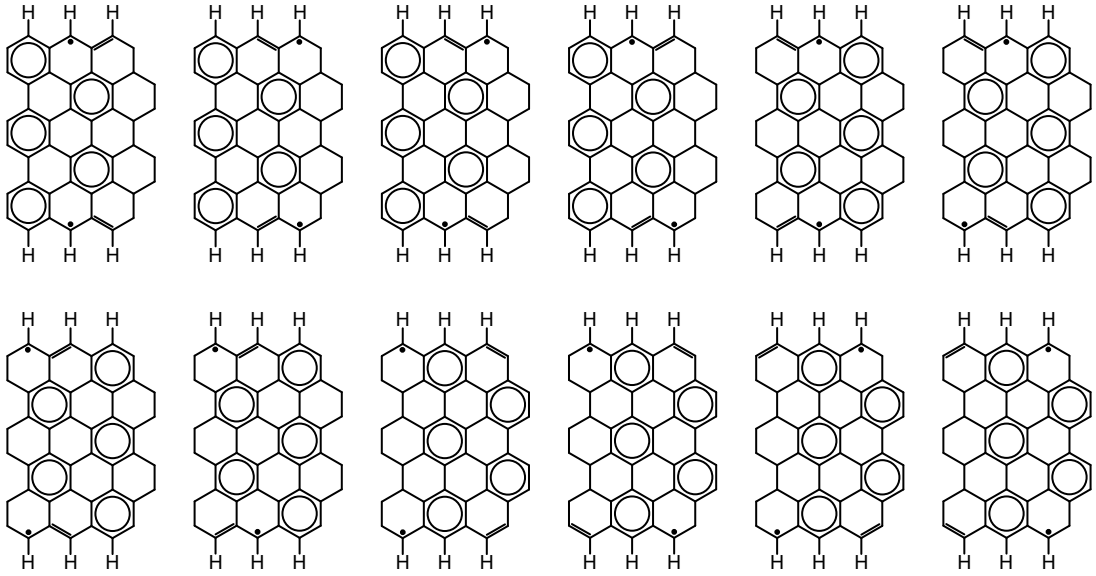

Figure 2.8: (a) Clar representation for a 8-ZGNR of infinite length. Only 9 Clar sextets can be placed all along the ribbon. The rest of the ribbon can be described by the two quinoidal structures at each side of the ribbon. Since these structures add up double bonds with increasing width, this Clar representation is non-benzenoid. (b) Clar formulas for a 8-ZGNR allowing the formation of a radical at each edge of the ribbon. This allows a pseudo-benzenoid representation of the ribbon. This structure is preferred if enough sextets are created and the resonance energy gained overcomes the energy cost of the radicals [37].

2.4 Growth of Graphene Nanoribbons

The previous sections have shown the strong dependence between the structure and the electronic properties of AGNRs and ZGNRs. The experimental realization of GNRs faces two main challenges. As seen in section 2.1, the opening of a bandgap requires widths close to 5 Å. The other key requisite is the structural precision needed to preserve the electronic properties of graphene and GNRs. Both the edge structural disorder and the presence of lattice defects can induce localized states [3] that critically affect the mobility of electrons and break down the relation between GNR edge topology and its electronic properties [4]. These requirements are beyond the precision of current lithographic or other top-down fabrication approaches. Although many of these techniques succeeded in the formation of GNRs [60–63], the resulting ribbons lacked an atomically precise structure.

Nonetheless, the selectivity that top-down approaches lack can be achieved via bottom-up techniques. In particular, atomically precise graphene nanoribbons have been grown by on-surface reaction of molecular precursors, the first example being the work of Cai *et al.*, for 7-AGNR and chevron GNRs [5]. The molecular precursors act as building blocks and the substrate (usually a noble metal) acts as catalyzer to fuse them into the final GNRs. Thus, an adequate precursor design allows the growth of a broad range of GNRs (Figure 2.10) with the required edge and structure selectivity. Moreover, the molecular design opens up the possibility of controllably doping GNRs by substituting atoms or adding functional groups to the precursor structure (as discussed in Part II).

The growth process occurs in three steps. First, the molecular precursor is sublimated in UHV conditions on a metallic sample. This imposes a constraint on the precursors themselves, normally on terms of molecule size, since the precursor has to sublimate without degrading or reacting in the crucible.

Polymerization

The second step is the on-surface coupling reaction, which joins the precursors into polymeric chains. This reaction is generally based on the Ullmann C-C coupling [65] (Figure 2.9) and it involves the on-surface dehalogenation of two molecular species followed by the reaction of the dehalogenated radicals. As seen in Figure 2.10, the majority of molecular precursors used for growing GNRs possess halogen atoms at certain positions. This allows to steer the reaction pathway for the monomers.

The dehalogenation process requires overcoming an energy barrier, which is tipically provided by annealing the sample. The energy depends on both the halogen species

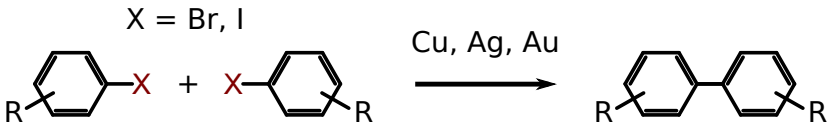

Figure 2.9: Ullmann coupling process which classically describes the reaction between aryl halides and copper. The coupling can be induced on the surface of noble metals, but also in some particular insulators like TiO_2 [64]

and the reactivity of the surface; C-I breaks at lower temperature than C-Br and Cu is the most reactive substrate followed by Ag and Au [66–71]. The energy required for the dehalogenation process is also dependent on the structure of the monomer [72]. For example, DBBA and cDBBA (Figure 2.10 III and IV, respectively) have the same chemical composition, however the dehalogenation step occurs $\sim 50\,^{\circ}\mathrm{C}$ lower in the case of cDBBA (IV), since the Br atoms lay closer to the surface compared to DBBA (III) [73].

Following the dehalogenation, the radicals must diffuse and couple between themselves to form polymeric chains. This process is mainly governed by the energy barriers associated with the diffusion of the monomers in the surface. According to *ab initio*

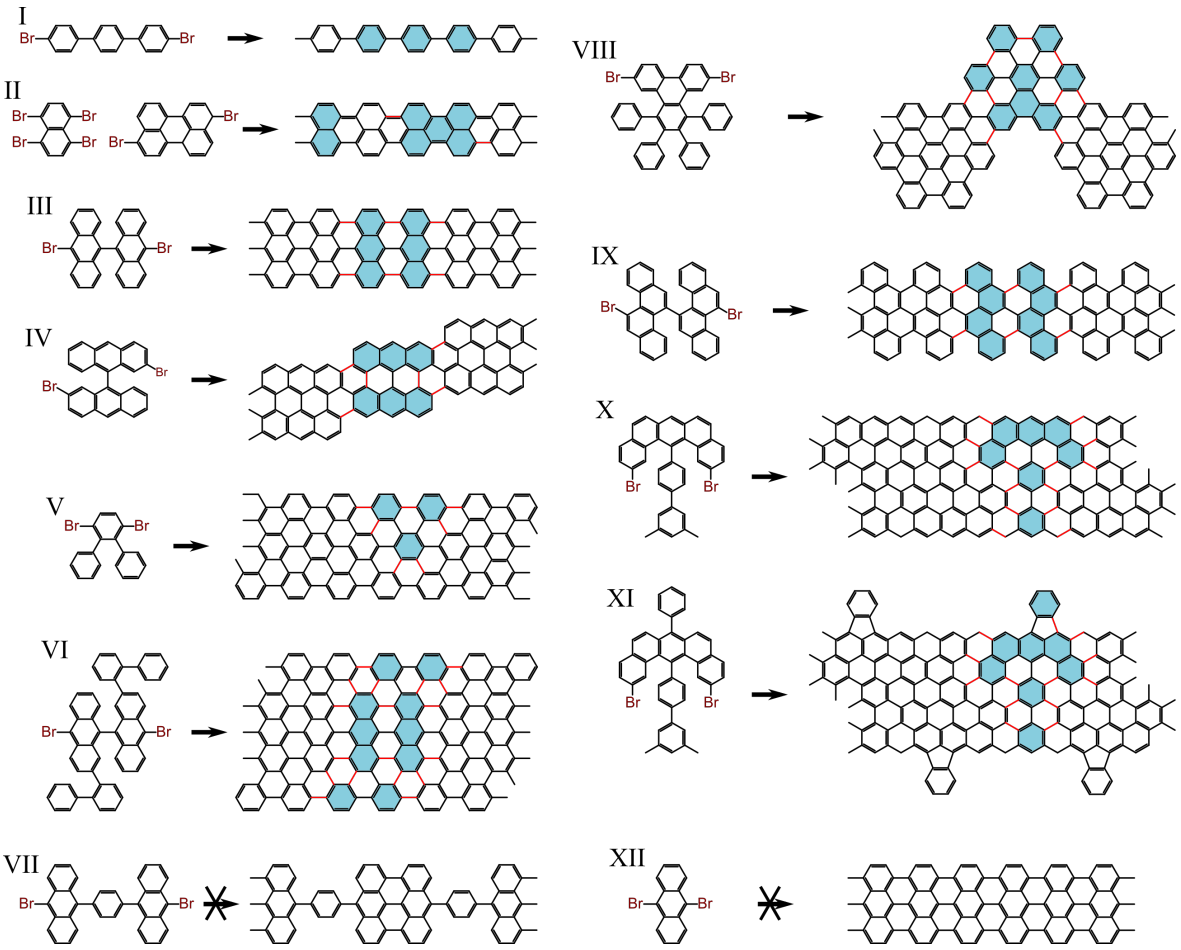

Figure 2.10: Molecular precursors and the different types of GNRs obtained via on-surface polymerization and cyclodehydrogenation. The GNRs have shaded in blue the initial precursor and the bonds formed during the cyclodehydrogenation step are highlighted in red. Monomers I, II, III (DBBA), V and VI yield 3-AGNRs [40,74], 5-AGNRs [42,75], 7-AGNRs [5] and 13-AGNRs [39]. Monomer IV leads to (3,1)-chiral GNRs [73] and monomer VIII leads to chevron GNRs [5]. Monomers IX, X and XI lead to cove-edge zig zag ribbons [41], 6-ZGNRs and edge modified 6-ZGNRs [43]. Monomers VII and XII illustrate molecules that do not yield the expected GNRs due to steric repulsions between radicals.

calculations [67], the energy barriers are smaller in Au(111), followed by Ag(111) and they are significantly larger in Cu(111) surfaces. Once the molecules diffuse to close positions, the energy cost to couple the radicals is relatively small in all surfaces [67]. Again, the reaction between radicals is also dependent on the molecular geometries. For example monomers VII and XII (Figure 2.10) do not lead to polymeric chains after dehalogenation. An intuitive explanation arises from the fact that the anthryl groups of these molecules lay flat on the surface. The coupling between two radicals is therefore hindered by the steric repulsion between the hydrogens surrounding the active carbon atom. This steric intermolecular barrier between hydrogens is reduced for non planar precursors and thus, the reaction is favored. Most of the molecules in Figure 2.10 possess a certain degree of steric hindrance between their subunits that makes them non planar. In the case of molecules III, IV and VI these distortions allow a better on-surface growth of polymeric chains, as the anthryl units between two radicals can join unhindered.

Cyclodehydrogenation

The third and final step is the cyclodehydrogenation process, which involves the formation of the missing C-C bonds in order to create the final GNRs. The majority of polymer chains are non planar due to steric repulsions. During this step, the polymers lose the hydrogen atoms that drive these repulsions followed by the formation of benzenoid rings and, as a result, the polymer structures planarize (Figure 2.10 red bonds). The cyclodehydrogenation process is also catalyzed by the substrate. First of all, the π-stacking interaction between polymers and surface tends to induce planar conformations, intensifying steric forces between hydrogens and increasing the overall energy of the polymer chain. As a result, the energy barriers for the dehydrogenation are reduced. Secondly, surface atoms act as catalysts supporting the cleavage of C-H bonds, as shown by means of *ab initio* calculations for the case of DBBA (Figure 2.10 III) on Au(111) [76]. Substrates with larger reactivity can lead to cyclodehydrogenations processes at lower temperature. For example, the cyclodehydrogenation of precursor DBBA on Ag(111) occurred at only at 177 °C [77]. Notably, this process occurred before the Ullmann coupling of the monomers and, as a result, the synthesized ribbons were highly interlinked. This exemplifies the importance of the hierarchy between polymerization and cyclodehydrogenation steps. Since the only control over these two reactions is the annealing temperature and annealing time, it is best that their activation energies are properly differentiated, in order to obtain high quality GNRs.

After a proper sequence of these three steps, the final GNRs have all their edges saturated by hydrogen, present high aspect ratios, low defect densities [5,39–44,74,75]. This allows a perfect study of their properties and an easy correlation with theoretical models.

2.5 Conclusions

We have described the electronic properties of GNRs depending on their edge topology. The band structure of N-AGNRs can be thought as discrete $k_\perp$ plane cuts of graphene's

band structure, projected into the growth direction, i.e. ΓM. In a Tight Binding approach, the cuts define mainly two types of N-AGNRs: semimetallic ($N = 3p + 2$) and semiconductor ($N = 3p$ and $N = 3p + 1$) with a bandgap that decreases with increasing ribbon width. This bandgap behaviour splits into three different trends whenever we take into account the difference in bond lengths at the edges of the ribbons. The associated increase in the hopping term ends up opening a small bandgap in the $3p+2$ family of ribbons. Additionally the $3p$ and $3p+1$ families split into two different bandgap progressions. These three families and their electronic properties can also be rationalized by means of Clar's formalism, where each family possess one ($N = 3p$), two ($N = 3p + 1$) or more than two ($N = 3p + 2$) Clar formulas which qualitatively relate to the different bandgap trends.

Similarly, ZGNRs electronic structure can be thought as $k_\perp$ cuts of graphene band structure projected along the ΓK direction. However, for ZGNRs, this cuts are not straight lines, as the ribbon edge atoms belong to different sublattices. The cuts characterize ZGNRs as semimetallic and two complex $k_\perp$ solutions define two localized edge states. These edge states do not arise from the graphene band structure, but are intrinsic to the presence of a zigzag edge. Additionally, the edge states have basically amplitude in one of the sublattices. This, combined with a large density of states at the Fermi level, turn edge states spin polarized, with opposite spin state in each side of the ribbon since they correspond to a different sublattice.

Clar's formalism allows a intuitive picture of the origin of the ZGNR edge states based on the existence of localized radicals. The formation of edge radicals can be energetically favorable for ZGNR, as it allows to establish more Clar sextets. As a result, for wide enough ZGNRs, the formation of edge states can be described as the combination of several possible radical sites along an edge.

Finally we have described tge experimental approach that will be used in this thesis to grow GNRs, based on on surface reactions of molecular precursors. A clever precursor design allows the growth of atomically precise GNRs. This bottom-up method involves the Ullmann-like coupling of these precursors on top of a metallic substrate. As a general guideline, a more reactive substrate tends to lower the dehalogenation energy barrier, but also increases the diffusion barriers of the dehalogenated precursors. After the monomer coupling, the polymeric chains have to undergo a cyclodehydrogenation step, where the excess of C-H bonds is removed, and C-C bonds are formed. The surface facilitates this process increasing the steric repulsions on the polymers and reducing the cyclodehydrogenation energy barriers. Again, more interactive surfaces tend to further reduce these energy barriers.

Chapter 3

Pristine 7-AGNR, a case study

The 7-AGNR was the first nanoribbon grown by on-surface synthesis using molecular precursors [5]. It quickly became the staple system to produce a large variety of ribbon structures and to study their chemical and physical properties. Many experimental and theoretical works emerged concerning the electronic and optical properties of 7-AGNR studied by STS [7, 45, 46, 77–80], DFT [51, 81], ARPES [45, 82], HREELS [83, 84] and Reflectance Difference Spectroscopy [85]. The growth mechanism of 7-AGNR has also been deeply studied by STM-AFM [5, 86], Raman Spectroscopy [5, 87], XPS [69–71] and DFT [67, 76, 88, 89] in order to understand and extend the on-surface process to different substrates. In addition, 7-AGNRs have also been the template to study electronic transport [90] and friction properties of GNRs [91].

In this chapter we review several aspects regarding the growth of 7-AGNR and their properties as revealed by STM. We will show the result of lateral fusion between 7-AGNRs and how to potentially incorporate surface atoms inside the structure of the ribbon. Finally, we will focus on the electronic properties of these ribbons by means of STS and DFT. This will allow us to set the main concepts to understand the doping of 7-AGNRs in part II of this thesis.

3.1 On-surface growth of 7-AGNRs on Au(111)

The molecular precursor used to grow 7-AGNR is the 10,10'-dibromo-9,9'-bianthryl (DBBA, Figure 3.1a). DBBA consists in two linked anthracene moieties with two bromine atoms. The steric repulsions between the hydrogen atoms of each moiety induce a cross shaped non planar conformation in the gas phase. We sublimated the precursors from a Knudsen cell kept at $\sim 170°$ on top of a Au(111) substrate held at room temperature. Upon deposition, the molecules arrange in π-stacked islands (Figure 3.1b). These islands consist of monomer chains, that preferentially align following the herringbone reconstruction. Upon close inspection, the monomers exhibit their three dimensional structure (Figure 3.1c) as a pair of bright lobes in alternating positions, corresponding to the highest section of each anthracene moiety. As seen in the profile in Figure 3.1d, the apparent height of the lobes is close to 1.5 Å and the spacing between them is 1 nm, in reasonable agreement with the molecular size.

Following the evaporation step, we annealed the sample to 200 °C for ten minutes,

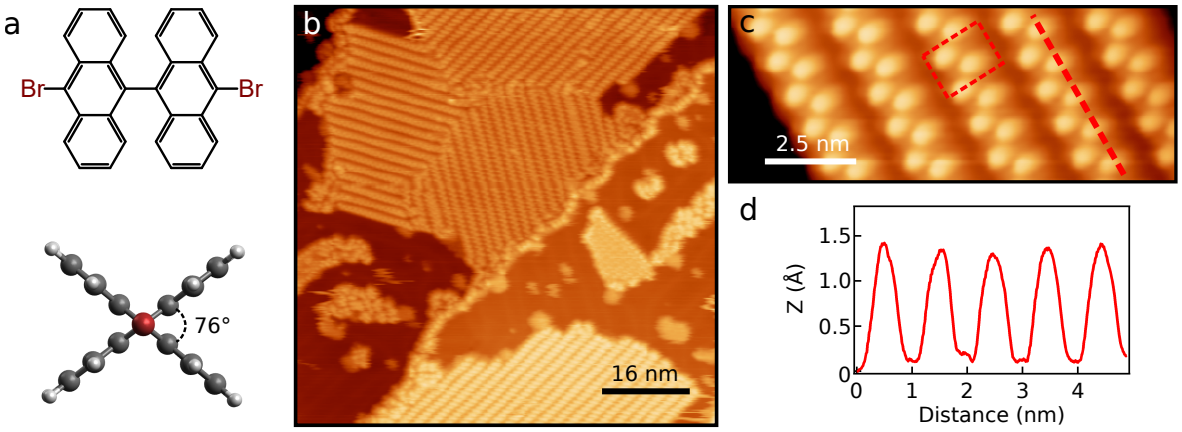

Figure 3.1: (a) Molecular structure and gas phase structure of 10,10'-dibromo-9,9'-bianthryl (DBBA). The anthracene moieties are rotated $76°$ between each other. (b) Overview of DBBA monomers deposited on top of a Au(111) surface. The monomers self assemble into islands. Three different orientations are observed with $120°$ between them. (V_s=1.7 V, I_t=51 pA)(c) Small scale image of the DBBA chains, which show an alternating sequence of protusions, associated to the extrema of the anthracene moieties. The dashed square marks a single DBBA molecule. (V_s=0.76 V, I_t=67 pA). (d) Topography profile along the monomer chains. The spacing of the protusions ($\sim$1 nm) agrees with the distances between anthracenes.

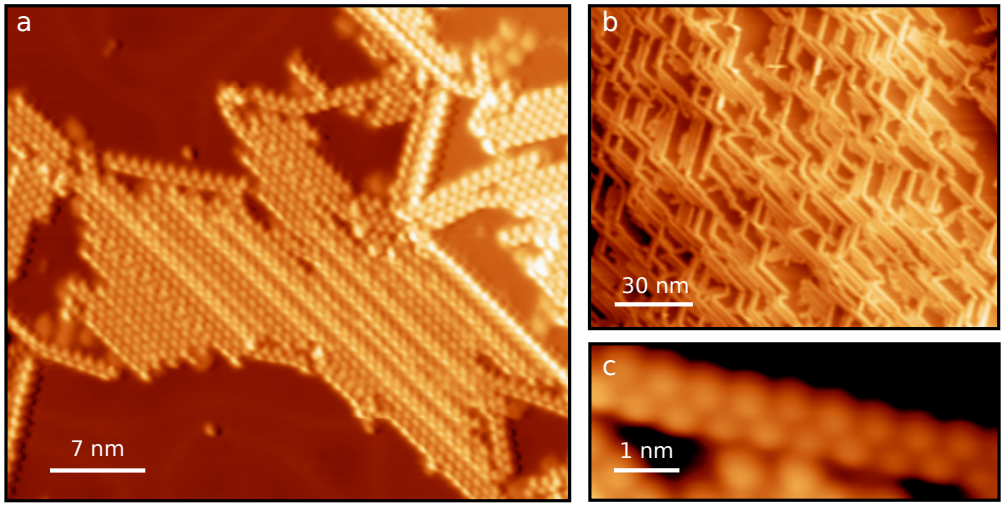

Figure 3.2: (a) Overview of a DBBA polymer island, showing the compactness and alignment of the polymer islands. (V_s=1 V, I_t=84 pA). (b) Large scan overview showing the terrace reconstruction caused by the polymers. The step edges are all decorated with polymers and present sharp $120°$ orientations (V_s=1.2 V, I_t=130 pA). (c) Small scale image of a DBBA polymer, showing the characteristic alternating protusions along the length of the chain. (V_s=1.5 V, I_t=81 pA)

in order to induce the dehalogenation and polymerization, i.e. Ullmann-like coupling, of the DBBA precursors. As discussed in the previous chapter, Au(111) is the least reactive substrate among the noble metals, and thus the dehalogenation temperature

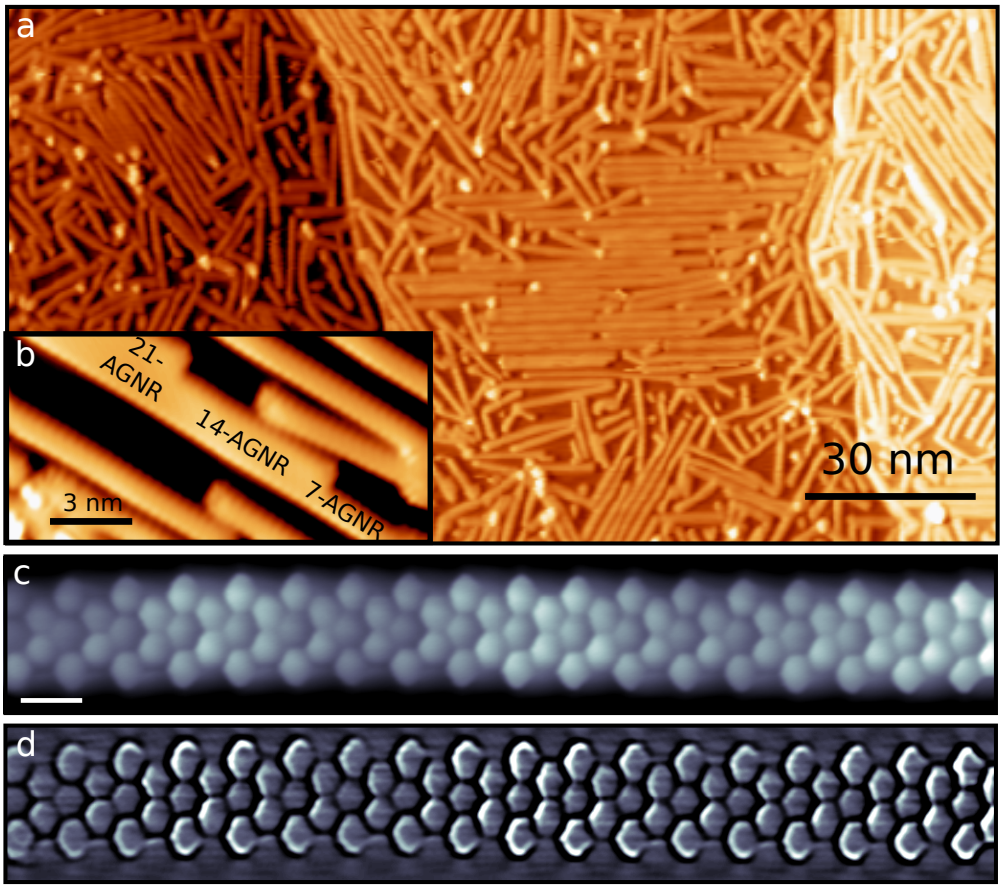

Figure 3.3: (a) Overview of 7-AGNR on a highly covered sample. (V_s=1.5 V, I_t=93 pA). (b) Small scale image of three laterally fused 7-AGNR, creating a 7-, 14-, 21-AGNR heterostructure. (V_s=2 V, I_t=140 pA). (d) Constant height dI/dV map of a 7-AGNR showing its intramolecular resolution. (V_s= 5 mV Z_{off}=-0.6 Å V_{rms}=4 mV f= 760 Hz. OFC: V_s= 22 mV I_t=100 pA, scale bar is 5Å) (e) Laplacian filtered image of panel *d*, highlighting the backbone structure of the 7-AGNR.

is rather high. The rection results on long polymeric chains as seen in Figure 3.2a. After this reaction step, and for the monomer coverage in Figure 3.1b, we observe a reconstruction of the atomic terraces of the surface (Figure 3.2b). All terrace steps are covered by polymeric chains, and the reconstrucion results in sharp 120 ° directionalities on the terraces. As in the case of the DBBA monomers, the polymers tend to align into π stacked islands. A close inspection shows that the polymer islands are more compact than the DBBA ones, and that the chains consist, again, in an alternating arrangement of protusions (Figure 3.2c), with an apparent height of 3 Å. This is consistent with the polymer structure, which preserves the steric hindrance observed in DBBA molecular precursors [5].

Further annealing to 400°C for 30 seconds yields the final 7-AGNR structures. In the case of DBBA polymers, first principle calculations showed that the cyclodehydrogenation step is most likely to occur first at the extreme of the polymers [76]. Once a C-C bond is created, the energy to form additional C-C bonds drastically diminishes, suggesting a cascade cyclodehydrogenation occurring all along the polymer. The

resulting 7-AGNR can be seen in Figure 3.3a. The ribbons are no longer arranged in π-stacked islands, even at high coverages. However, it is possible to observe large groups of aligned ribbons. STM images with CO functionalized tips clearly resolve the intramolecular structure of the ribbons (Figure 3.3d,e), showing that 7-AGNR grown by this method can attain lengths of tenths of nanometers with no structural defects.

The GNRs may undergo unwanted coupling reactions between themselves, such as T shaped links or lateral ribbon fusions, which involve edge dehydrogenations. At particular high coverages, such as that of Figure 3.3a, lateral fusion of 7-AGNRs becomes more frequent. These lateral reactions most probably follow the same pathway as intrarribbon cyclodehydrogenations, i.e. creation of an initial C-C bond between two aligned ribbons and C-C bond formation all along the nanoribbon edge in a zipping fashion. The laterally fused ribbons define GNR heterostructures containing sections of ribbons of different widths and belonging to different families and hence different electronic bandgaps (Figure 3.3b).

The yield of lateral cyclodehydrogenations can be increased by annealing high coverage samples to higher temperatures. Figure 3.4a shows the result of annealing the sample corresponding to Figure 3.3a to 470°C for 15 minutes. The overview shows a significant widening of the original 7-AGNRs, resulting in structures up to 28-AGNRs. However, the process is uncontrolled, and the ribbons present a wide variety of interlinkages and defects.

After the higher temperature annealing, we observe in some occasions a chain of protrusions aligned along the joint between two fused ribbons (Figure 3.4b). The protrusions have the same periodicity of the AGNR unit cell and form structures that can extend over more than 10 nm. A possible assignment of these features is that they correspond to a chain of un-detached hydrogen atoms bent upwards due to the steric hindrance between both ribbons. However, high bias pulses ($\sim$ 3 V) were unable to remove the protusions, unlike the case of hydrogens in the edges of AGNRs [78]. We can

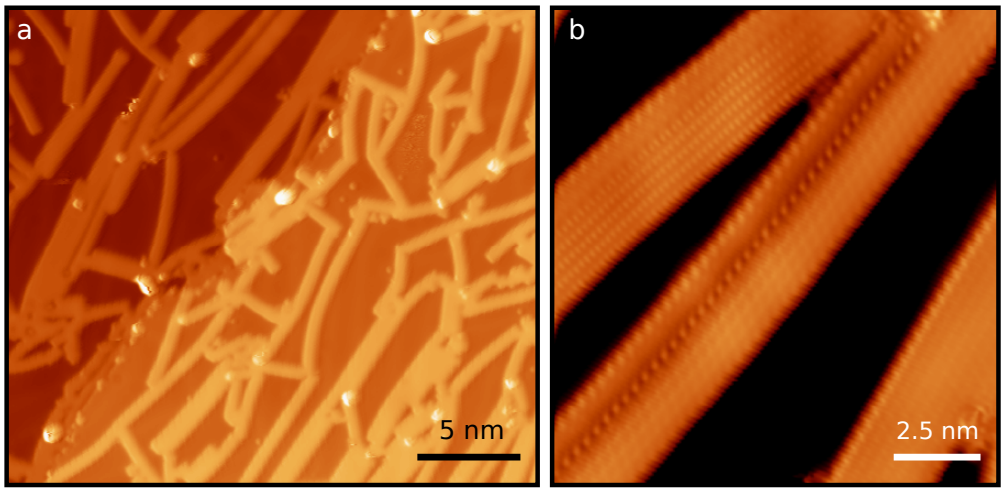

Figure 3.4: (a) Overview of the postannealed sample. The majority of GNRs become wider and interlinked. (V_s=0.6 V, I_t=170 pA). (b) Close up image of a hindered lateral fusion. Between the 7-AGNR and the 14-AGNR we observe a chain of protrusions which we attribute to the presence of trapped adatoms. (V_s=100 mV, I_t=1.1 nA)

also discard that they are residual bromine atoms from the dehalogenation step since XPS studies on 7-AGNRs demonstrated that bromine desorbs from Au(111) surfaces above 250°C [70]. We instead consider that these features are gold adatoms trapped between the ribbons during an unsuccessful lateral fusion. At 470°C, temperature where the Au(111) reconstruction already takes place, gold atoms have large mobility, becoming a two-dimensional gas of adatoms. They participate in reactions and, in this case, it is probable that they mediate the lateral fusion by creating a metal-organic intermediate state previous to C-C coupling [92, 93]. The regularity and length of the structures observed also points towards this hypothesis. Although, there is no conclusive proof to confirm any of the options, these observations suggest that AGNR could be used as template to include heteroatoms, such as transition metal atoms, in the GNR structure.

Moreover, we find that some ribbons have an additional faint topographic feature inside wide, fused GNRs (Figure 3.5a). This feature has a strong electronic fingerprint close to 1.2 V which resembles a chain of protrusions (Figure 3.5b), again with the AGNR unit cell periodicity, similar to the adatoms in Figure 3.4b. We note as well, that the adatom chains in Figure 3.5a also present a similar although fainter feature at this energy (Figure 3.5b). The resemblance between the electronic fingerprints suggests a similar origin of both the adatom chains and its fainter counterpart within fused GNRs. However, their distinct topographic shapes point towards different morphological structures.

We performed STMH [23] to better understand the ribbon structure hosting these strong electronic chain-like features. As seen in figure 3.5c and d, there is a clear interface between a 7-AGNR section and the wider GNR section. We observe the presence of four lobes in the top positions of the AGNR edge, periodically distributed along the interface. The origin of such contrast is unknown and perhaps is related to a coordination of the radicals at the the ribbon edge with trapped adatoms (Figure 3.5d). However, the STMH images do not provide a clear picture of the structure of the interface, and further experiments are required to confirm our hypothesis. CO functionalized AFM images could resolve the intramolecular structure of the GNR's interface and shed light on the presence of adatoms and the bonding mechanism between both GNRs.

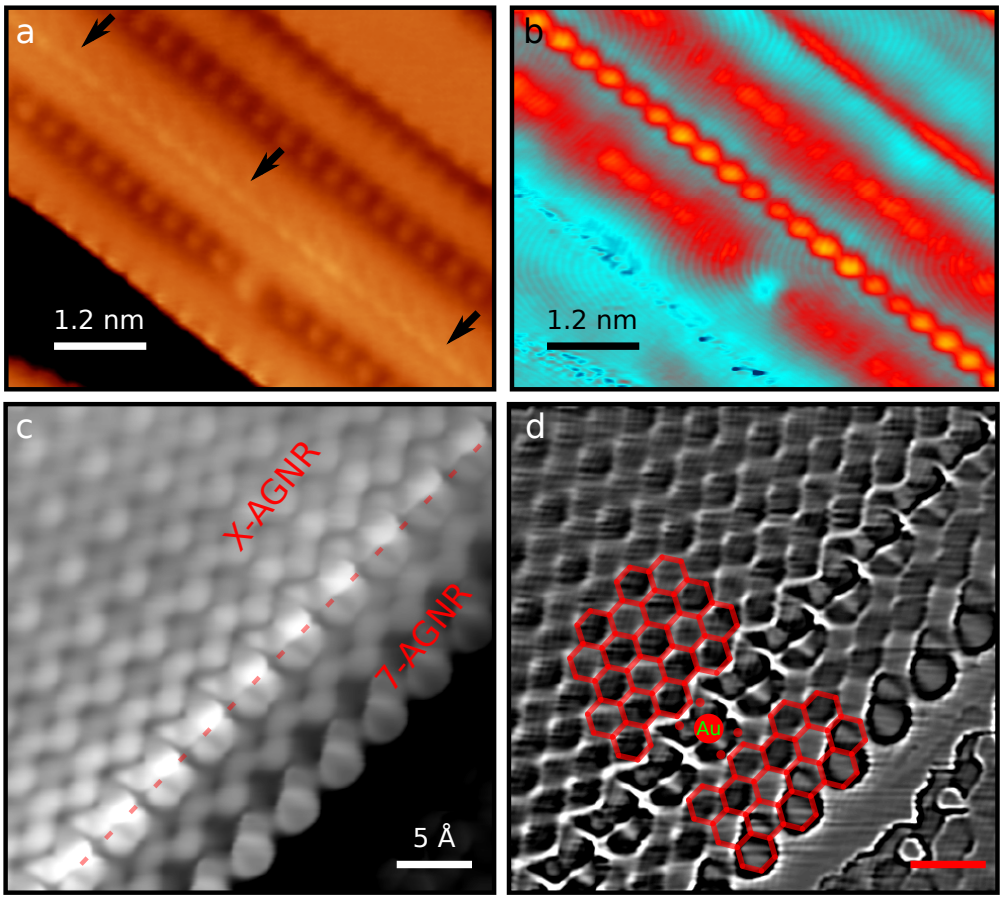

Figure 3.5: (a) Small scale image of a group of ribbons showing chains of addatoms and a faint feature along the backbone of the fused central ribbon (black arrows). (V_s=1 V, I_t=84 pA). (b) Constant current dI/dVmap of panel *a* showing the strong periodic electronic fingerprint along the ribbon. The adatom chains show similar fingerprints, although its intensity is weaker.(V_s=1.2 V, I_t=630 pA, V_{rms}=14 mV f=760 Hz). (c) Constant height STMH current image of a 7-AGNR joining a wider AGNR. The interface (delimited by a red dashed line) shows the strong electronic fingerprint of panel b. (Z_{off}=5 Å, V_s=-20 mV, open feedback conditions: V_s=100 mV, I_t=2 nA) (d) Laplacian filtered image of panel *c*, which allows to better resolve the intramolecular structure. Overlayed in red is the GNR structures and a proposed coordinated structure between both ribbons and adatoms.

3.2 Electronic structure of 7-AGNR

We now turn to discuss the electronic properties of 7-AGNR, which will serve as base concepts for the following chapters. The 7-AGNR belongs to the $3p+1$ AGNR family which has the largest band gap among the three AGNRs families [49, 50]. Figure 3.6a shows the band structure and PDOS of a free standing 7-AGNR, calculated by DFT simulations in the LDA formalism. The CB and VB are almost parabolic bands, with their maxima at Γ defining a bandgap of 1.6 eV. GW calculations, which incorporate electronic correlations, increase this bandgap up to 3.7 eV [45, 50]. It is worth noting that the CB+1 and VB-1 are close in energy to the frontier bands. In the case of ribbons laying on a surface, the bandgap is reduced compared to the GW calculations since the substrate polarization partially screens the electron-electron interactions [51, 94, 95].

STS on a 7-AGNR (Figure 3.7a) on Au(111) shows two main features corresponding to the Van Hove Singularities associated with the VB and, for reasons that will be discussed later on this section, the CB+1. Depending on the criteria chosen to define the band onsets on the actual spectra, the energy values for the VB and CB+1 may vary [7, 45]. Recently, Söde *et al.* [46] determined that the bands onsets lay between the maximum and half maximum of the STS peak. Nevertheless, the onsets can also be determined by analyzing the Fourier Transform of the standing wave patterns on finite ribbons, resulting on $E_{VB} = -0.84 \pm 0.05$ eV and $E_{CB+1} = 1.67 \pm 0.03$ eV [46].

Between both bands we also observe the fingerprint of the Au(111) Shockley surface state at around -450 mV. This value is slightly upshifted respect to the one on clean Au (111), which lays at -500 mV [96]. This is due to the weak confinement that the ribbons impose on the surface electrons below [97–100].

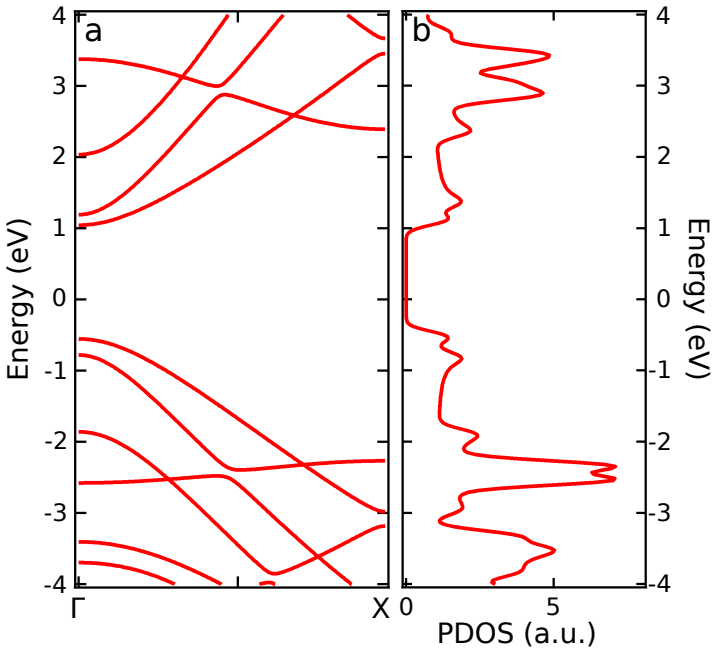

Figure 3.6: (a) Band structre of a free standing 7-AGNR calculated by DFT in the LDA formalism. The CB and VB are almost parabolic, and the CB+1 and VB-1 lay very close in energy. (b) DOS projected onto the carbon atoms of 7-AGNR.

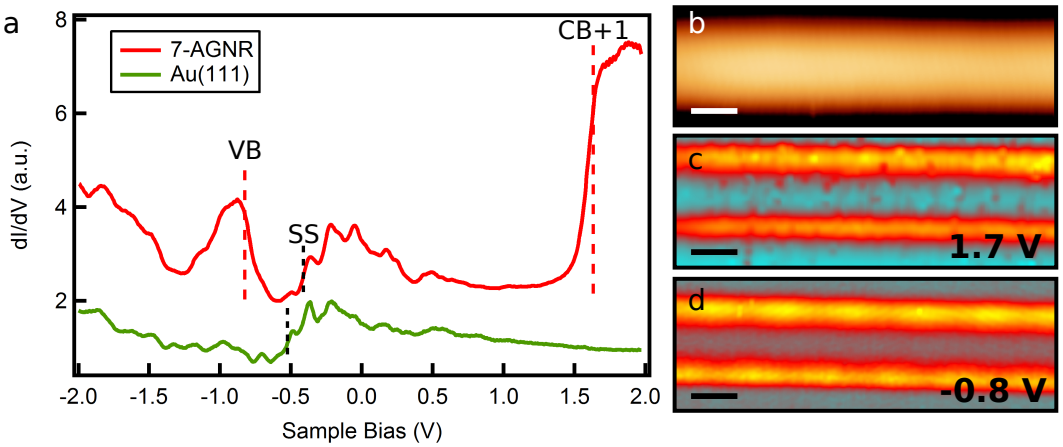

Figure 3.7: (a) Differential conductance (dI/dV) spectra taken on the edge of a 7-AGNR (red spectrum) and on the bare gold surface (green spectrum). Red dashed lines mark the onsets of the VB (-0.84 V) and CB+1 (1.67 V). Black dashed lines mark the onset of the Au(111) Shockley surface state (SS), slightly upshifted (∼50 mV) beneath the GNR. (Open feedback parameters: V_s= 1.0 V, I_t= 0.41 nA, V_{rms}=12 mV, f = 767.7 Hz) (b) STM topography of a 7-AGNR and constant current dI/dV maps acquired at the onset of the CB+1 (panel *c*) and at the onset of the VB (panel *d*). The maps show a localized contrast along the edges of the ribbon. (dI/dV maps feedback conditions: I_t= 1 nA, V_{rms}= 18 mV, f = 767.7 Hz.

Constant current dI/dV maps of the VB and the CB+1 show a peculiar localized edge contrast along the ribbon (Figure 3.7c and d). This differs with the shape of the wavefunctions for the 7-AGNR bands at the Γ point (Figure 3.8a), which extend all over the ribbon backbone. However, recent works [44,46] have shown that the cause of the localized edge contrast is in fact the symmetry of these wavefunctions. In the case of the VB and the CB+1, the wavefunction amplitude sign oscillates across the ribbon width (y direction). When taking into account the evanescent decay of these electronic states, the sign oscillation translates into a faster decay rate at the center of the ribbon due to the superposition of + and − components of the wavefunction amplitude. On the other hand, the wavefunction at the ribbon edge does not suffer such a strong sign cancellation, and therefore its decay is slower along the z direction. Since STM probes the evanescent electronic states, the final contrast observed for the VB and CB+1 is localized around the edges of the ribbon (Figure 3.8b).

The symmetry of the wavefunctions also explains the arbitrary assignment that we previously did, that is, considering the spectral feature at 1.6 V (Figure 3.7a) the CB+1 onset instead of the CB one. The wavefunctions of the CB and VB-1 (Figure 3.8a) present strong sign oscillation both along (x direction) and across the ribbon. The oscillations result in a faster decay of the CB and VB-1 features along the z direction over all the ribbon. Therefore, both bands are hardly detected at typical tunneling distances (Figure 3.8b).

To detect signatures from these fast decaying bands, we acquired dI/dV maps in constant height mode with a CO functionalized tip. At tunneling currents close to 10 nA, we resolve the CB at 1.54 V (Figure 3.9a). The observed contrast qualitatively

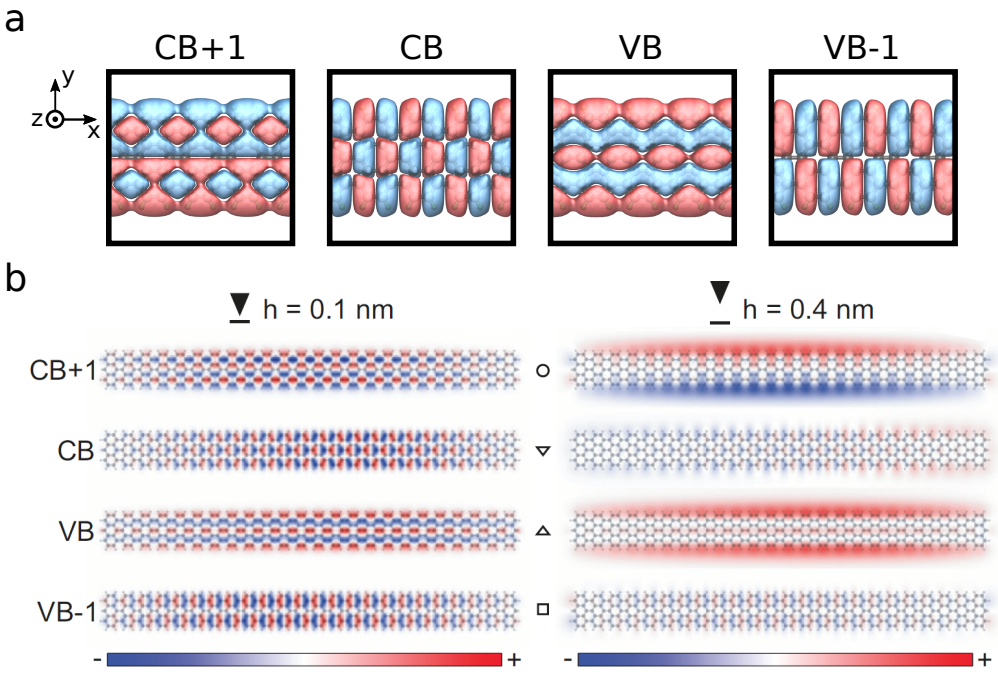

Figure 3.8: (a) Wavefunctions of CB+1, CB, VB and VB-1 at the Γ point. All wavefunctions amplitude oscillate strongly along the y direction. The CB and the VB-1 also oscillate along the x direction. (b) Effect of the tip distance on the probed bands, extracted from [46]. At small tip-ribbon distances (left) the bands have not decayed significantly. At typical tip-ribbon distances (right), the CB and VB-1 have strongly decayed and they are no longer visible. In the case of the CB+1 and VB, only the edge components of the wavefunctions remain.

agrees with a *p*-wave tip image of the wavefunction shown in Figure 3.8a (see chapter 1.2). On the other hand, the features observed at the energy of the CB+1 onset (Figure 3.9b) do not have such a direct resemblance to the band wavefunction. Compared to the CB, the edge contrast is blurrier, and the center contrast has additional maxima, creating a chessboard like pattern. The reason behind this lack of clear contrast could be an overlap between CB and CB+1 features, which lay very close in energies. For instance, the blurred edge in the CB+1 map, could be a fingerprint of said band, while the contrast at the center may be governed by the CB features.

Regarding the filled bands, the VB shows a contrast pattern consisting in a series of half circles at the center and a modulated edge contrast (Figure 3.9c). This is in good agreement with DFT image simulations of the VB for a mixed *s* and *p*-tip [81]. In the case of the VB-1, at -1.5 V (determined by ARPES [45]), we observe a contrast not easily identifiable with the band wavefunction, similar to the situation of the CB+1 (Figure 3.9d). This could be again due to an overlap between VB and VB-1 features and/or due to tip-ribbon distances being still large to detect fingerprints from the VB-1. In any case, DFT simulated images taking into account all four bands are needed to further corroborate our dI/dV map interpretations.

Another useful method to extract information from GNR bands is the Fourier Transform of STS spectral maps. Electrons scattering against the ends (or other barriers,

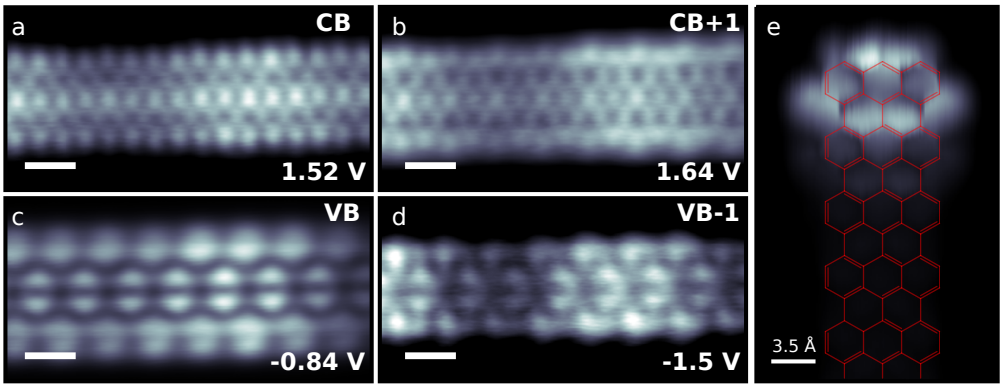

Figure 3.9: Constant height dI/dV maps using a CO functionalized tip of a 7-AGNR at the onsets of the (a) CB, (b) CB+1, (c) VB and (d) VB-1 (as expected from ARPES measurements [45]). Scale bars correspond to 5 Å. (e) Constant height dI/dV map using a CO functionalized tip of the zigzag end of a 7-AGNR, with its structure overlapped in red. At energies close to E_F, the Tamm state superimposes to the atomically resolved structure of the ribbon. (Imaging parameters: (a,b) Z_{off}=-2.2 Å (c) Z_{off}=-1.9 Å (d) Z_{off}=-2.6 Å V_{rms}=8 mV, f= 760 Hz. (e) V_s=50 mV Z_{off}=-0.6 Å V_{rms}=4 mV, f= 760 Hz. Open feedback parameters: (a-d) V_s= 21 mV I_t= 110 pA. (e) V_s= 200 mV I_t=50 pA.)

see chapter 6) of the ribbon generate standing wave patterns with a wavenumber and energy relation characteristic of each GNR band. The Fourier Transform of these patterns provides the energy dispersion of the confined bands. By fitting a free electron model ($E(k) = E(k=0) + \hbar^2 k^2/2m^*$) to the energy dispersion, the band's onset and its effective mass can be obtained. Using this method, Söde *et al.* obtained the onset of the CB, $E_{CB} = 1.52 \pm 0.04$ eV defining a transport bandgap for 7-AGNR of $E_g = 2.37 \pm 0.06eV$ [46], in agreement with GW and DFT calculations taking into account image charge corrections [45, 51].

Concerning the effective masses of the GNR bands, they obtained a reasonable agreement between DFT and FT-STS. However, the values obtained for the VB by this method, $m^*_{VB} = 0.41 \pm 0.08 m_e$ [46] and $m^*_{VB} = 0.43 \pm 0.03 m_e$ [8], differ by a factor two with the effective masses obtained by ARPES measurements, $m^*_{VB} = 0.21 m_e$ [45] and $m^*_{VB} = 0.18 m_e$ (chapter 5). The origin of this discrepancy is still unknown, and surprisingly it has not been reported to occur for 9-AGNR [44].

Finally, we also observe the presence of the Tamm state localized at the zigzag ends of the ribbons close to E_F (Figure 3.9e) [78, 80, 81, 88]. These edge states are predicted to host a localized spin of opposite polarization at each ribbon end [101]. On top of Au(111), these edge states appear as a single spectroscopic feature [78, 90], probably degenerated. However, on top of NaCl, the states are splitted up to 1.9 eV [80] owing to the decoupling provided by the insulator. Although this localized state may be of relevance for contacts between GNRs, the following chapters are going to focus mainly on the bulk properties of 7-AGNR.

3.3 Conclusions

In summary, we have described the growth mechanism of 7-AGNR on Au(111) using DBBA as molecular precursors. Both the unreacted DBBA monomers and their polymer counterparts organize in self assemble π-stacked islands. The steric hindrance between the anthracene moieties of the molecule (polymer) is reflected in a three dimensional structure of the monomer (polymeric) chains. This steric repulsion is also the driving force behind the cyclodehydrogenation step, which planarizes the polymeric chains and results in atomically precise 7-AGNR.

On highly covered samples, the cyclodehydrogenation is also likely to occur between adjacent ribbons. This creates heterostructures containing ribbon sections of different widths which belong to different AGNR families. The yield of these lateral GNR dehydrogenations can be increased by annealing the ribbons to higher temperatures. The process renders wider ribbons, although their precise width cannot be controlled. After the annealing we observe some unsuccessful lateral fusions. Between the ribbons, we resolve a chain of protrusions. We propose that gold adatoms are trapped between the ribbons, mediating the bonding between the ribbons. On certain occasions, the topographic interface between ribbons is much fainter and it can only be resolved by its electronic fingerprint at $\sim$1.2 V or by high resolution STHM imaging.

Regarding the electronic structure of 7-AGNR, STS usually probes only the VB and the CB+1 at -0.8 V and 1.7 V, respectively. Moreover, the electronic signatures are significantly stronger at the edges of the ribbon. The reason behind the "missing" bands and the localized edge contrast is the symmetry of the bands wavefunctions. Wavefunctions with strong sign oscillation along and across the ribbon axis, as the case of the CB and VB-1, result in states that decay quickly into the vacuum and thus are not easily probed by the STM tip. On the other hand, wavefunctions with sign oscillations only across the ribbon axis, i.e. CB+1 and VB, result in states that decay quickly at the center of the ribbon but slowly at its edges. Therefore, these bands show a localized edge contrast in both dI/dV maps and spectra.

Spectral signatures of all four bands (CB, VB, CB+1 and VB-1) have been detected by constant height dI/dV maps at small tip-ribbon distances, using a CO functionalized tip. For the VB and CB, there is a clear resemblance between the bands wavefunction and its conductance map. On the other hand, CB+1 and VB-1 maps yield conductance features harder to ascribe to the band wavefunction without further simulations.

Finally, the Fourier Transform of spectral maps of finite ribbons can be used to determine the bands onsets and their corresponding effective masses. This allows to define a transport bandgap of $\sim$2.4 eV for 7-AGNRs. However, there are discrepancies in 7-AGNR m^*_{VB} between ARPES and FT-STS experiments that have still not been understood.

Part II

Doping of Graphene Nanoribbons

In previous chapters we have shown that the on-surface synthesis of GNRs allows tuning the electronic structure of the ribbons via width control [5, 39–42, 44, 74, 75]. Doping of GNRs is a key aspect to further develop the possibilities of these nanostructures as alternative material for semiconductor applications. On-surface synthesis strategies allow to place substitutional heteroatoms or chemical moieties in the ribbons by selecting specific precursors. The high precision of the on-surface built structures allows to understand atomistically the effect of dopants or functional groups in the electronic structure of the ribbon. Such effects can modify the band alignment [6, 55, 102], change the band gap [103], modify the density of states (DOS) of a ribbon by inducing new bands [104, 105] or generate highly reflective electron scatterers [8]. However, full insight between doping and the consequences on the ribbon electronic structure has still not been accomplished.

Up to now, the most common on-surface approach has been the chemical substitution of carbon atoms by heteroatoms [6, 55, 102–105]. By exchanging atoms of the backbone of GNRs with other elements (Figure 3.10) a certain degree of control on the GNRs band structure has been achieved.

Nitrogen doped chevron GNRs have been grown with either two [55, 84] or four [6] nitrogen substitutes. The stronger electron affinity of nitrogen atoms drives a rigid downshift of the bands, n-doping the ribbon and as a result, turning the nanoribbon a stronger electron acceptor. Interestingly, the bands downshift increases almost linearly with the number of nitrogen substitutes, around 0.13 eV per nitrogen atom [6]. The nitrogen substitution does not affect otherwise the DOS of the ribbon, since the Nitrogen electron lone pairs in both pyridine and pyrimidine groups does not delocalize through the π-system.

On the other hand, sulfur doped 13-AGNR have been obtained by substitution of phenyl edge groups by thiophene functional groups [103]. The conjugation of the additional sulfur p electrons with the π network leads to a hybridization of sulfur orbitals with the ribbon bands. However, the small difference in electronegativity between carbon an sulfur atoms causes that the band alignment is barely modified [103],

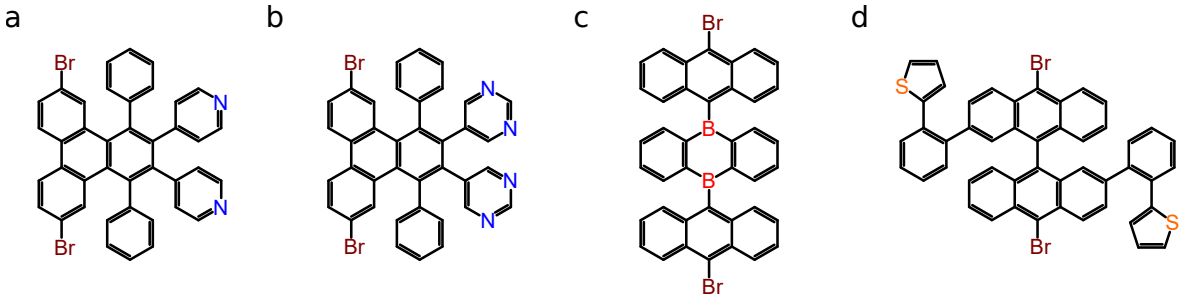

Figure 3.10: Chemical structure of different chemically substituted precursors. (a) Chevron GNR precursor with two pyridine rings (6,11-dibromo-1,2,3,4-tetraphenyltriphenylene) [55, 102]. (b) Chevron GNR precursor with two pyrimidine rings (5,5'-(6,11-dibromo-1,4-diphenyltriphenylene-2,3-diyl)dipyrimidine) [6]. (c) Boron substituted 7-AGNR precursor 9,10-bis(10-bromoanthracen-9-yl)-9,10-dihydro-9,10-diboraanthracene [104, 105]. (d) Sulfur substituted 13-AGNR precursor (2,2'-di((1,1'-dithiophenyl)-2-yl)-10,10'-dibromo-9,9'-bianthracene) [103].

in clear contrast to the nitrogen case.

Finally, 7-AGNR doped with substitutional boron atoms have been recently produced [104, 105]. The resulting ribbons, which will be discussed extensively later in this chapter, exhibit a an in-gap acceptor band.

In the following, we discuss about two doping strategies for 7-AGNR. First, we focus on the edge functionalization of 7-AGNR with CN groups, leading to n-doped 7-AGNRs. Second, we study the effect of boron substitution inside the backbone of 7-AGNRs providing a model to understand their impact on the ribbon's band structure. Finally we will discuss on the growth of 7-AGNR heterostructures with quantum dots embedded within.

Chapter 4

Doping of Graphene Nanoribbons via Functional Group Edge Modification

As previously mentioned, the most common approach to dope GNRs has been the substitution of carbon atoms by other elements with different electron affinities to either create p or n doped GNRs. However the on-surface growth approach provides further tuning flexibility, such as the addition of functional groups onto the GNR structure.

The large variety of functional groups compatible with the synthesis of molecular precursors potentially adds a huge versatility to GNRs. For example, alkyne functional groups could be used as reaction centers for further on-surface reactions, such

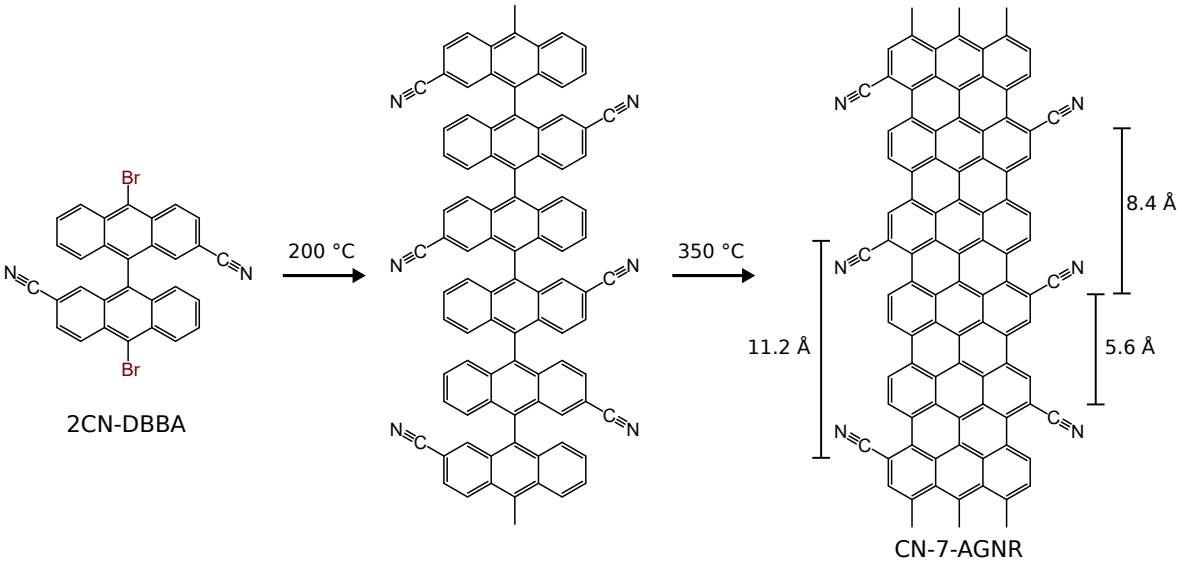

Figure 4.1: Chemical structure and reaction pathway of 10,10'-dibromo-[9,9'-bianthracene]-2,2'-dicarbonitrile (2CN-DBBA) on Au(111). The resulting ribbons have three possible intercyano distances depending on the orientation of the precursor molecule during the polymerization step.

as Sonogashira [106] or Glaser [107] couplings, that could result in precise two dimensional GNR networks. Additionally, selected functional groups could be used to attach optically active centers to the GNR, such as fluorophores [108, 109] . In terms of electronic band adjustments, electron donor or withdrawal groups can dope the electronic structure of GNR while being preferential sites for the coordination of transition metal atoms.

Here we report the synthesis on a Au(111) surface of 7-AGNR with nitrile (CN) groups substituted at the edges, which are of special interest due to their strong electron acceptor behavior. The on-surface reaction of cyano substituted dibromo bianthracene precursors (2CN-DBBA, Figure 4.1) results in the formation of 7-AGNRs with CN groups protruding from the bay regions of the AGNR. We use high resolution Scanning Tunneling Microscopy (STM) imaging to obtain reliable information on the products of the reaction, such as the detachment of some CN functional groups during the reaction process and the on-surface formation of pyridine rings. Moreover, by means of Scanning Tunneling Spectroscopy (STS) and Density Functional Theory (DFT) calculations we show that CN functionalization induces a downshift on the ribbon bands of ∼0.3 eV per CN added.

4.1 Growth of CN functionalized 7-AGNR

Molecular precursor 2CN-DBBA was sublimated at 230 °C from a Knudsen cell onto a Au(111) substrate kept at room temperature. Figure 4.2a depicts the reaction process leading to CN functionalized 7-AGNR. Following the deposition step, the sample was annealed to 200 °C for 10 minutes in order to induce the polymerization of monomer 2CN-DBBA by Ullmann coupling. Finally, the sample was annealed for 30 seconds at 350 °C in order to trigger the final cyclodehydrogenations. It is worth noting that precursor 2CN-DBBA can adopt two different prochiral configurations when confined to the flat surface, which are maintained during the polymerization step. As a result, the ribbons possess an intrinsic disorder in the CN groups distributions, leading to three possible inter CN distances (Figure 4.2a). We have not observed any conformation where two CN share the same bay region, probably because the high steric repulsion

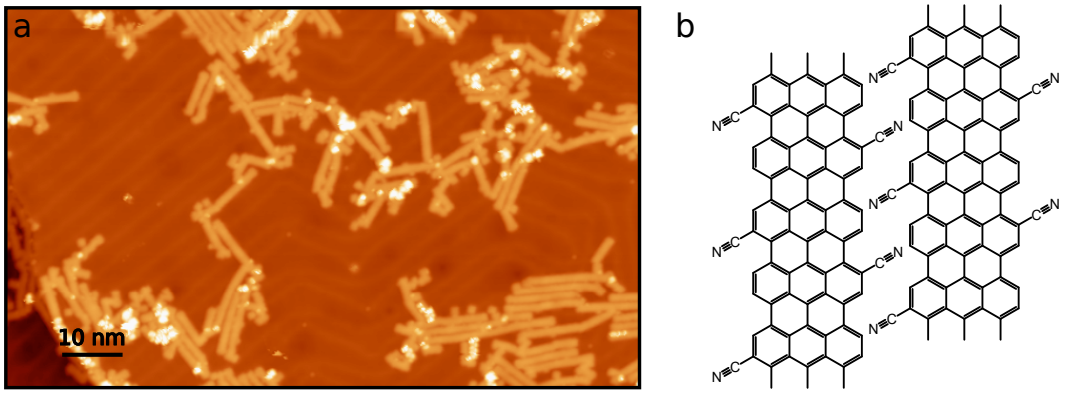

Figure 4.2: (a) Overview STM image of the reacted CN-7-AGNR (V_s=1.2 V, I_t=140 pA). (b) Proposed nanoribbon arrengement on close packed configurations.

of this substitution pattern would evolve in the fragmentation of one of the CN groups on the bay region.

Figure 4.2a shows an STM overview of the resulting ribbons. The typical lenghts are around 8 to 10 nm, much shorter than average lengths for pristine 7-AGNR [5]. Additionally the ribbons appear aligned in arrays in contrast with the disperse arrangement of pristine 7-AGNR [5]. This points towards the presence of nitrile groups in the ribbons, which drive the clustering of the GNRs via Van der Waals forces. The electric dipoles created by the nitrile groups (see next section) in the edges of neighboring ribbons can also contribute to this attractive inter-ribbon interaction with the appropriate relative orientation (Figure 4.2b).

However, the identification of the CN-functionalized sites in the STM images is difficult. To overcome this limitation we used a CO-functionalized tip [19, 30]. Figure 4.3b shows a dI/dV image of a section of a ribbon (indicated in Figure 4.3a) obtained with a CO-functionalized tip, resolving clearly its graphenoid backbone structure and additional features at the edges. The high resolution image allows us to characterize with high precision the edges of the ribbon and their precise functionalization. CN groups (marked with red arrows in Figure 4.3b) appear as linear features at the edges

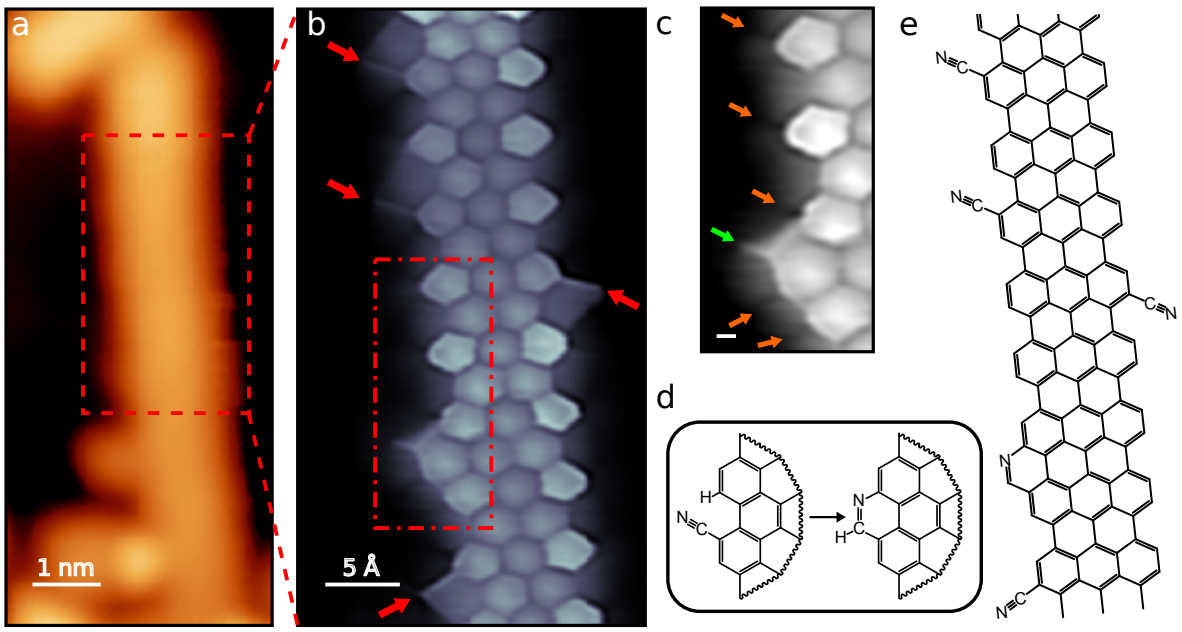

Figure 4.3: (a) Small-scale image of CN-7-AGNR acquired with a metallic tip (V_s=1 V, I_t=50 pA). The ribbon edges look almost featureless. (b) Constant height dI/dV map with a CO-functionalized tip of the dashed region in panel *a*. CN groups (red arrows) appear as linear bright protusions (Z_{off}=40 pm V_s=5 mV, OFC: V_s=5 mV I_t=120 pA, V_{rms}=10 mV f=699 Hz). (c) Zoomed in image of the dot-dashed region in panel *b* highlighting the additional pyridine ring. Orange arrows point the typical dark contrast around carbon atoms saturated with hydrogen. Green arrow points the bright contrast of the edge nitrogen atom. Scale bar corresponds to 1 Å.(d) Reaction scheme of the nitrile cycloisomerization into pyridine rings. (e) Chemical structure of the ribbon in panel *b*.

pointing along distinctive directions . We attribute the shadow on the CN groups to the potential landscape between CN group and the close-by H in the same bay region, to which the CO tip is sensitive [31, 110].

The high resolution dI/dV images also highlight unexpected chemical processes occurring during the on-surface GNR synthesis. First, we found that a large fraction of the CN groups (about 50%) are missing from the edges, probably lost during the GNR formation steps by σ-bond cleavage. Second, we observed the occasional appearance of additional rings at the edges of the 7-AGNR backbone, with a similar contrast as other six-member carbon rings (Figure 4.3c). Moreover, these new rings present a characteristic shape at the outermost edge atoms. We propose that these new rings are pyridine rings produced through the on-surface nitrile cycloisomerization of CN groups located on GNR bay regions (Figure 4.3d). This on-surface cyclization, to date unreported to the best of our knowledge, is related with the copper-catalyzed synthesis of phenanthridine derivatives from biaryl-2-carbonitriles and Grignard reagents by solution chemistry [111]. The resulting product can be corroborated by the high resolution dI/dV images, where the new H on the pyridine ring appears as a darker shadow, exactly as other aromatic hydrogen atoms nearby (orange arrows in Figure 4.3c). In contrast, a bright line in the images points to the position of the pyridinyl nitrogen atom of the heterocycle (green arrow in Figure 4.3c).

4.2 *n*-like doping induced by CN groups

We performed STS measurements to investigate the impact of the CN edge functionalization on the electronic structure of the 7-AGNR (Figure 4.4a). Figure 4.4b shows a high resolution image of a GNR section, showing two regions with different density of remaining CN groups (marked with red arrows). One of the regions maintains the CNs only in one of the sides (labeled as sCN-7AGNR), while the other have intact all CNs at the expected sites (2CN-7AGNR). The dI/dV spectra in these regions show two steps at 1.4 (1.2) V and -1.0 (-1.1) V for the sCN (2CN) segments. In analogy to the case of pristine GNR, these steps are attributed to the onset of the second conduction band (CB+1) and of the valence band (VB), respectively [44, 46] (see also Figure 4.5f). Comparing these spectra with that of a pristine GNR segment (included in Figure 4.4a) we prove that the CN functionalization produces a rigid downshift of the frontier bands, which amounts to ∼0.3 eV in sCN sections and ∼0.4 eV in 2CN regions. This behavior indicates that CN groups behave as n-dopants, as found for other nitrogen doped GNRs [6, 102]. The spectra also indicate that the density of CN groups affects the doping strength and, consequently, the bands' downshift. This is pictured in (constant heigth) dI/dV maps measured at 1.2 V (Figure 4.4c), which show a significantly larger dI/dV signal in the cyano-richer regions (the 2CN segments) due to the larger downshift of the CB+1 band.

In addition to the doping of the GNR, the CN moieties lead to a sizable accumulation of density of states in their proximity. dI/dV maps at -1.8 V (Figure 4.4d), a bias value well below the VB onset, find an increased conductance signal appearing mostly over the CN groups. This might suggest the existence of an impurity state similar to those observed in previous works [112] for amine and single nitrogen edge

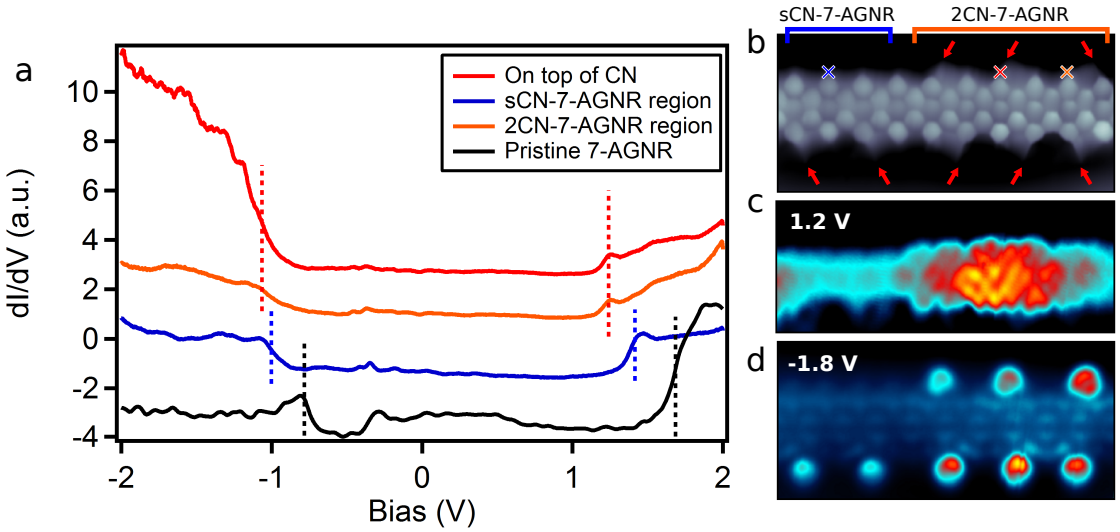

Figure 4.4: (a) Differential conductance (dI/dV) spectra taken at different sites of the ribbon in panel *b*. Red spectrum taken on top of a CN group. Orange spectrum taken between CN groups in the cyano rich regions (2CN-7-AGNR). Blue spectrum taken on the ribbon region with CN groups only on one edge (sCN-7-AGNR). A pristine 7-AGNR spectrum is shown in black for comparison. Dashed lines indicate the CB+1 and VB onsets for the different spectra. Onsets in sCN-7-AGNR regions are downshifted 0.28 eV respect to the pristine 7-AGNR. Onsets on the 2CN-7-AGNR region are downshifted an additional ∼0.18 eV for the CB+1 and ∼80 meV for the VB (open-feedback parameters CN-7-AGNR spectra: V_s=1 V, I_t=400 pA, V_{rms}=14 mV f=699 Hz, open-feedback parameters pristine 7-AGNR spectrum: V_s=0.5 V, I_t=75 pA, V_{rms}=12 mV f=700 Hz). (b) Constant height dI/dV image with a CO-functionalized tip. Red arrows mark the positions of the CN groups. Colored crosses mark the position where the spectra in panel *a* were taken. sCN-7-AGNR and 2CN-7-AGNR regions are highlighted in blue and orange respectively. (Z_{off}=40 pm, V_s=5 mV). (c) Constant height dI/dV map of the ribbon in panel *b* taken at V_s=1.2 V. The CB+1 onset is further downshifted in CN rich regions (Z_{off}=-90 pm). (d) Constant height dI/dV map of the ribbon in panel *b* taken at V_s=-1.8 V. The map shows the large contribution of the CN groups to the states at this energy (Z_{off}=-140 pm). OFC for CO dI/dV maps: V_s=5 mV I_t=110 pA, (b) V_{rms}=12 mV; (c,d) V_{rms}=20 mV, f=699 Hz.)

substitution. However, the calculations presented below seem to suggest that this signal should come from a rather flat band of the ribbon that strongly hybridizes with the CN group. Furthermore, dI/dV point spectra over the CN groups (red spectrum in Figure 4.4a), reproduce the larger occupied DOS at CN sites, but appear as a broad background, rather than a well-defined resonance.

The spectra also indicate a slight reduction of the bandgap upon addition of CN groups. Comparing to pristine 7-AGNR, the bandgap in sCN-7-AGNR and 2CN-7AGNR sections is ∼50 meV and ∼100 meV smaller, respectively. The bandgap closing is consistent with the increase of effective width of the π-network, since the CN groups extend the conjugation of the 7-AGNR backbone.

To complement the experimental picture on the impact of CN functionalization

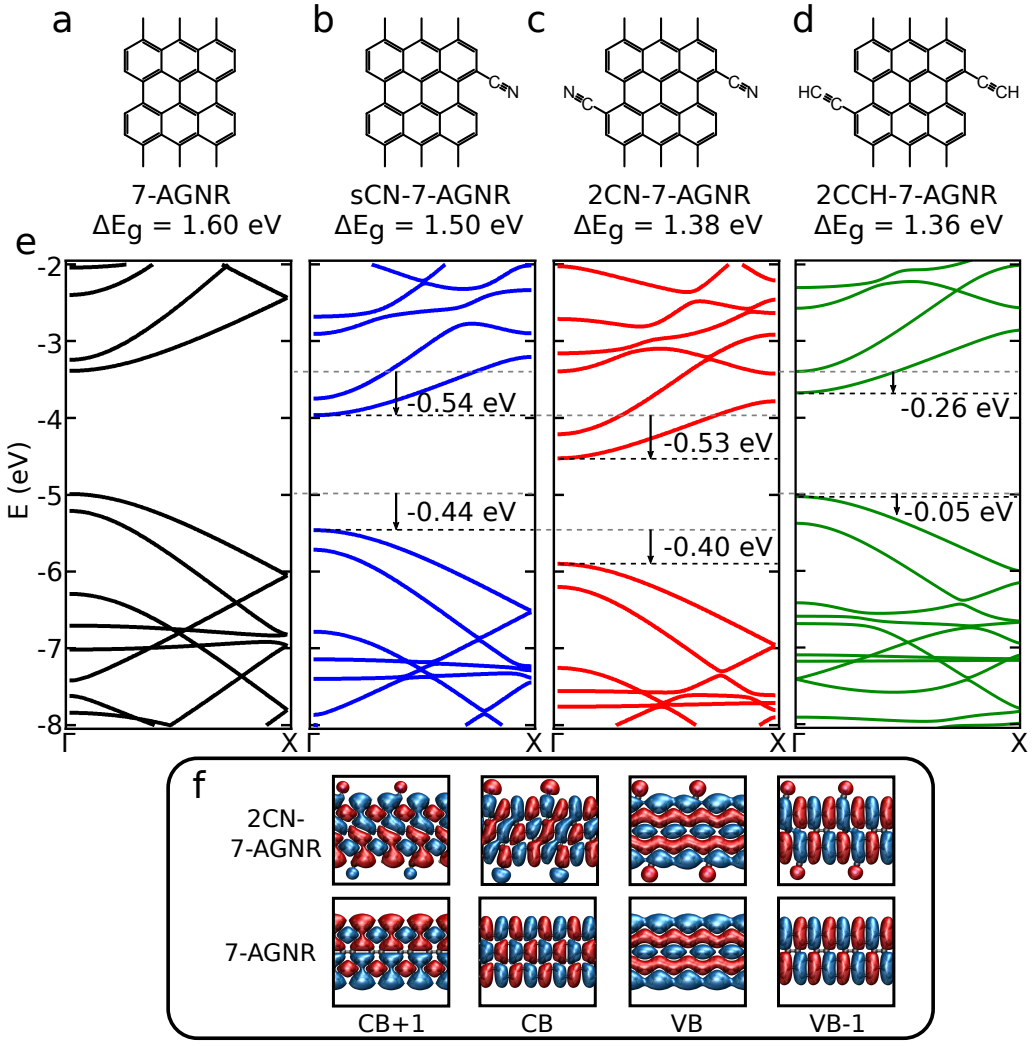

Figure 4.5: (a-d) Periodic unit cell for the calculated freestanding ribbons: pristine 7-AGNR, sCN-7-AGNR and 2CN-7-AGNR and an acetylene functionalized 7-AGNR, i.e. 2CCH-7-AGNR. (e) Band structure for each different ribbon. The CB and VB show a downshift and a slight closing of the gap unpon adding CN groups. The CB+1 downshifts 0.5 eV and 0.46 eV more in sCN-7-AGNRs and 2CN-7-AGNRs, respectively. For 2CCH-7-AGNR (green), the CB downshifts 0.26 respect to the pristine case, while the VB only shifts -0.05 eV. The energies of the band structures are referred to the vacuum energy. (f) Real part of the wavefunctions of pristine 7-AGNR and 2CN-7-AGNR at the Γ point. The bands symmetry is not changed by the presence of CN groups. Therefore, the relative intensities of the STM/STS features of the different bands should not be altered as compared to the pristine case.

we performed DFT calculations of freestanding 7-AGNRs with periodically arranged CN functional groups in one (Figure 4.5b, sCN-7AGNR) or both sides (Figure 4.5c, 2CN-7AGNR). Figure 4.5e compares the calculated band structure of pristine, sCN, and 2CN nanoribbons. The calculations reproduce both the additive downshift of the bands and the bandgap reduction upon addition of CN groups. The results show that for each CN added to the pristine ribbon, the VB downshifts ∼0.4 eV, while the CB

and CB+1 move ∼0.5 eV. In our experiments, the observed band shifts are however smaller, between 0.2 eV and 0.3 eV. We attribute this to the interaction effects of the ribbon with the metal surface, such as the screening provided by the substrate. Given the calculated band downshifts, the band gap of the functionalized ribbons closes 100 meV for a sCN-7-AGNR and 220 meV for a 2CN-7-AGNR which agrees qualitatively with the experimental results. The origin of the bandgap closing is the extension of the conjugated π-network, due to the addition of the CN moieties. To prove this, we calculated the band structure of a similar 7-AGNR substituting the CN groups by acetylene groups, which extend the conjugate system in a similar way (2CCH-7-AGNR, Figure 4.5d and e in green). Our results show a similar bandgap (ΔE_g=1.36 eV) to that of 2CN-7-AGNR, although without a downshift of the VB in this case, confirming our previous hypothesis.

The rigid downshift of the bands is an observed trend after the incorporation of electronegative species onto GNRs [6, 102]. However, the band's downshifts induced by CN groups are larger than those induced by nitrogen heterocycles. Even though the ratio between carbon and nitrogen per ribbon cell is smaller in 2CN-7-AGNR, our DFT results find a 0.5 eV downshift per CN group compared to the 0.13 eV per edge nitrogen in chevron GNRs [6]. Thus, our results indicate that cyano moieties behave as more efficient *n*-dopants than nitrogen heterocycles.

To unravel the mechanism behind the band downshift induced by the CN groups we next focus on the details of interaction between these functional groups and the ribbon. Figure 4.6a shows the 2CN-7-AGNR bands, with the amount of N-contribution represented by the thickness of a blue shadow. The plot shows that the the N character is widespread in the whole band structure. The origin of such strong mixing is the resonant character of the conjugation between CN and 7-AGNR mesh (Figure 4.6c). The DOS is enhanced particularly at ∼-7.7 eV due to nearly flat bands (top red arrow, Figure 4.6b) with strong p character (Figure 4.6d), presumably being responsible to the dI/dV enhancement found in the spectra of Figure 4.4a and in the dI/dV map of Figure 4.4d. Moreover, states with strong N character are found at lower energy, deep inside the filled states of the ribbon (∼-9 eV, Figure 4.6b). These states, not reached in our STS spectra, have both s and p character (Figure 4.6d), in agreement with the nitrogen *sp* orbital hosting the lone pair. Since the localized lone pairs do not participate in the conjugation of the GNR π-system, these states are regarded as the impurity levels induced by the CN groups.

Most importantly, the strong electron withdrawing character of CN induces a charge redistribution over the whole ribbon (Figure 4.6e and f) and results in sizeable dipoles at the CN sites. We calculate these dipoles using the following expression:

$$\boldsymbol{\mu} = \int_{\text{half cell}} \left(\rho_{tot}(\mathbf{r}) - \sum_{I=1}^{N_{atoms}} \rho_I(\mathbf{r}) \right) \mathbf{r} d\mathbf{r} \tag{4.1}$$

where, ρ_{tot} is the total valence charge density, ρ_I is the valence charge density of each individual free atom and r is the distance from the growth axis. The integral is performed over half of the ribbon (respect to the ribbon's growth axis). In the pristine ribbon, each edge accumulates a dipole of 2.4D pointing from the ribbon growth axis to the edge, mainly as a consequence of the charge redistribution between C-H end

groups (that is 0.6D per C-H). In the case of the 2CN-7-AGNR, each edge accumulates a dipole of -1.1D (pointing to the center of the ribbon). The three C-H end groups hold similar charge population than in the pristine case. However, the CN group generates a dipole in the opposite direction. Thus we estimate that the dipole induced only by the CN is of $-1.1 - 0.6 \times 3 \sim -2.9$D. We note this value is in reasonable agreement to the calculated dipoles for a HCN $\mu = -2.86$ D molecule (see also [113]).

The CN localized dipoles modify the electrostatic background of the ribbon. Figure 4.7a shows the electrostatic potential at the plane of the ribbon (z=0) and, averaged over the periodic direction (x). We observe the effect of the dipoles caused by the CN

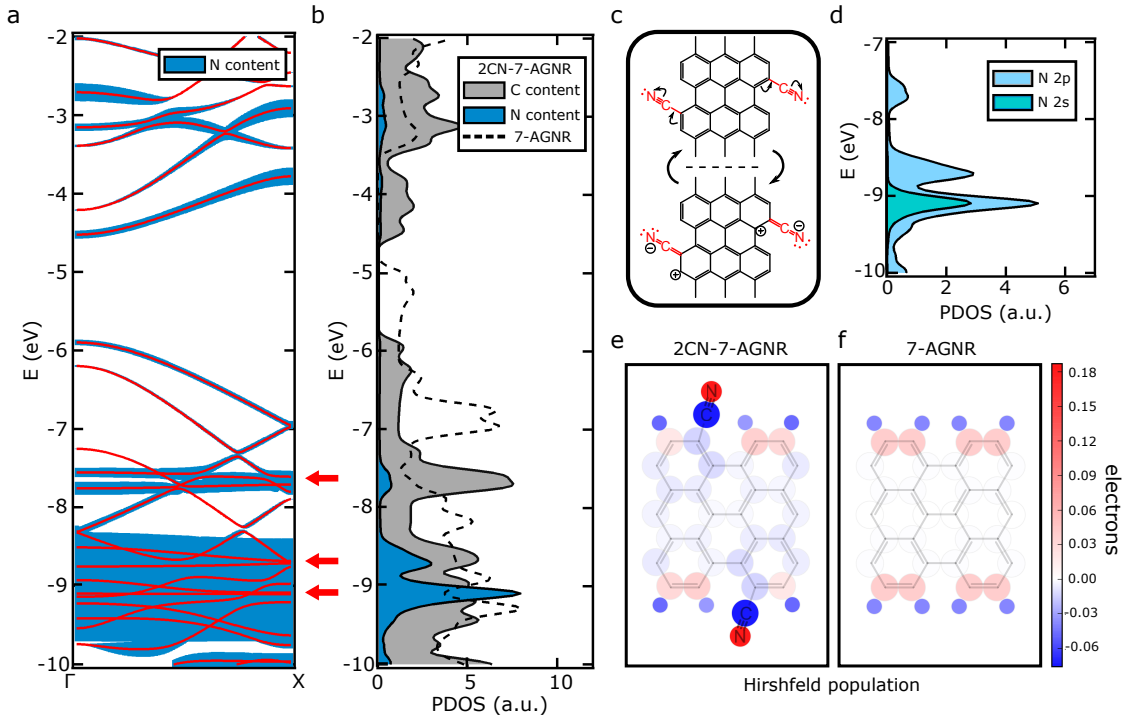

Figure 4.6: (a) Band structure of a 2CN-7-AGNR showing the nitrogen content of the bands. The CB and the VB show a clear hybridization with the CN groups. Flat bands with strong Nitrogen weight are observed close to -7.7 eV and -9 eV (red arrows). The zero energy of the band structures is referred to the vacuum energy. (b) DOS projected on C and N atoms of a 2CN-7-AGNR (grey, blue) and a pristine 7-AGNR (dashed line). The CB and VB show smaller N contributions compared with the states associated with the flat bands at $\sim$-7.7 eV and $\sim$-9 eV. (c) Resonant structures for a 2CN-7-AGNR unit cell. The CN groups are in conjugation with the AGNR structure. Thus, the π-network is slightly extended. In contrast, the Nitrogen lone pair is localized and does not participate in the conjugation. (d) Orbital contributions to the nitrogen PDOS of the strongest nitrogen peaks in panel *b*. The peak at $\sim$-7.7 eV shows only p component, whereas the peak at $\sim$-9.2 eV has a strong s component too. (e) Hirshfeld population plot of a 2CN-7-AGNR representing the charge redistribution in the ribbons. The nitrogen atoms accumulate $0.18e$, while the carbon network is slightly depleted of charge. (f) Same as in panel *e* but for a pristine 7-AGNR. In this case the edge carbon atoms accept a small amount of charge from the hidrogen terminations.

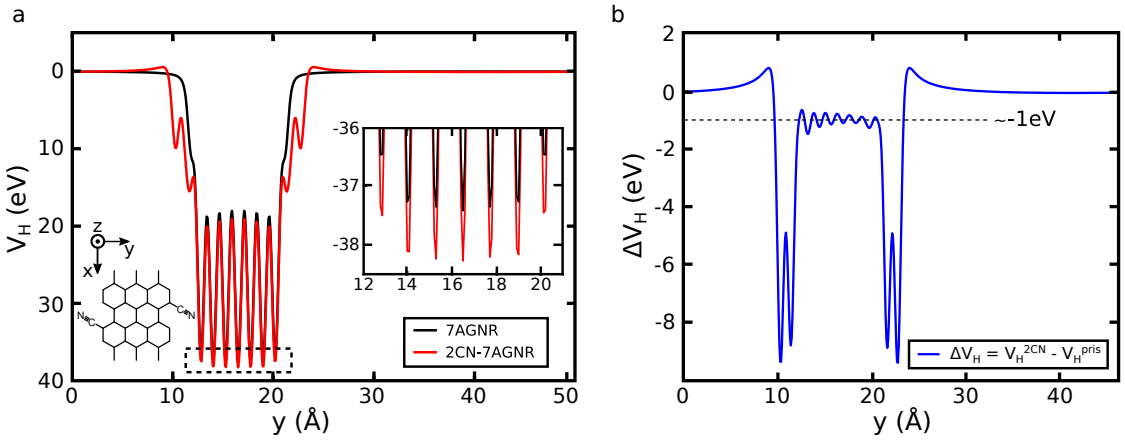

Figure 4.7: (a) Electrostatic potential (V_H) of a pristine 7-AGNR (black) and a 2CN-7-AGNR (red) at the plane of the ribbon (z=0) and averaged over the periodic direction (x). Small positive shifts can be observed close to the edges of the ribbon, as a consequence of the CN dipoles. Inset zooms at the central region of the ribbon (dashed rectangle), where an offset of -1 eV can be seen between both cases. (b) Difference in electrostatic potential ($\Delta V_H = V_H^{2CN} - V_H^{prist}$) between both ribbons, highlighting the presence of a 1 eV downshift at the central part of the ribbon. The oscillations observed are mostly caused by small differences in atomic positions between both ribbons.

groups as two $V_H > 0$ shifts at the edges of the ribbon. As seen in the inset of Figure 4.7a, the electrostatic potential at the center of 2CN-7-AGNR backbone presents a downshift (~ -1 eV) compared to the pristine case, and thus, 2CN-7-AGNRs are more electronegative. Figure 4.7b shows the difference in electrostatic potential between 2CN-7-AGNR and pristine 7-AGNR ($\Delta V_H = V_H^{2CN} - V_H^{prist}$), highlighting the -1 eV electrostatic background at the backbone of the functionalized ribbon. We note as well that the shift in electrostatic background agrees nicely with the one calculated for the bands (-1.07 eV for the CB, -0.84 eV for the VB). Thus, our results suggest that the bands downshift is a consequence of the charge redistribution induced by the CN groups.

4.3 Conclusions

In summary, we have shown the growth of cyano substituted 7-AGNR and studied the impact of nitrile functional groups on the electronic structure of the ribbons. The CN groups increase the reactivity of the 7-AGNRs as inferred from the bunching of the ribbons into aligned clusters and the overall shorter ribbon lengths. STM imaging with CO-functionalized tips resolves with high precision the intramolecular structure of the ribbons and finds a significant loss of CN groups, close to 50%. Moreover, the high resolution images unveil the on-surface nitrile cycloisomerization into pyridine rings, which has not been previously reported.

By combining STS and DFT calculations we have shown that the addition of CN groups conjugated to the GNR structure reduces its bandgap, since the π-network of the GNR is extended. Furthermore, we have demonstrated that CN groups behave as

n-dopants. The CN groups downshift the bands ∼0.5 eV per CN added (∼0.3 eV in the experiments), which is significantly more than the doping observed in substitutional nitrogen edge atoms. The downshift of the bands stems from the strong electron withdrawing character of nitrile groups, which induce dipoles at the CN sites. The charge redistribution causes a downshift of the electrostatic potential in the GNR backbone, resulting in an increased ribbon electronegativity. In conclusion, our work shows the potential of using functional groups as tools to modify the physicochemical properties of GNRs, albeit further work concerning the stability of said groups is needed.

Chapter 5

Role of substrate interactions in boron substituted 7-AGNR

On-surface synthesized GNRs have been mainly studied on top of rather weakly interacting substrates, such as Au(111), which simplify both its study and comparison with theoretical predictions. However, the process of doping through chemical modification may induce additional interactions between a more reactive ribbon and its supporting substrate. The impact of this interactions might significantly change the properties and potential applications of the ribbon, specially if transferred onto non-noble substrates. In this chapter we show how the larger ribbon-substrate interaction of boron substituted 7-AGNRs induces a hybridization between surface and ribbon bands.

Boron is a typical dopant in silicon based semiconductors. As it has one valence electron less ([He]$2s^2 2p^1$) than the silicon host ([Ne]$3s^2 3p^2$), the boron is missing one electron to form the sp^3 hybrid orbitals required to substitute it silicon in the lattice and, therefore, acts as a p-dopant [114]. In a carbon ([He]$2s^2 p^2$) sp^2 network boron contributes similarly, with three electrons creating sigma bonds with the surrounding carbons, leaving an empty p_z orbital. Therefore, boron substitutes could be used as p-dopants in GNRs as already reported in previous works [105].

Figure 5.1 depicts the molecular precursor (2B-DBBA) used to grow boron doped 7-AGNRs. The precursor is very similar to DBBA but includes a 9,10-dihydro-9,10-diboraanthracene moiety in its center [104, 105]. In these positions, we expect the empty p_z orbitals of boron to be part of the π-system of the ribbon.

As seen in Figure 5.1, the reaction leads to the formation of 5% boron doped 7-AGNR (2B-7-AGNR). In this conditions, the impurity levels of dopants typically

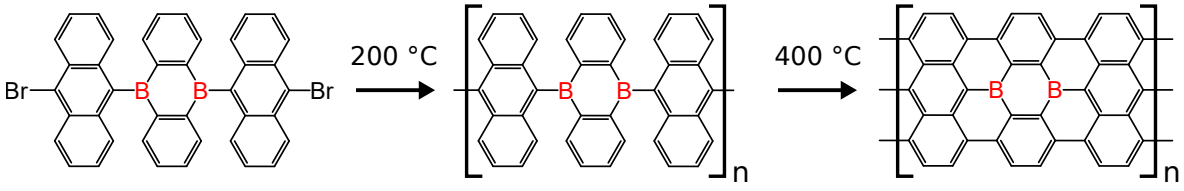

Figure 5.1: Chemical structure and reaction pathway of 9,10-bis(10-bromoanthracen-9-yl)-9,10-dihydro-9,10-diboraanthracene (2B-DBBA) on Au(111) [104, 105]. The resulting ribbons are 7-AGNR with a 5% Boron content.

hybridize onto acceptor (or donor) bands [14]. Here we report the growth of 2B-7-AGNRs on Au(111) and provide a thorough description of their electronic structure. We study the frontier bands of the ribbons by means of ARPES and STS, providing the valence band effective mass and an experimental bandgap for 2B-7-AGNRs. By combining STM and DFT calculations we find that the structure of 2B-7-AGNR is corrugated and that the boron induced acceptor band strongly hybridizes with the substrate. These effects stem from the higher interaction between the ribbons and the underlying substrate.

5.1 Growth of 2B-7-AGNR

2B-DBBA molecules were sublimated from a Knudsen cell held at 290 °C onto a Au(111) kept close to room temperature. After deposition the sample was subsequently annealed to 200 °C and 400 °C to trigger the polymerization and cyclodehydrogenation steps, respectively [5]. Figure 5.2a shows a STM image of the resulting 2B-7AGNR covered surface. The length of the ribbons is quite similar to pristine 7-AGNRs. The ribbons tend to align following the herringbone reconstruction of the Au(111) substrate (Figure 5.2b). Moreover, on certain occasions, the surface reconstruction is distorted by the presence of the 2B-7-7AGNR [104]. The main characteristic feature of the 2B-7-AGNR is is a height modulation along the backbone in the STM images (Figure 5.2c).

We resolve the intramolecular structure of these ribbons acquiring constant height images using CO-functionalized tips (Figure 5.7a). In contrast with pristine 7-AGNRs images (chapter 3.1), the inner carbon rings are brighter than those at the edges. Moreover, the ribbon edges of the carbon segments appear brighter than those of the

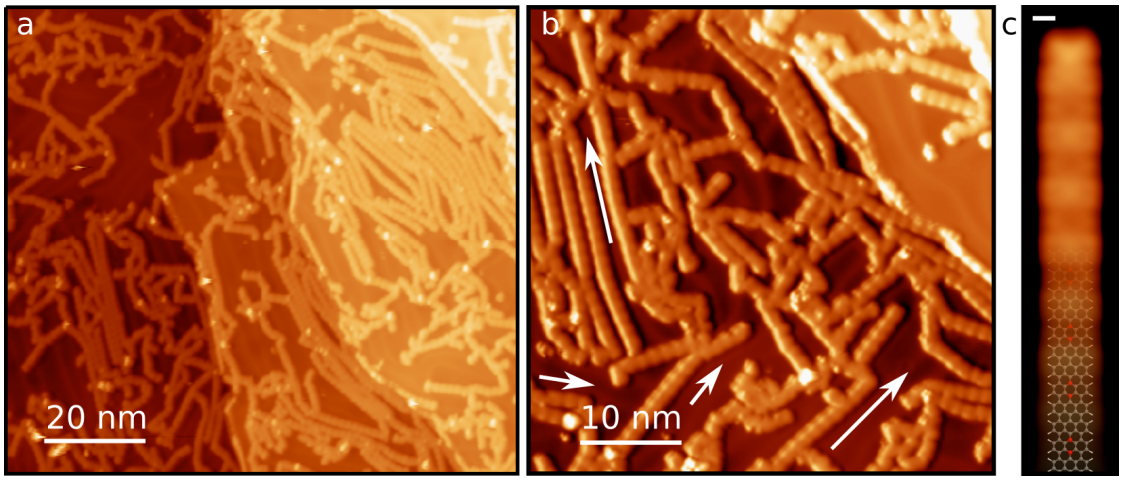

Figure 5.2: (a) Overview of the 2B-7-AGNR on Au(111) (V_s=1 V I_t=170 pA). (b) Small scale overview of 2B-7-AGNR. The ribbons preferentially align with the herringbone reconstruction. White vectors mark the directions parallel to the gold reconstruction fcc sites in different positions (V_s=1 V I_t=100 pA). (c) Small scale image of a 2B-7-AGNR with its molecular structure overlaid. The lower topography regions correspond to the borylated regions (V_s=-150 mV I_t=410 pA).

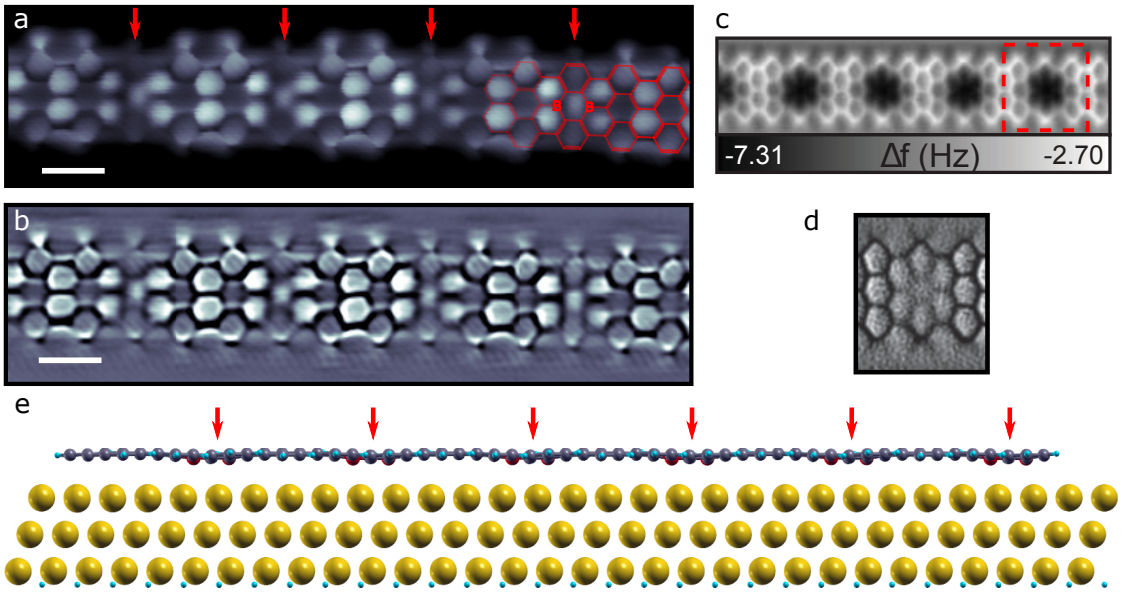

Figure 5.3: (a) Constant height image of a 2B-7-AGNR with a CO-functionalized tip. Overlaid in red is the chemical structure of the ribbon. Red arrows highlight the borylated segments, (V_s=3.5 mV Z_{off}= -0.6 Å; OFC: V_s= 200 mV I_t=100 pA). (b) Laplacian filtered image of panel *a*. (c) Frequency shift map with a CO functionalized tip, extracted from [104]. Boron sites appear as dark depressions compared to the bright carbon backbone. (d) Laplacian filtered image of a boron segment such as the one highlighted in red in panel *c*, extracted from [104].(d) DFT relaxed cell of a 2B-7-AGNR on top of a gold slab. The boron pairs, pointed with red arrows, approach ∼30 pm towards the surface. Hydrogen is represented in blue for clarity. The presence of hydrogen in the bottom surface of the gold is explained in the following section.

boron segments. This points towards a modulation of the Local Density of States close to the E_F, which complicates the assessment of the actual corrugation of the ribbon. Previous non contact AFM experiments using CO-functionalized tips reported dark depressions at the boron segments (Figure 5.7c,d [104]), which, to some extend, could be ascribed to the density of charge near the electron-deficient borons. However, our DFT calculations of a 2B-7-AGNR on top of a Au(111) slab (Figure 5.7d) confirm the actual corrugation of the ribbon, where boron atoms lay 30 pm closer to the surface. This buckled configuration suggests a stronger interaction between 2B-7-AGNRs and the substrate compared to pristine 7-AGNRs.

5.2 Electronic structure and substrate-ribbon hybridization

We performed STS measurements on 2B-7-AGNR to determine the effect of boron substitution in the AGNR electronic structure. Figure 5.4b shows a stack plot of dI/dV spectra (spectral map) taken across the borylated subunits of the 2B-7-AGNR. The most striking difference with pristine 7-AGNRs is the apppearance of a broad

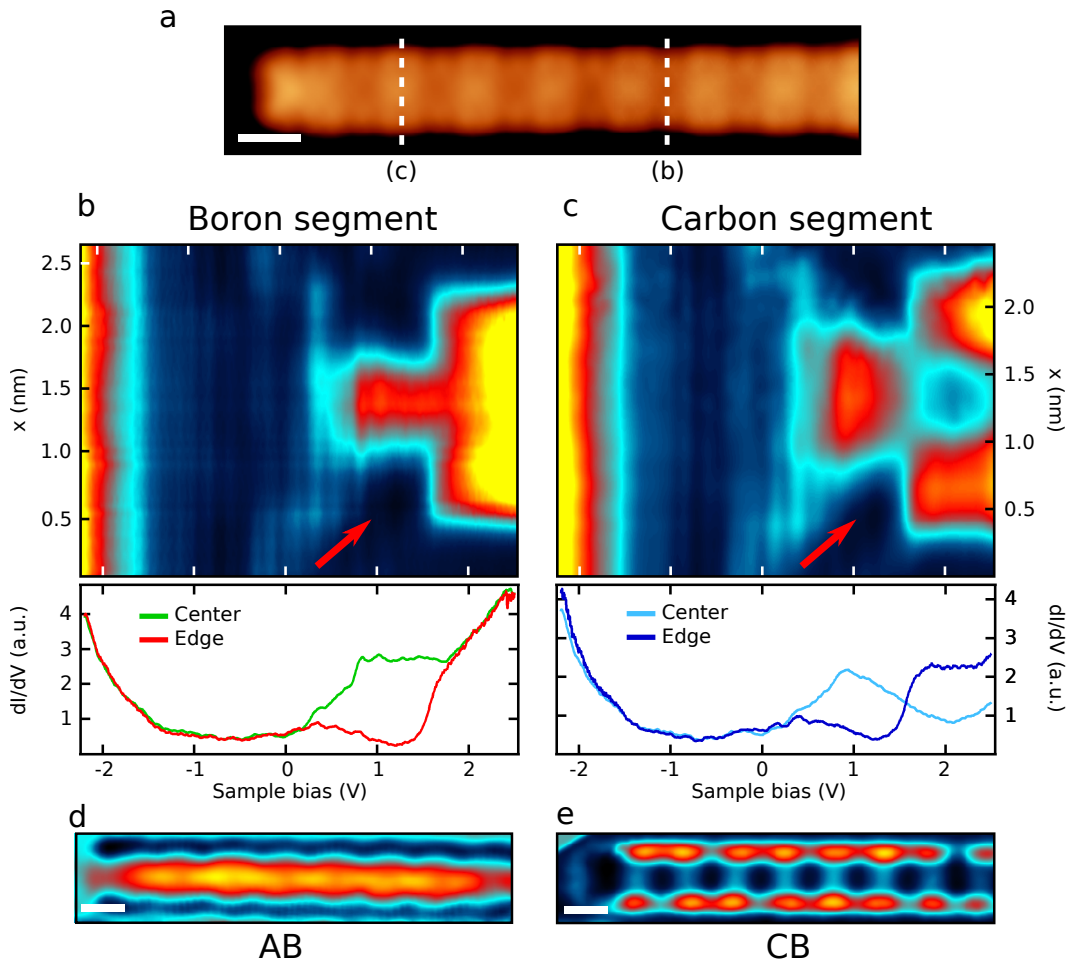

Figure 5.4: (a) STM topography of a 2B-7-AGNR. White dashed lines show the positions where the spectral maps were acquired (V_s=-150 mV I_t=410 pA). (b) dI/dV spectral map taken across a boron segment of a 2B-7-AGNR. Two cuts, at the edge (red) and at the center (green) of the ribbon are shown. The AB is clearly localized around the center of the ribbon, while the CB presents higher intensity at the edges. The AB and the CB overlap at the center of the ribbon. The Au(111) SS is visible outside the ribbon at -500mV and upshifts beneath it (following the red arrow). (c) Same as in *b*, but across a carbon segment. (d) dI/dV map of *a* at V_s=1.05 V, where AB peaks. The DOS is clearly located along the backbone of the ribbon.(e) Same as d but at V_s=1.65 V, which is the onset of the CB. The contrast is located around the edges of the ribbon and over the boron segments (OFC for *b* and *c*: V_s=-1.1 V, I_t=0.4 nA, V_{rms}=18 mV, f=751.9 Hz; FC for *d* and *e*: I_t=0.4 nA, V_{rms}=18 mV, f=751.9 Hz).

increase of conductance in the center of the ribbon, from 0.3 V and peaking around 1 V. We observed this broad resonance both in the borylated and carbon subunits of the ribbon (Figure 5.4c). A dI/dV map acquired at the energy of this new feature (Figure 5.4d) shows that the new state extends along the 2B-7AGNR and has higher intensity at the center of the ribbon. This suggests the presence of a new band as a consequence of the boron substitution. Previous works [105] associated these feature to an acceptor band (AB), due to its extended character and because it lays above E_F.

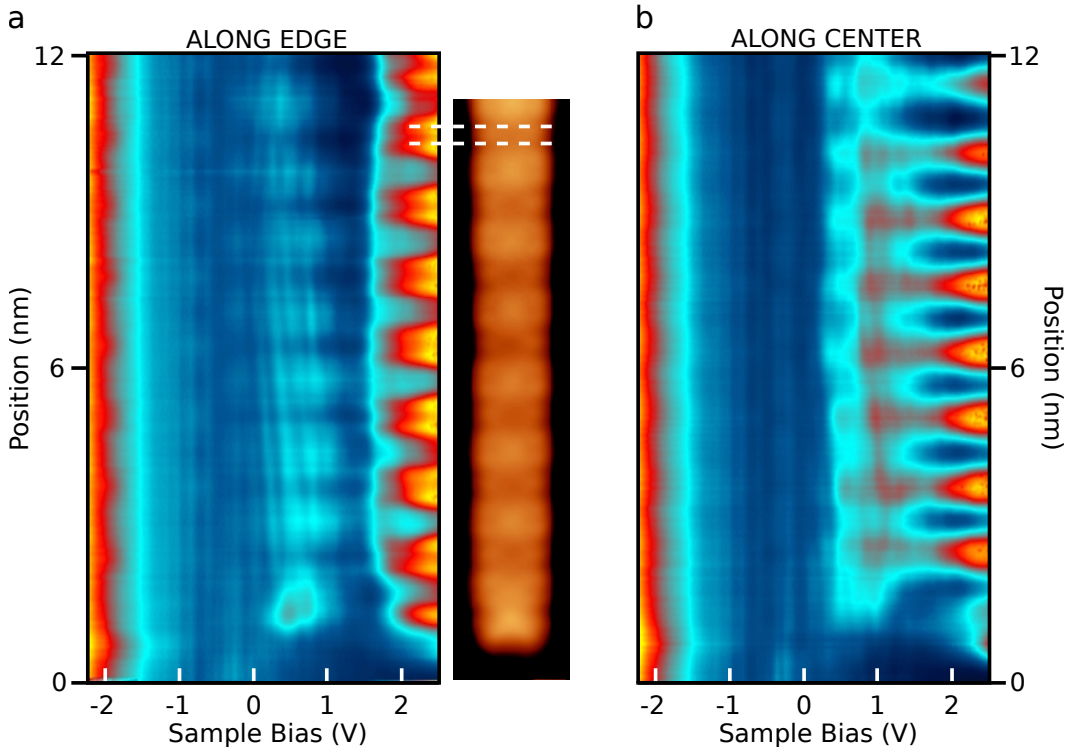

Figure 5.5: (a) dI/dV spectral map taken along the edge of a 2B-7-AGNR. The signal above 2 V allows to locate individually the boron atom contributions (white dashed lines). Ribbon displayed for reference. (b) dI/dV spectral map taken along the center of a 2B-7-AGNR. The acceptor band around 1 V is stronger than in *a*. Also the signal above 2 V shows the boron contributions to the CB and CB+1. (OFC for *a* and *b*: V_s=-1.1 V, I_t=410 pA, V_{rms}=18 mV, f=752 Hz;)

Additionally, the spectral maps show an onset of conductance at 1.6 V. This onset has a stronger weight on the edges of the ribbon and decay in intensity considerably towards the center of the carbon sites. Both the energy position and the spacial distribution of the state are reminiscent to the CB+1 of pristine 7-AGNR (see chapter 3.2 and [45]). In contrast, this band (from now on called CB) is also modified by the boron pairs. As observed over the boron segments (Figure 5.4b), the intensity of the CB does not decay towards the center of the ribbon. Again, this can be observed in the dI/dV maps taken at the onset of the CB (Figure 5.4e), showing stripes of higher contrast on the borylated regions.

Finally, we observe an evolution of the features attributed to the Au(111) surface state (SS) as we approach the ribbon (red arrows in Figures 5.4b and c). The SS signatures seem to merge with the AB, specially beneath the boron segments. This effect points again towards a larger interaction between the ribbon and the substrate, thus compatible with the large linewidth of the AB.

The spectral maps acquired (Figure 5.5) along the edge (a) and center (b) of the ribbon provide a summarized picture of all the spectral features explained before. The acceptor band is more visible along the center of the ribbon than along the edge. The CB appears heavily modulated by the boron pairs, as observed from the increases of

conductance at ∼2 V. Finally, the fringes observed at the energies of the AB (∼0.3 V to ∼1V), all along the ribbon, could origin from the merging of the spectral features of the Au(111) SS with the AB.

The VB onset of 2B-7-AGNR, to date not reported, is not observed in the dI/dV spectral maps of Figures 5.4 and 5.5. To gain insight on this band, we performed ARPES measurements on 2B-7-AGNRs and pristine 7-AGNRs. The ribbons were grown on a vicinal Au(322) substrate. On this surface, the parallel array of step edges promotes the nanoribbon alignment along the terrace edge direction (i.e. along the $[1\bar{1}0]$ direction). Figure 5.6a shows the ARPES spectra for clean Au(322) substrate, 2B-7-AGNR and 7-AGNR, detecting the signatures of a band in both borylated and pristine ribbons. Figure 5.6b, shows energy cuts at the maxima of each detected band. The onset of the pristine 7-AGNR and 2B-7-AGNR lays at -1.28 eV and -0.93 eV,

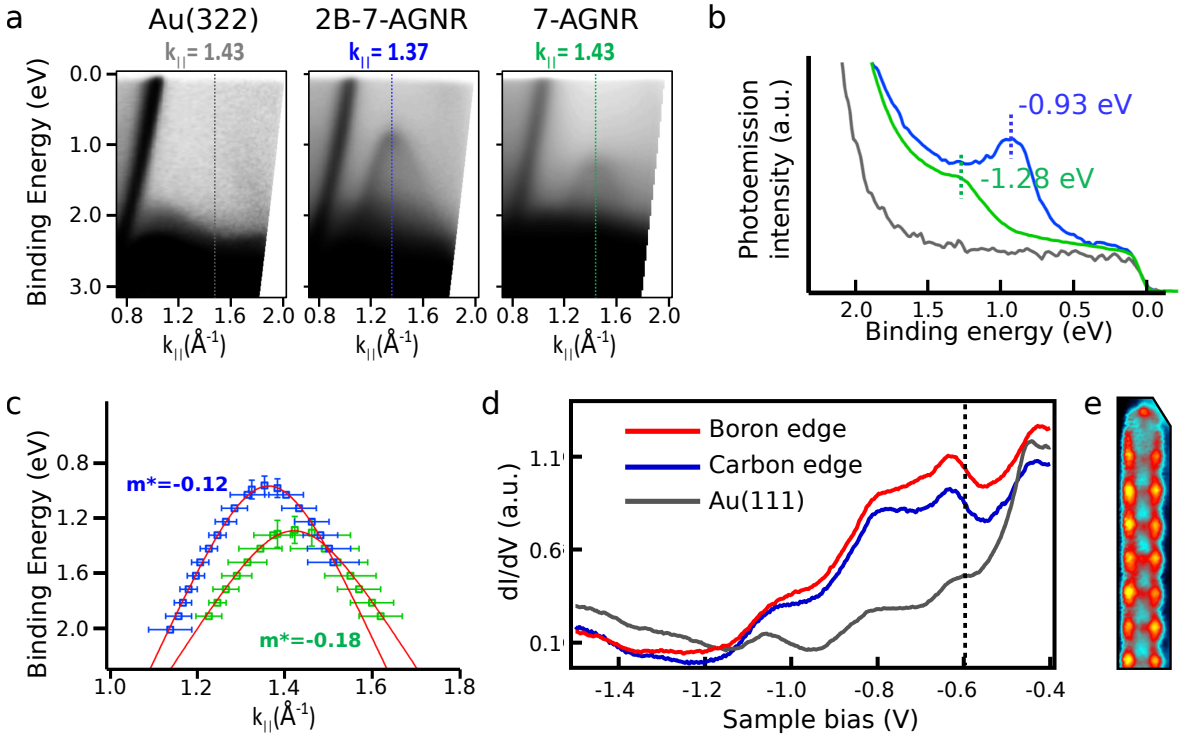

Figure 5.6: (a) ARPES measurements of the clean Au(322) substrate (left), the surface covered by 2B-7-AGNRs (center) and the surface covered by pristine 7-AGNRs (right). (b) ARPES spectra at the maxima of the VB for pristine 7-AGNR (green), 2B-7-AGNR (blue) and Au (322) (grey). (c) Fits of the experimental energy dispersions of the pristine 7-AGNR (green) and the 2B-7-AGNRs (blue). Red lines correspond to the parabolic ($E = E_0 + \hbar^2 k^2 / 2m^*$) fits for both data sets, that allow the extraction of the effective masses of both VBs. The smaller $k_{\|}$ in 2B-7-AGNR points towards a $4 \pm 2\%$ strained unit cel, compared to 7-AGNR. (d) Constant current dI/dV of the filled states of a 2B-7-AGNR. black dashed lines shows the energy onset of the VB. The onset is observed both at the edge of a carbon (blue) and borylated (red) segment (FC: I_t=0.5 nA,V_{rms}=12 mV, f=769 Hz). (e) dI/dV map of Figure 5.4a at the VB onset V_s=-0.55 V. The contrast is modulated along the length of the ribbon, showing stronger dI/dV signal at the boron segments. (I_t=0.4 nA,V_{rms}=18 mV, f=751.9 Hz).

respectively. Moreover, the parabolic fit of the ARPES spectra reveals (Figure 5.6c) that the effective mass of 2B-7-AGNR VB is $m^* = -0.12\,m_e$, slightly smaller than the pristine case. The photoemission results also show that the band onset of the borylated ribbons lies at a smaller wave-vector ($k_{\|}$) in the reciprocal space. This would correspond to a $4 \pm 2\,\%$ strain along their growth axis. However, the intramolecular resolved STM measurements do not report such strain on ribbons on top of Au(111) (merely a $0.5 \pm 0.6\,\%$) . A possible explanation for this inconsitency is the higher reactivity of Au(322) terraces which could act as anchoring points for the 2B-7-AGNR boron pairs.

The onset of the VB detected by ARPES on the 2B-7-AGNR/Au(332) system, can be used to track the VB onset on Au(111) if we take into account that the workfunction of the stepped substrate is lower than the flat (111) surface [115]. Using the pristine 7-AGNR VB onset as energy reference, i.e. -0.84 eV on Au(111), -1.28 eV on Au(322), the 2B-7-AGNR's VB on Au(111) should be found close to ∼-0.5 eV. In fact, constant current spectra find a dI/dV increase at -0.6 eV, which we associate to the VB onset, thus lying slightly below the Au(111) surface state onset at -0.5 eV (Figure 5.6d). Constant current dI/dV maps of the VB (Figure 5.6e) shows a modulated contrast at the edges and center of the band, their maxima coinciding with the borylated sections. The values from the VB and AB define an effective bandgap of ∼1.6 V (peak to peak), which is close to a 30% reduction respect to pristine 7-AGNRs.

We resolve the different bands' DOS shape by constant height dI/dV maps with CO functionalized tips. As explained in chapter 1.2, this allows to obtain a higher detail of the LDOS of the bands at the cost of convoluting the ribbon features with the π orbitals of the CO probe. Figure 5.7a shows the features of the VB. The carbon regions consist

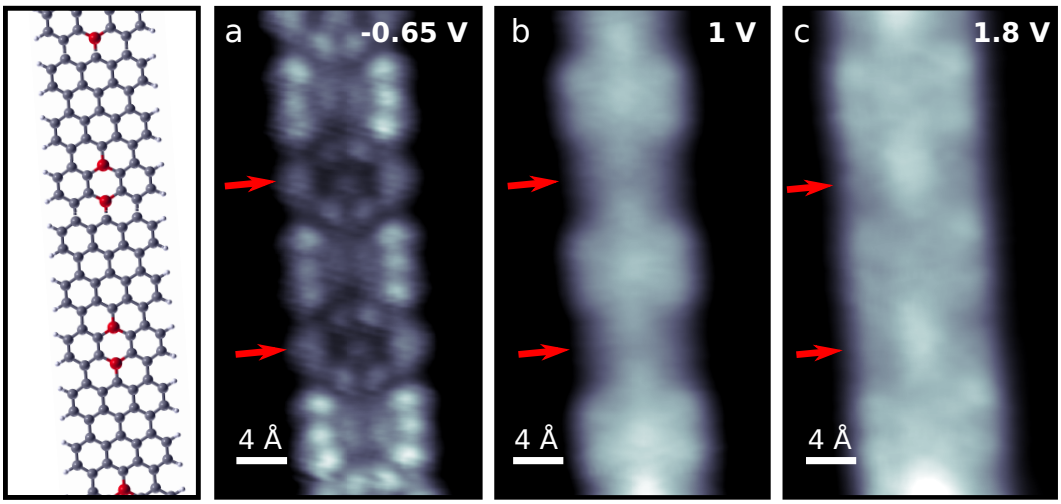

Figure 5.7: (a) Constant height dI/dV maps with a CO-functionalized tip of the different 2B-7-AGNR bands. Red arrows mark the position of the borylated regions. (a) VB displaying a characteristic nodal structure at its center consisting on two lobes in the carbon segments and five in the boron regions (Z_{off}=-1.8 Å). (b) AB showing a modulated width, thinner in the borylated segments (Z_{off}=-0.8 Å). (c) CB dsiplaying an increased conductance on top of the boron pairs (Z_{off}=-1.2 Å).(OFC: V_s= 20 mV, I_t= 100 pA, (a): V_{rms}=4 mV; (c,d): V_{rms}=14 mV, f=760 Hz).

on three lobes located at each edge, with a slight radial distribution, surrounding two lobes at the center of the ribbon. The boron regions appear as rhomboid shapes, two lobes at each side surrounding five lobes in the center. At 1 V (Figure 5.7b), the AB is characterized by a modulated edge intensity, with boron segments appearing weaker and thinner, and carbon segments appearing wider. The inner structure of the band is, on the contrary, rather featureless, with single faint maxima in the carbon segments and two maxima along the borylated segments. Finally, at the energies of the CB (Figure 5.7c), the maps show a constant width shape with increased intensities at the center of the borylated sites.

We now focus in the details of the interaction between the 2B-7-AGNR and the

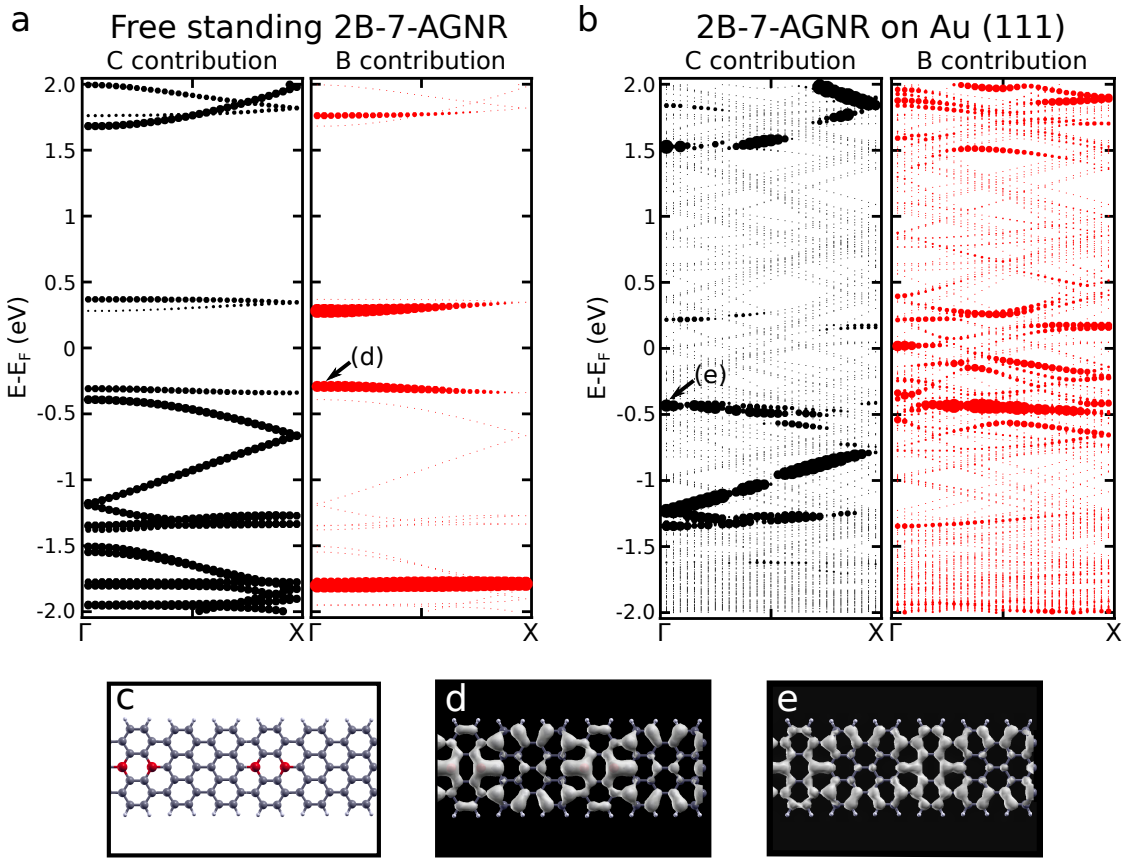

Figure 5.8: (a) Band structure of a freestanding 2B-7-AGNR (unit cell displayed in panel *c*), distinguishing the Carbon contribution (left, black) and the Boron $2p$ contribution (right, red). Thicker bands correspond to higher carbon or boron weight. Two clear boron heavy bands appear at ± 0.3 eV, CB_{th} and VB_{th} (Boron weights have been multiplied by a factor 5 (free-standing) and 10 (adsorbed) for clarity) (b) Same as in *a* but for a 2B-7-AGNR on top of a hydrogen passivated three layer gold slab. (c) 2B-7-AGNR unit cell used in both free standing and adsorbed calculations. (d) LDOS of the VB_{th}, highlighted in panel *a*, integrated from -0.35 to -0.25 eV. We note the similarities between this LDOS and the experimental dI/dV map of the VB in Figure 5.7a. (e) LDOS of the VB_{th} for the adsorbed ribbon, integrated from -0.5 to -0.35 eV. The LDOS shows very little changes from its free-standing counterpart.

underlying gold substrate. We performed DFT calculations of free standing 2B-7-AGNRs and 2B-7-AGNRs adsorbed on top of a three layer gold slab. The bottom of the Au slab is passivated with hydrogen atoms (Figure 5.3e) in order to quench one of the Au(111)'s Shockley surface states and thus provide a more refined model of the metal substrate [116]. Figure 5.8a shows the band structure of a freestanding 2B-7-AGNR, splitted in its carbon and boron contributions. The most characteristic feature is the pair of boron heavy bands at ± 0.3 eV (from now on called CB_{th} and VB_{th}). When adsorbed on top of the gold slab (Figure 5.8), the ribbon band structure close to E_F becomes more diffuse. While the band structure and LDOS of the VB_{th} (Figures 5.8d and e) suggest few changes of this band upon adsorption, the CB_{th} broadens considerably, extending between $\sim$0 to $\sim$0.5 eV, as a consequence of the hybridization between the substrate and the ribbon band. Thus our calculations support the presence of an empty band, strongly hybridized with the substrate, consistent with the observed behavior of the experimental AB. The difference in energy between the AB seen in the experiment and CB_{th} probably comes because DFT cannot capture quantitatively the full energetics of the system, specially in such a reduced slab.

5.3 Conclusions

In conclusion, we have studied the structural and electronic effects of boron substitution on 7-AGNR. The resulting 2B-7-AGNR displays a corrugated structure as a consequence of the higher interaction between boron and the gold surface. The most prominent change on the electronic structure of 2B-7-AGNRs is the introduction of an in-gap acceptor band centered around 1 V. On the other hand, we detect the VB of the 2B-7-AGNR by combining ARPES and STS measurements. Thus, we report an effective bandgap for 2B-7-AGNR of $\sim$1.6 V, significantly smaller to that of pristine 7-AGNR.

As observed from both STS and DFT calculations, the higher interaction between 2B-7-AGNR and substrate results on a hybridization of the newly created AB with the surface bands, giving the AB a hybrid metal-ribbon character. Our results highlight the importance of the substrate in describing the structural and electronic properties of doped ribbons. This might become relevant for ribbons grown on, or transferred to, more reactive substrates.

Chapter 6

Quantum dots embedded in hybrid 7-AGNR

As seen in the previous chapters, the bottom-up synthesis of GNRs using molecular precursors is a versatile toolbox for tuning the electronic properties of GNRs. The control on the band alignment, doping and band gap allows to envision full graphene nanoribbon nanodevices. Molecular precursors can be combined to produce graphene nanoribbon heterojuntions with various functionalities. The most basic heterojunction, a p-n junction, has been created by combining pristine chevron GNR precursor with their nitrogen doped analogue [6]. Similarly, type I heterojunctions have been obtained by combining 7-AGNR with 13-AGNR [7].

One of the main advantages of these bottom-up built heterojunctions is the quality of their interfaces, which seamlessly join the different segments of the ribbon with different electronic properties. As a result, extremely sharp interfaces can be achieved leading, for example, to electric fields in a p-n junction two orders of magnitude higher than in traditional semiconductors [6].

Other active elements can be designed in GNRs to turn them into operationa nanodevices. One of such elements are quantum dots (QDs). QDs embedded inside a GNR may turn it optically active for luminescence when electrically powered through the terminal GNR segments. The construction of such hybrid devices requires a precise technology to create confining barriers for electrons inside the nanoribbons [7, 117].

Here, we show that the insertion of a pair of substitutional heteroatoms in the interior of the ribbon backbone produces very efficient confining barriers for electrons, leading to quantum well (QW) states in their valence band (VB). As seen in the previous chapter, the boron pairs locally modify the electronic properties of the 7-AGNR segments [105]. Using Scanning Tunneling Spectroscopy (STS), we find that the valence band of pristine segments between two 2B sites is discretized into states with an integer number of modes, resembling a Fabry-Perot resonator for GNR electrons [118, 119]. Electronic transport calculations reveal that the borylated segments act as perfect scatterers for VB electrons, but are transparent for the band below (VB-1). We show that this band-selective scattering depends on the difference in wave-function symmetry between 7-AGNRs bands and localized states at boron pairs. The band-specific scattering of electrons suggests that active components such as QDs can be embedded in GNRs, while maintaining fully transmitting channels for hole injection.

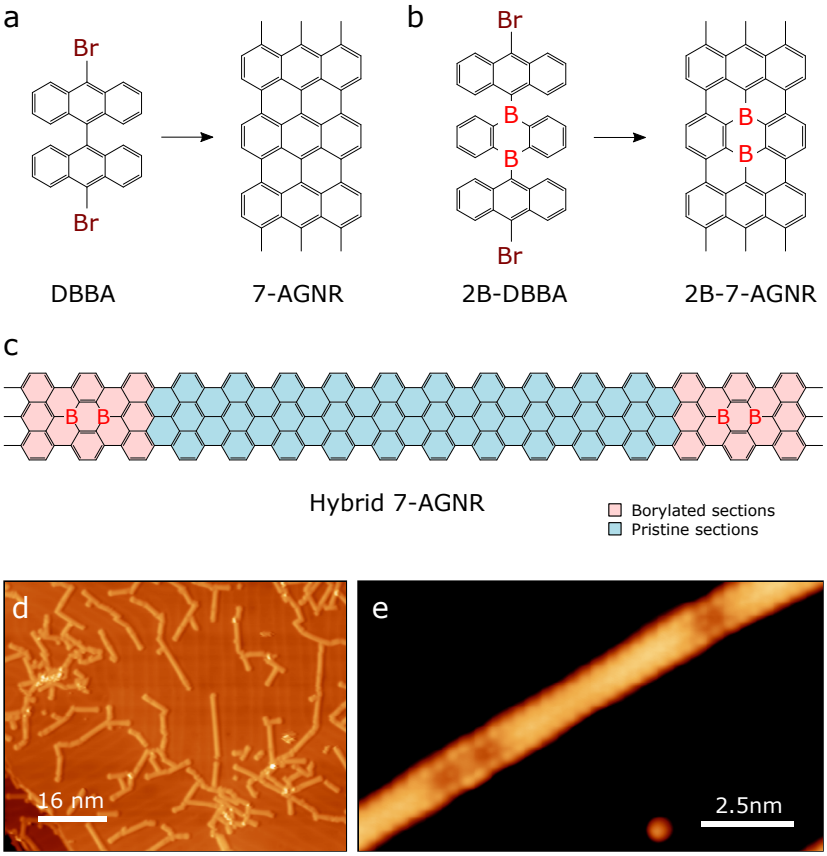

Figure 6.1: (a) Molecular structure of 10,10'-dibromo-9,9'-bianthryl (DBBA) precursors and the resulting 7-AGNR. (b) Structure of the precursor 9,10-bis(10-bromoanthracen-9-yl)-9,10-dihydro-9,10-diboraanthracene (2B-DBBA) and the resulting boron substituted 2B-7-AGNR [104, 105]. (c) Chemical structure of a hybrid 7-AGNR formed after on-surface reaction of five DBBA precursors between two 2B-DBBA molecules. Pink (blue) sections mark the borylated (pristine) regions on the hybrid structure. (d) Overview STM image of a Au(111) surface precovered with hybrid 7-AGNRs (V_s=0.6 V, I_t=70 pA). (e) Small-scale STM image of a hybrid 7-AGNR (V_s=1 V,I_t=1.7 nA). The dark spots at the center of the ribbon allows us to identify the position of the boron pairs.

We produce these hybrid AGNRs by adding a small amount of boron-substituted precursors (2B-DBBA) during the on-surface reaction of DBBA molecules (Figure 6.1a) to produce 7-AGNRs. The mixture of DBBA and 2B-DBBA precursors thus results in ribbons with a pristine 7-AGNR body and a few subunits of substitutional boron pairs (Figure 6.1c). As observed from the STM images (Figure 6.1d), DBBA and 2B-DBBA precursors aggregate to produce linear hybrid 7-AGNR of homogeneous width. At a sample bias V_s=1 V (Figure 6.1e) the borylated subunits appear as a characteristic depression in the center of the GNR backbone [104]. A mixture ratio ∼3:1 of DBBA and 2B-DBBA precursors leads to ribbons that consist of a pristine GNR body with randomly distributed pairs of boron atoms along the ribbon, with an average distance of more than 3 nm.

6.1 Electronic properties of hybrid 7-AGNR

To determine the effect of embedded boron-pairs on the electronic structure of the ribbon we performed STS measurements at different positions. Figure 6.2 shows spectral maps taken across a pristine segment (a) and a borylated segment (b). The pristine segment spectral map presents the same features as those of a fully pristine 7-AGNR; stronger dI/dV signal at the edges of the ribbons and onsets of the VB and CB+1 at -0.8 V and 1.7 V respectively, giving an transport band gap of 2.5 eV, in agreement with previous works [45,46]. On the other hand, the spectral map across the borylated segments presents similarities to those of a full 2B-7-AGNR (see chapter 5.2): onset of the CB+1 at 1.7 V with stronger contrast at the edges, a broad resonance around 1V at the center of the ribbon and lack of signal from the VB onset. The maps taken at the onset of the CB+1 (Figure 6.2c) and at 1 V (Figure 6.2d) summarize the features of the empty states of the hybrid 7-AGNR. The CB+1 is almost unaltered by the presence of the borylated segments and a localized in-gap state appears in the borylated subunits. Fom the maps at 1 V (Figure 6.2d) we can also extract that in this small boron concentrations, the impurity states are localized and do not hybridize into an acceptor band, in contrast with the fully borylated 2B-7-AGNR.

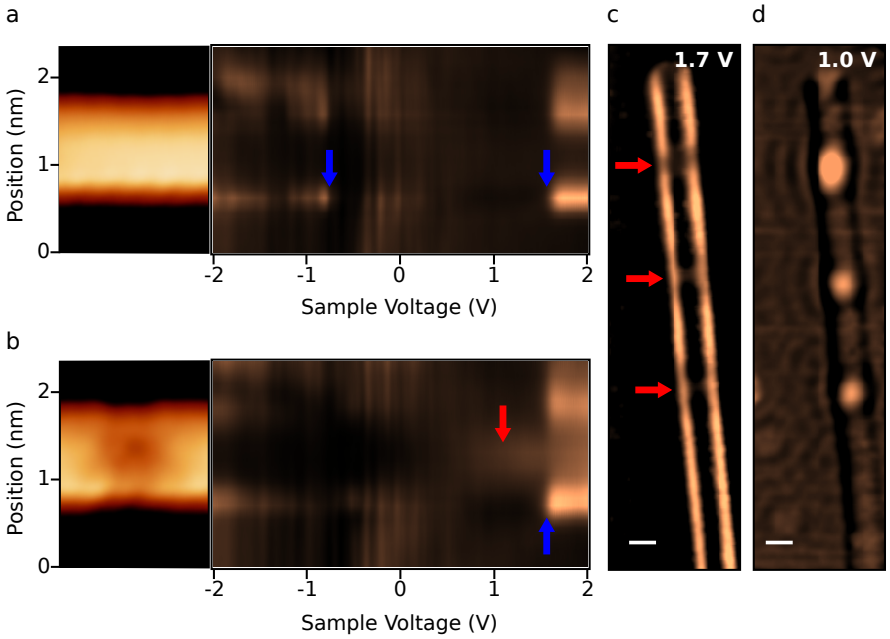

Figure 6.2: (a) Spectral map taken across a pristine segment as in the topography inset. Blue arrows mark the onset of the VB and CB+1. (b) Same as in panel *a* but across a borylated segment. Blue arrow marks the onset of the CB+1 and red arrow shows the localized boron state, reminiscent to the acceptor band in 2B-7-AGNR. (Open feedback conditions for *a* and *b*: V_s=1 V, I_t=0.41 nA, V_{rms}=12 mV, f =767.7 Hz (c) Constant current dI/dV map of a hybrid 7-AGNR taken at the bias of the onset of the CB+1 (1.7 V) . The red arrows mark the positions of the borylated segments. (d) Same as in panel *c* but at the maxima of the in-gap boron induced state (1 V). Scale bars are 1nm (Parameters for *c* and *d*: I_t=150 pA, V_{rms}=20 mV, f =800 Hz).

Figure 6.3a shows spectra at the edges of pristine (blue) and borylated (red) segments. At the edges of the 2B sites, the VB of the pristine regions is completely absent. The absence of VB signal at the borylated segments is clearly observed in differential conductance (dI/dV) maps measured at V_s=-0.8 V, i.e. at the pristine VB onset (Figure 6.3c). An enhanced dI/dV signal is mostly observed along the ribbon

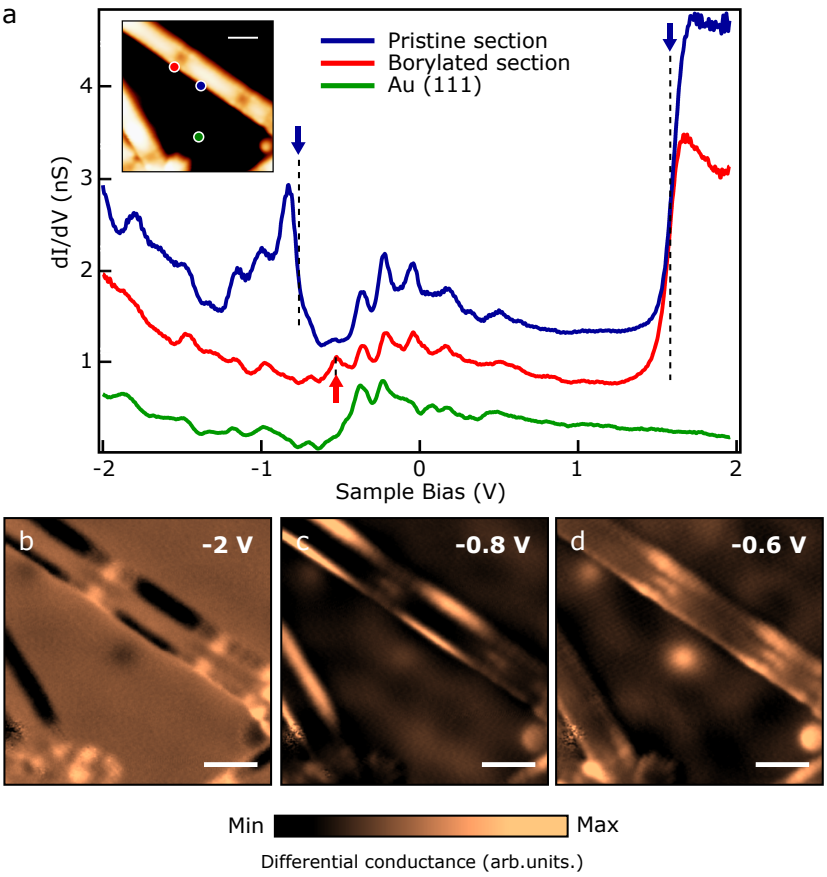

Figure 6.3: (a) Differential conductance (dI/dV) spectra taken at different sites of the hybrid GNR. Blue spectrum acquired at the edge of a pristine section. Red spectrum acquired at the edge of a borylated section. Green spectrum acquired over the Au(111) substrate. Blue arrows and dashed lines mark the onset of the CB+1 for the pristine and borylated section and the onset of the VB for the pristine segment. Red arrow marks the boron localized state in Figure 6.3d. All spectra were taken with the same tip and are vertically offseted for clarity (open-feedback parameters: V_s=1.0 V, I=0.41 nA, V_{rms} =12 mV, f =767.7 Hz). States between -0.45 eV and 0.5 eV are the Shockley surface state band of Au(111). The peaks below the VB onset, at -0.9V and -1.1 V, are due to band discretization, discussed later in the text. (b) Constant current differential conductance maps of the hybrid nanoribbon shown in the inset of Figure 6.3a at V_s=-2 V, showing a localized state around the boron regions. (c) Same as in panel *b* but bias voltage is chosen at the energy of the onset of the pristine VB, V_s=-0.8 V. (d) Same as in panel *b* but at a bias voltage where the first localized states of the borylated sections appear, V_s=-0.6 V. Differential conductance maps feedback conditions: I=0.5 nA, V_{rms}=16 mV, f =767.7 Hz. All scale bars are 1.8 nm.

edges of pristine parts, appearing strongly suppressed around the boron sites. The dI/dV maps additionally reveal that boron pairs exhibit two localized states at -2 eV and -0.6 eV (Figures 6.2b and d, respectively).

6.2 Confinement of the Valence Band

The VB suppression indicates that the 2B sites act as scattering centers for electrons. Indeed, the valence band of pristine nanoribbon sections enclosed by two borylated subunits shows fingerprints of energy discretization (6.4a) suggesting quantum confinement of electrons. dI/dV maps show that the valence band appears with a series

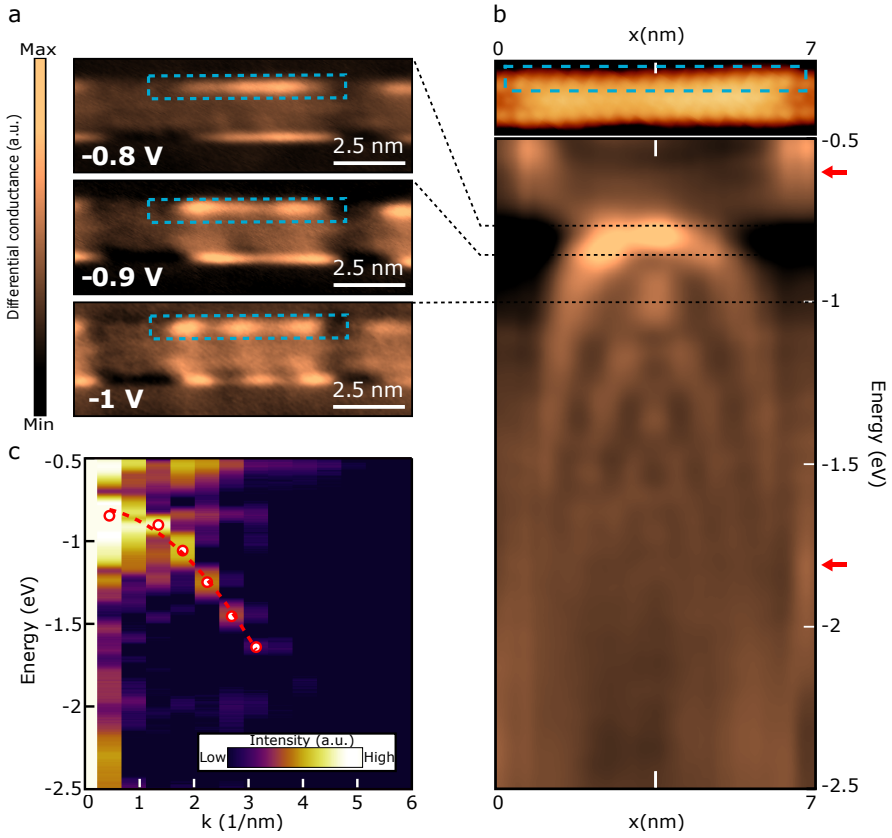

Figure 6.4: (a) Constant current differential conductance maps of hybrid GNR, taken at energies where the spatial modulation of the VB of the pristine sections is seen. The maps show from one up to three maxima. Dark regions at the edge of the ribbon coincide with the position of the borylated sections of the ribbon. Differential conductance maps feedback conditions: I_t=0.5 nA, V_{rms} =20 mV, f =743.4 Hz. (b) Stack plot of constant current differential spectra taken along the edge (marked in the topography image on top with blue dotted rectangle) of a pristine section confined between two borylated sections. Red arrows mark the 2B localized states of figure 2b and 2d. Constant current feedback conditions: I_t=1 nA, V_{rms} =14 mV, f =743.4 Hz (c) Line-by-line Fourier Transform of *b*, including the parabolic fit used for extracting $E(k = 0)$ and m^*.

of maxima along the edges of the nanoribbon. Furthermore, the number of maxima increases with bias voltage, which is characteristic of a quantum well (QW) system.

A dI/dV spectral map along the pristine GNR segment depicts the full energy distribution of the VB quantum well states (Figure 3b). The first QW state is located at -0.85 eV, and overlaps with the second one due to their energy broadening. The third state located at -1 eV has three evident maxima. The quantized levels go as high as N=7 at an energy of -1.7 eV. Below this energy, no additional confined states are observed, probably due to their overlap with the state localized at the 2B sites at -2 eV (Figure 2b).

The line-by-line Fast Fourier Transform (FFT) of Figure 3b reproduces the dispersive behavior of the confined VB (Figure 3c). From a parabolic fit $E(k) = E(k = 0) + \hbar^2 k^2/2m^*$ of the FFT-STS spectral map we deduce a band effective mass of $m^* = 0.43 \pm 0.03 m_e$, in correspondence with pristine 7-AGNRs [46, 80]. Additionally we estimate from the fit that the top of the band lies at $E(k = 0) = -0.79 \pm 0.03$ eV as in bare 7-AGNR [46]. Therefore, we conclude that boron pairs do not act as charge dopants, but only as scatterers. This behavior is observed in multiple confined segments of different lengths found in the same ribbon (Figure 6.5a). Figure 6.5 shows the spectral maps of QWs of 4.5 nm (b), 7 nm (c, as in Figure 6.4) and 3.5 nm (d). The energy dispersions for all three QWs (e) coincide nicely with each other. Moreover,

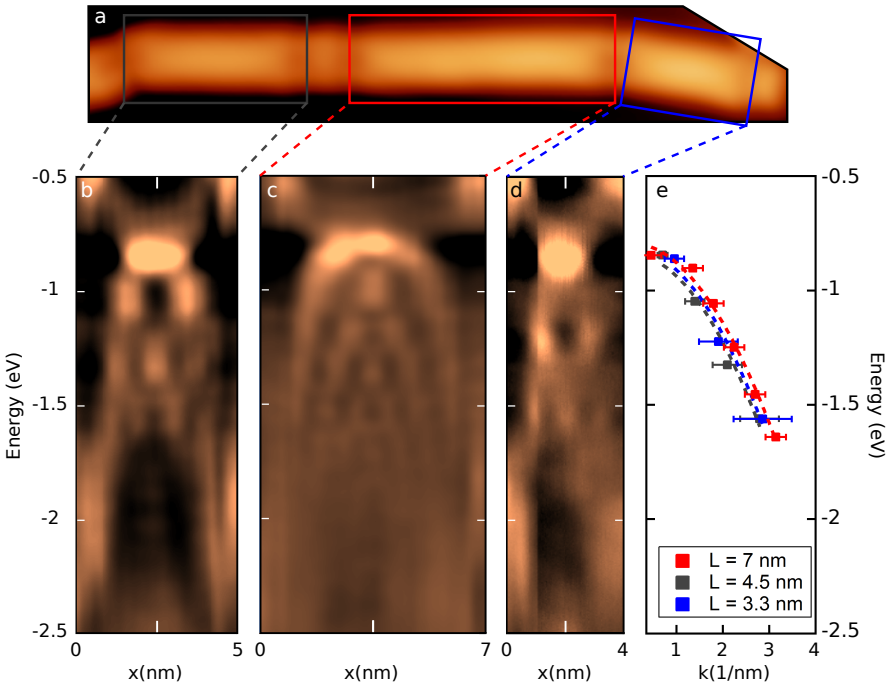

Figure 6.5: (a) STM topography of a hybrid ribbon with multiple confined pristine regions, marked with colored squares (I_t=0.43 nA, V_s=-400 mV). (b-d) Spectral maps of the 3 confined regions highlighted in panel *a*. Panel *b* has been extracted from 6.4b. Feedback conditions for *b* and *d*: I_t=2 nA, V_{rms} =14 mV, f =743.4 Hz(e) Energy dispersion relation ($k = n\pi/L$) for three quantum wells of different lengths. The data in red corresponds to the QW shown in 6.4b for comparison. Dashed lines show parabolic fits to each data set, showing a good overlay of all energy dispersions.

from the dispersions we can infer that there is little to no coupling between the QWs, since the energy levels are not pinned to particular energies.

There is a significant difference between the spectral features of the QWs shown in Figure 6.5b and d, and those shown on Figure 6.5c. The QW in 6.5c shows a diffuse parabolic envelope, where the different quantum levels are not easily discerned between each other. This effect is particularly acute in the first three quantum well levels. On the other hand, the QWs spectral maps of 4.5 nm and 3.3 nm show well defined quantum well levels, properly delimited in energy.

We interpret the different contrast of QW states with the of the well width using a very simple model that correlates the lifetime of an excited hole in a QW state with the time an electron requires to travel back and forth through the well. From a rough analysis of our results, we can extract approximated values for the lifetime of the quantum well levels and the charge carrier velocity of the confined VB. Figure 6.6a shows the lifetime of the energy levels from Figure 6.5b and c, extracted from the linewidth of the spectral features and after the substraction of the gaussian broadening induced by the lock-in during the spectra acquisition. All the lifetimes are in the order of 10 fs. This time is slightly shorter than the lifetimes of confined surface state electrons in Ag(111) [120]. By numerically deriving the energy dispersions of the 7 nm and 4.5 nm QWs in Figure 6.5e we extract the group velocity of the charge carriers of the confined VB ($v = \hbar^{-1}\partial E/\partial k$). The velocity is momentum (energy) dependent, and decreases towards zero at the maxima of the VB. The maximum velocity ($\sim 6{\times}10^5$ m/s) is reached around -1.3 V, which is in very good agreement with ARPES measurements, and close to the constant carrier velocity in graphene $v_0 = 10^6$ m/s [45].

Both the lifetime and velocity allows us to roughly estimate the number of times a VB electron can travel through the confined region and coherently contribute to the scattering process ($\#travels = v\tau/L$ where v is the group velocity, L is the well length and τ is the lifetime at a certain energy). Figure 6.6c shows how, in the case of the

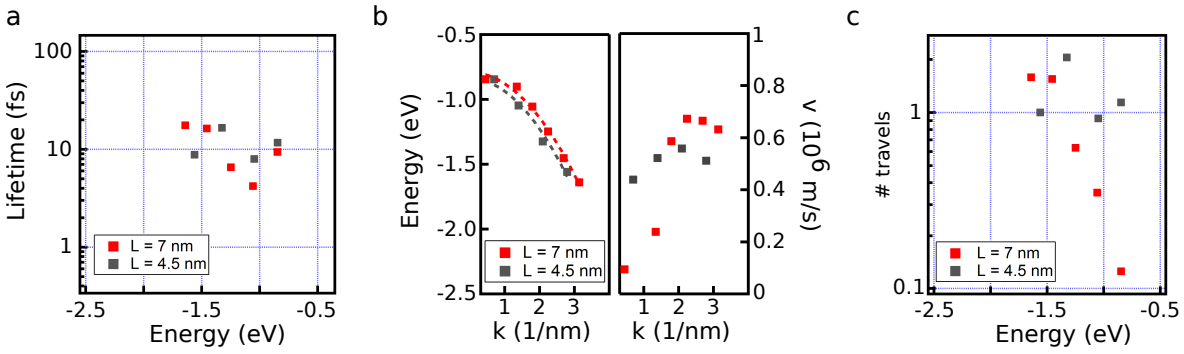

Figure 6.6: (a) Extracted lifetimes from the spectral maps in Figure 6.5 panel *b* (gray) and *c* (red). The gaussian broadening induced by the lock-in in the linewidth of the levels has been removed. Due to the overlap between quantum levels N=1 and N=2 of the 7 nm QW, the lifetime of N=2 was not possible to obtain.(b) Energy dispersion from Figure 6.5e and their derived group velocities ($v = \hbar^{-1}\partial E/\partial k$). (c) Number of travels across the confined regions defined as $\#travels = v\tau/L$). All levels of the 4.5 nm QW are close to one full travel, while N=1, N=3 and N=4 levels for the 7 nm QW are below an integer number of travels.

QW of 7 nm (red), the quantum levels N=1, N=3 and N=4 (the lifetime of N=2 was not possible to define) are well below an integer amount of travels through the confined section. In contrast, for the QW of 4.5 nm (gray), the electrons of all QW levels are able to travel one time through the confined region. This provides an interpretation on why the QW levels of narrower QWs are better defined, since electrons can coherently contribute to the scattering process. For longer QWs (Figure 6.5c) electrons loose their phase coherence before reaching the other QW end, and as a consequence the quantum well levels are blurred one with each other.

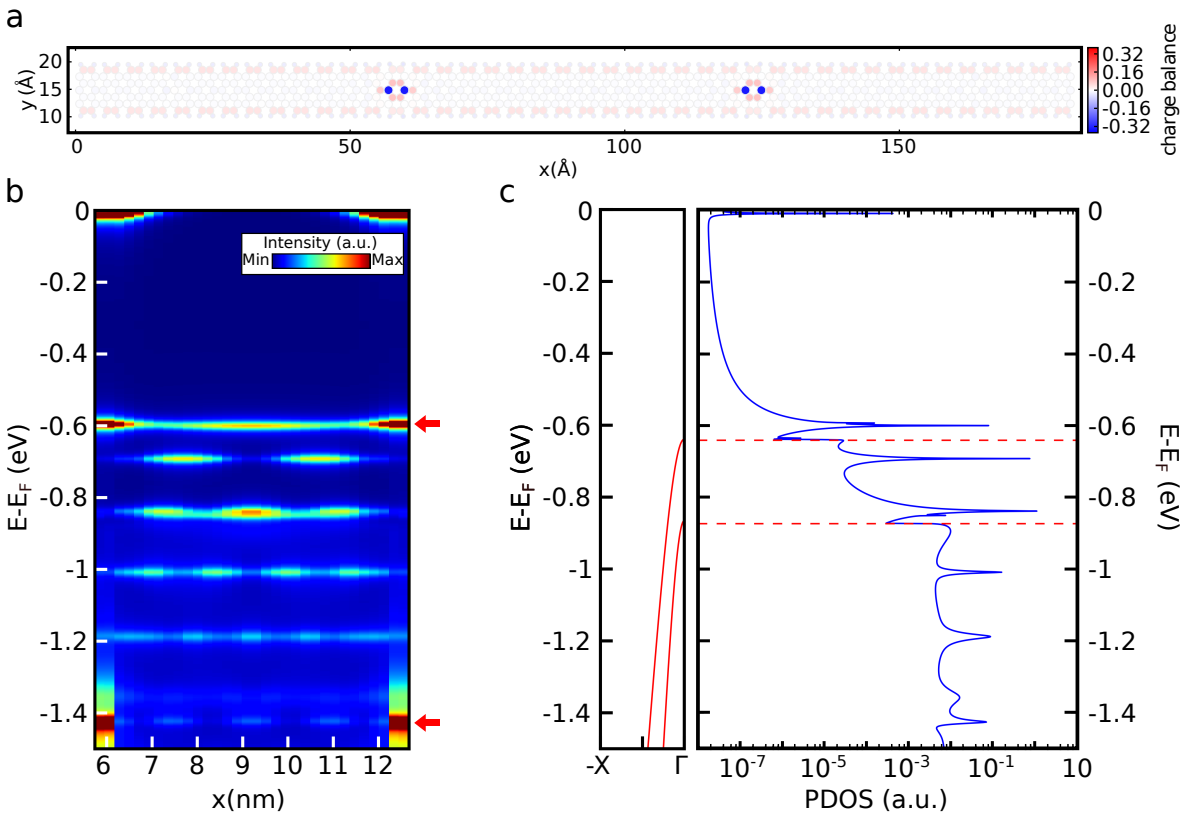

Figure 6.7: (a) Mulliken population analysis of the freestanding hybrid 2B-7-AGNR. The boron atoms are negatively charged, receiving an amount of ∼0.38 electron charge from the neighbouring carbons which, in turn, are positively charged.(b) PDOS for a pristine segment enclosed between two borylated sections 65 Å apart. Quantized levels up to N=5 are clearly observed between the boron localized states. Red arrows show boron resonances with strong boron p_z character, corresponding to localized states found in the spectral map of Figure 6.4b. (c) VB and VB-1 dispersion for a pristine 7-AGNR (left) and PDOS profile (right) obtained at the middle position between the two borylated sections. The vertical dashed red lines correspond to onsets of the pristine VB (∼-0.64 eV) and VB-1 (∼-0.87 eV).

6.3 Electronic transport through a hybrid 7-AGNR

In order to investigate the origin of the band confinement we performed first principles calculations via Density Functional Theory (DFT) on a free-standing 7-AGNR with two diboron substituted subunits separated ∼65 Å apart which behave as weak charge acceptors (Figure 6.7a). The open system was simulated by coupling each terminal from the hybrid GNR to semi-infinite pristine ribbons, which act as electrodes. We first calculated the density of states (DOS) along the central pristine segment, and project it onto atomic columns across the 7-AGNR section. Figure 6.7b depicts the corresponding projected DOS (PDOS) plotted along the confined region, showing that it consists of discrete levels with an integer number of DOS maxima between the boron subunits, as in the experimental dI/dV spectral map of 6.4b. From the evolution of the confined levels with energy we obtain an effective mass of $m^* = 0.36 \pm 0.02 m_e$, considering a particle in a box model with hard walls, i.e. $k_n = n\pi/L$. The small difference of band's effective mass with respect to the experiment might be related to the role of the surface, not included in the simulations.

The DFT results thus confirm the strong confinement of the valence band between boron pair sites, which suggests that they behave as very effective scatterers for VB electrons. To get more insight on the scattering properties of these sites we simulated the electronic transport through these hybrid graphene nanoribbons. Figure 6.8a compares the energy-dependent electronic transmission (probability of an electron to propagate from one electrode to the other) along a pristine ribbon (red) with the case of including a single boron pair site (green-dashed) and two of them forming a quantum well (blue). The transmission through a pristine 7-AGNR shows a typical step-like behavior with the opening of new channels corresponding to the available bands (VB and VB-1 in the plotted energy window). The effect of including a single 2B site in the ribbon is drastic: the transmission of the VB is almost completely suppressed. In contrast, the VB-1 is apparently not affected by the impurity, exhibiting an onset to a baseline of transmission about 1. Thus, a single boron pair acts as a hard barrier for VB electrons but is fully transparent for VB-1 electrons.

This peculiar band selective behavior is also expressed in the transmission through the double 2B quantum-well case. The VB shows zero transmission except for narrow peaks of T∼1 at the energies of the QW states, supporting that this system is the electron analog of a Fabry-Perot (FP) resonator. At the onset of the VB-1, the transmission shows again a step like behavior to T∼1, and resonant peaks reaching T∼2. Looking at the eigenchannel's wavefunctions at energies between resonant peaks (Figure 6.8b), we resolve that the baseline T∼1 corresponds to the VB-1, which is fully transmitted through the double-barrier system. The VB is strongly reflected at the first 2B-site, except at the energies of the QW states, where it expands with the nodal structure in the resonator (Figure 6.8c) and transmits with narrow FP-peaks. The FP resonator is manifested not only in the nodal structure, but also in a higher wavefunction amplitude between the 2B-sites when compared to the incoming wave. From the sharp transmission lines at the Fabry-Perot modes we corroborate that 2B sites reflect VB electrons with R∼1. We note that this is in absence of any surface acting as support. In the experiments, the linewidth of the quantum-well levels is significantly broader due to the presence of a metal surface.

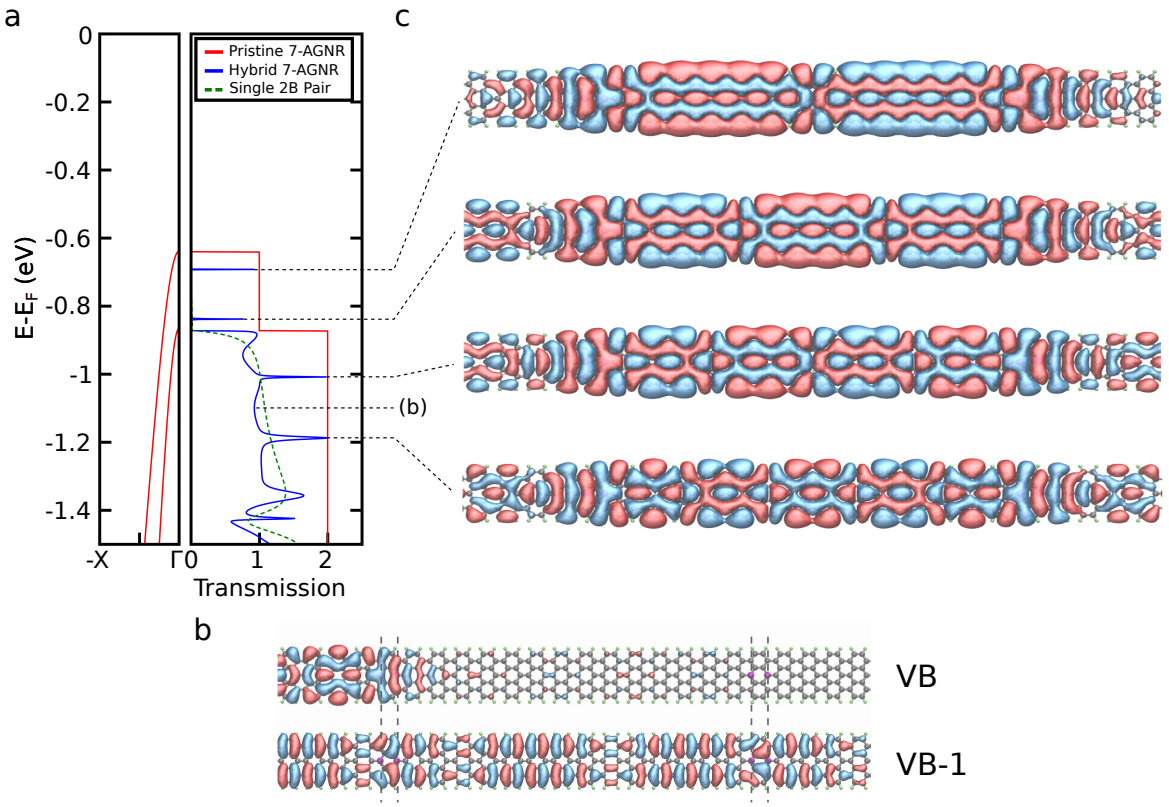

Figure 6.8: (a) VB and VB-1 dispersion for a pristine 7-AGNR (left) and Transmission function (right) for a pristine ribbon (red), a single boron pair (dashed green) and for the confined system formed by two boron pairs (blue). The transmission function shows the strong reflectivity of a single boron pair and the Fabry-Perot behavior of the double 2B-barrier system. The transmission through the N=1 quantum level is not seen because this state lies in the energy gap of the electrodes. (b) Real part of the eigenchannel functions taken at $E - E_F = -1.10$ eV (dashed-dot line in panel *b*), i.e. between quantized levels. The eigenchannel corresponding to the VB shows no transmission through the boron segments, while VB-1 fully transmits through. (c) Real part of the eigenchannel functions taken at the energies corresponding to the N=2,3,4 and 5 quantum well levels.

The origin of the band selectivity in the electron scattering is related to the specific symmetry of the electronic wave functions of the AGNR bands and the boron-induced states. Figure 6.9a shows the Highest Occupied Molecular Orbital of a molecule simulating the borylated 7-AGNR segment, which has the strongest boron p_z character. This state reflects the symmetry of the boron localized states in the hybrid 7-AGNR, marked in Figure 6.7a with red arrows. In particular, this state has an even symmetry across the AGNR. VB states are also even-symmetric across the AGNR, while VB-1 states have odd symmetry and, hence, expose a nodal plane at the center of the AGNR backbone (Figure 6.9b). Therefore, boron-localized states hybridize with the valence band, but are orthogonal to the VB-1 band. The hybridization has been verified by investigating the wave functions obtained from a periodic calculation of a 7- AGNR with a single boron dimer (Figure 6.9c). The band corresponding to the pristine nanorib-

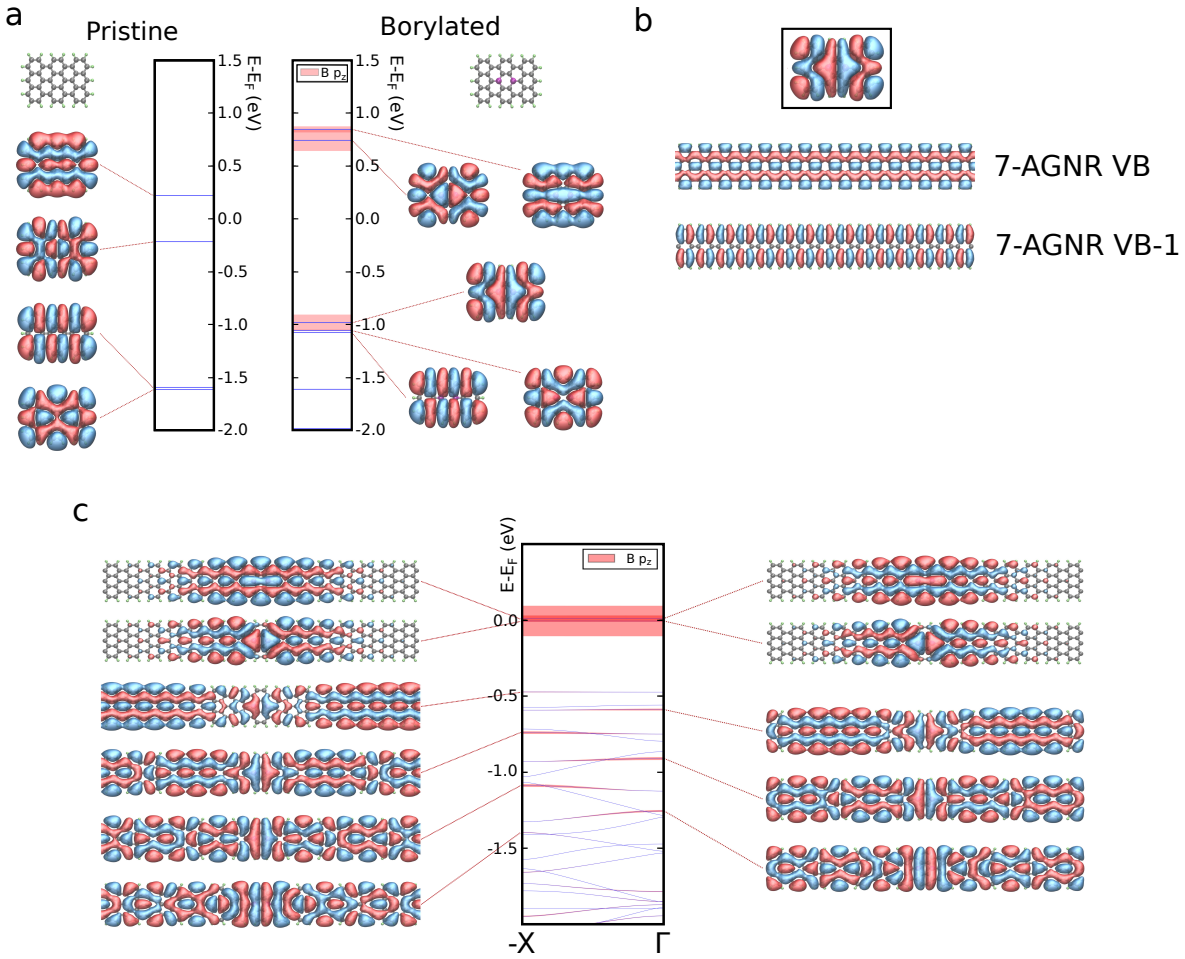

Figure 6.9: (a) Wave functions and corresponding energy levels obtained for a pristine trisanthene molecule (left) and for a trisanthene molecule with a substituted pair of boron atoms (right). In the considered energy range, the boron-substituted molecule presents a new energy level (at $E - E_F = -0.98$ eV) with strong boron p_z character (shadowed in red). (b) Real part of the wavefunctions for the boron-induced HOMO, and for the pristine 7-AGNR VB and VB-1 bands at Γ-point. Both the boron state and the VB show a even symmetry with respect to the mirror plane bisecting the GNR along its axis, while VB-1 has odd symmetry. (c) Band structure (center) obtained for a 7-AGNR with a periodic boron pair substitution. The unit cell of the ribbon has been chosen so that the distance between the boron dimer and its next periodic replica is equal to that of the open system calculation, i.e. 65 Å. The nodal structure, analogous to that of Figure 6.8c, is observed.

bon valence band (VB) strongly hybridizes with a boron resonance and appears with a stronger boron p_z character alternately at Γ and -X points.

The boron states also present a nodal plane at the center of the boron pair, which imposes the presence of a node at that location for the confined states derived from the AGNR VB. This is the origin of the large VB-scattering at the 2B-sites. The VB-1 transmits freely because it cannot mix with boron states, and its wavefunction amplitude remains essentially unaffected by the 2B-segments. In the experiments, the

VB-1 onset is weakly sampled by the STM tip [46] and, therefore, hardly visible in point dI/dV spectra. This band, if confined, should be easier to detect due to its localized character. Additional modes should arise around -1.5 eV [45], which is not the case in our experiments, supporting the absence of VB-1 confinement.

6.4 Conclusions

We have shown that hybrid 7-AGNRs with a small amount of 2B substitutional subunits give rise to quantum-well states due to electron confinement in the region between two 2B sites. The boron pair units act as local scatterers for one of the two valence bands of the 7-AGNR while leaving the other unaffected. First principles calculations on a free standing hybrid 7-AGNR qualitatively reproduce our experimental results and evidence that the band selective nature of the confinement is due to the different symmetry of the bands of the pristine ribbon and the scatterer states; only states with matching symmetry are affected. The presented band-selective procedure to manipulate only some bands envisions embedding functional devices in GNRs while transmitting charge through other unaffected bands. Furthermore, our results indicate that the substitutional doping of conjugated conductors with heteroatoms goes beyond a simple charge doping model and can be a method to manipulate bands' wave-function and transport channels.

Part III

On-surface synthesis of graphene nanostructures

Beyond armchair, zigzag or chiral GNRs, other carbon based nanostructures also hold great interest for potential applications in the field of organic electronics. Being π-conjugated systems, polycyclic aromatic hydrocarbons (PAH) can act as active components in devices such as field effect transistors, light emitting diodes and solar cells [121, 122].

In recent years, solution chemistry has been successfully employed to obtain PAHs with fascinating structures following a bottom-up approach [123–127]. However, the large size and the extremely low solubility of these molecules severely complicates their manipulation and characterization. Combined sub-molecular atomic force microscopy (AFM) and scanning tunneling microscopy (STM) have demonstrated to be privileged tools to study insoluble nanographenes prepared by solution chemistry [128–131]. An important drawback of these methods is that they require the sublimation of the material on an adequate surface, which limits the size of the molecules that can be studied. As seen in previous chapters, the on-surface synthesis approach circumvents these limitations by using specially designed molecular precursors as building blocks.

Here we focus on the on-surface synthesis of two different PAHs, originating from two similar triphenylene based precursors (Figure 6.10). On the one hand precursor **A** leads to a chevron-like GNR, consisiting on a (6_A,6_A) chevron branch [51,132] decorated with nine six-carbon rings. On the other hand, precursor **B** leads to the formation of 0D trimer structures hosting peculiar pore electronic states at their centers.

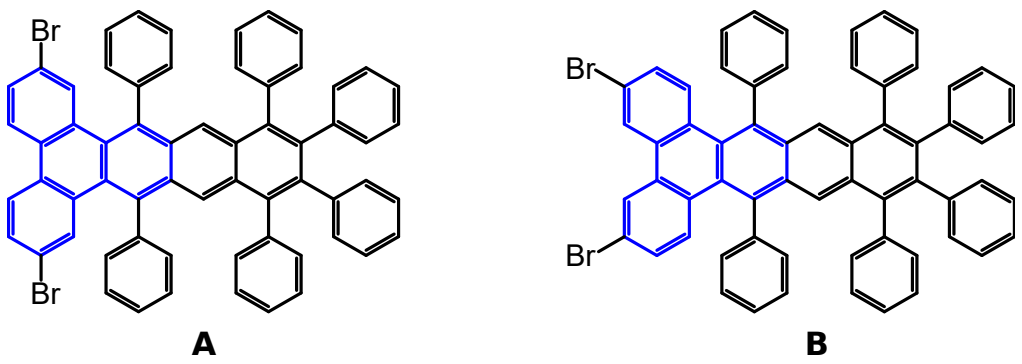

Figure 6.10: Chemical structures of the precursors used to grow PAH. The triphenylene subunit is highlighted in blue.

Chapter 7

On-surface synthesis of a chevron decorated ribbon

Chevron graphene nanoribbons (CGNRs) are graphene nanostructures that periodically combine AGNR and ZGNR sections with different growth directions. These so-called graphene nanowiggles are particularly interesting not only because they share most of the electronic and magnetic properties of the different armchair and zigzag segments, but also from the emergence of new behaviors from the interaction between these sections.

CGNRs have been classified by Costa Girão *et al.* [132] depending on the widths

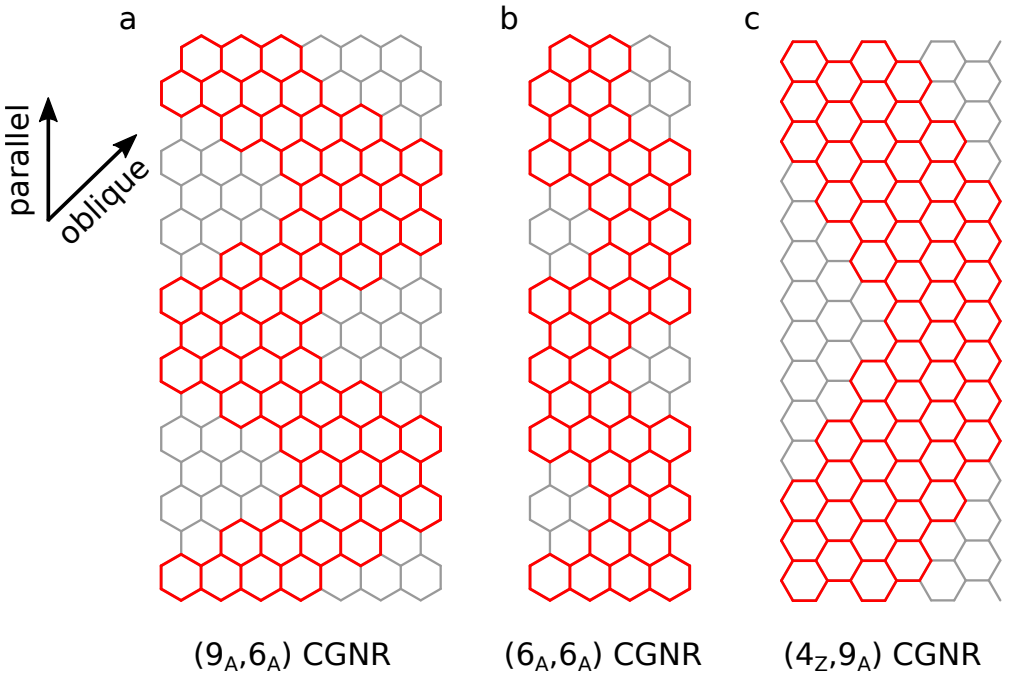

Figure 7.1: Structures of different CGNRs. (a) (9_A,6_A) CGNR as grown in previous works [5, 6, 102]. (b) (6_A,6_A) CGNR, which will be the framework for the results in this chapter. (c) (4_Z,9_A) CGNR. Note the rotation of the underlaying graphene lattice respect to panels *a* and *b*.

and type of the ribbon parallel and oblique segments. The nomenclature used consists in a pair of numbers (P_α, O_β), each of them accounting for the width of the parallel (P) and oblique (O) segment. The subindexes α and β stand for the edge type, armchair (A) or zigzag (Z) in each region. We note that the width convention used is the same as the one explained in chapter 2: zigzag lines for zigzag segments and carbon dimer lines for armchair segments. Thus Figure 7.1a shows the structure of the $(9_A,6_A)$ CGNR, previously synthesized by Cai *et al.* [5]. On the other hand, Figure 7.1c shows the structure of a CGNR combining both zigzag parallel segments with armchair oblique segments.

It has been shown that purely armchair CGNRs behave as semiconductors, with bandgaps defined by the same relation that AGNRs follow, i.e. $E_{g,3p+1} > E_{g,3p} > E_{g,3p+2}$. The bandgaps of (P_A,O_A) CGNRs follow a trend that depends on the building block segment with the smallest bandgap, which in its turn, depends on the width and AGNR family of said segment. On the other hand, CGNRs combining zigzag and armchair segments display spin ordering in zigzag edges separated by armchair segments [132].

Here we focus on the STM[1] study of the on-surface growth of a modified CGNR on top of Au(111), composed of a $(6_A,6_A)$ CGNR branch decorated with small nanographene moieties. These moieties, consisting in nine six-carbon rings, could host localized states coupled to the semiconductor chevron branch. The resulting structure holds interest for potential functionalizations of GNRs or other PAH without the addition of het-

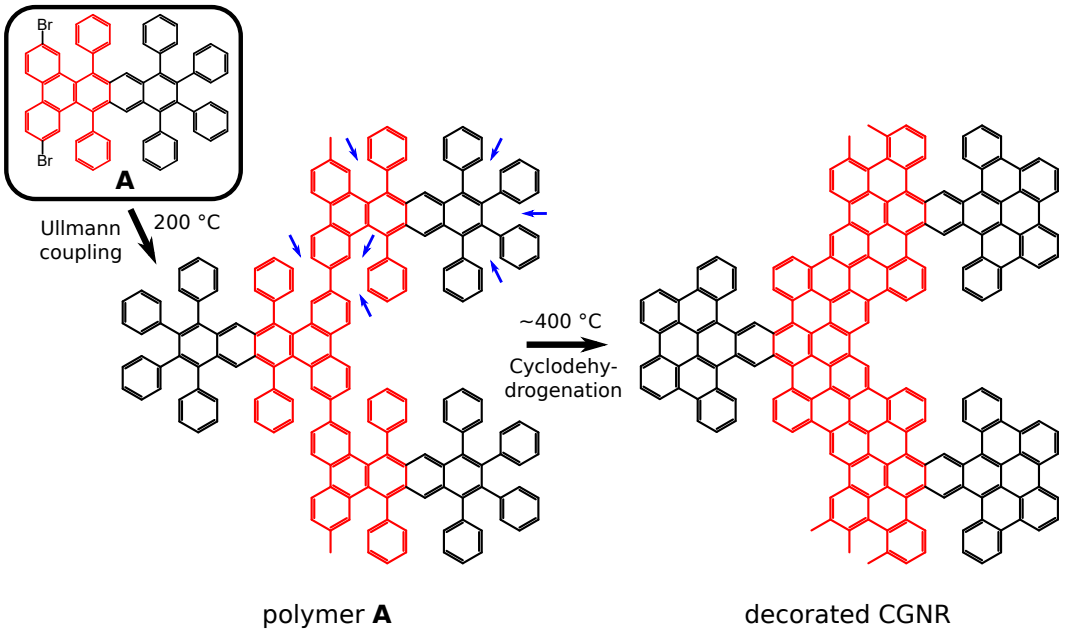

Figure 7.2: Reaction scheme to grow decorated $(6_A,6_A)$ CGNRs. Monomer **A** reacts via Ullmann coupling, creating polymer chains (polymer **A**) with several highly steric repulsive sites (marked with blue arrows). After post annealing to higher temperatures, the cyclodehydrogenations trigger planarizing the final decorated CGNR. Red highlights the portions of the monomer, polymer or ribbon building up the $(6_A,6_A)$ CGNRs branch.

[1]We note STM images in this chapter were acquired at 77K.

eroatoms altering the chemistry or reactivity of the final compound.

The reaction pathway to grow the decorated CGNRs is depicted in Figure 7.2. Precursor **A** consists in a triphenylene center joined to a naphtalene subunit. Six phenyl rings protrude from the center of the molecules resulting in a non-planar molecule, as a result of the steric repulsion between phenyl rings. We sublimated precursor **A** from a Knudsen cell held at 230 °C on top of a Au(111) substrate kept at room temperature. Figures 7.3a and b show the STM images of the as-deposited precursors. The monomers arrange in stripe-like islands that extend over tenths of nanometers and that do not follow the herringbone reconstruction. Close inspection of these islands show a high degree of order, with monomers π-stacking in multiple rows. The inset in Figure 7.3b also shows the STM shape of the monomer consisting in a flat rectangular region connected to six protrusions. The positions of these protrusions coincides with the

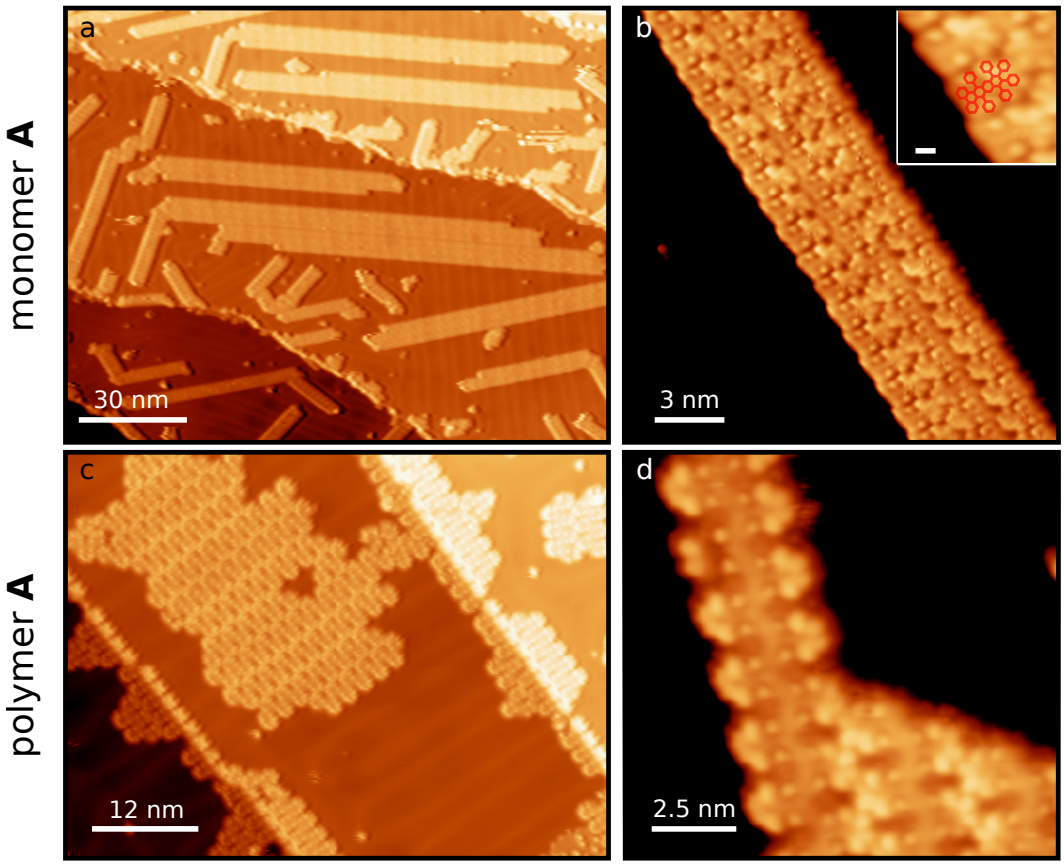

Figure 7.3: (a) STM overview of the as-deposited monomers, which organized in stripe-like islands (V_s=1 V I_t=100 pA). (b) Close view of one of the islands. The monomers arrange in multiple rows, with the bromine region of the monomers facing the outside of the island in all cases. Inset shows the STM shape of each monomer with a precursor structure superimposed in red (scale bar is 5 Å , V_s=1 V I_t=100 pA). (c) STM overview of the reacted polymers. The islands are formed by rows of polymers (V_s=1 V I_t=100 pA). (d) Close view of a polymer chain, displaying a connected central branch surrounded by brighter lobes as a result of the out of plane conformation of the phenyl rings in polymer **A** (V_s=100 mV I_t=100 pA).

positions of the six out of plane phenyl rings, confirming that the monomer structure is preserved upon evaporation.

Upon annealing to 200 °C, the morphology of the molecular islands changes (Figure 7.3c). Close inspection (Figure 7.3d) shows that the islands are formed by rows of polymer chains, each of them consisting on a faint zigzagging central region with equally spaced pairs of protrusions at each side. Surrounding this structure we find groups of four brighter lobes at alternating sites. As in the case of the unreacted molecules, the positions of these protrusions coincide with those of the out of plane phenyl rings in polymer **A** (Figure 7.2), which confirms the success of the Ullmann coupling process. The non planar structure of the polymer also confirms the energy hierarchy between the polymerization and cyclodehydrogenation steps of our reaction.

Following the polymerization step we annealed the sample at 420 °C for 10 minutes in order to trigger cyclodehydrogenation reactions that planarize the structure of the polymer chains. Figure 7.4a shows an overview of the sample after the thermal treatment. The chains do not arrange in π-stacked islands anymore, similar to the case of pristine 7-AGNR (see Chapter 3.1), pointing towards the formation of the decorated CGNRs. We also observe a high number of interlinks between the different chains, probably as a result of unwanted interribbon cyclodehdrogenations. Close inspection of the chains (Figure 7.4b) confirms the planarization of the polymers into our decorated CGNRs, their structure resembling the one proposed in Figure 7.2. However, the ribbon lobes show two possible tilts respect to the central branch (blue dashed lines in Figure 7.4b) that cannot be ascribed to the symmetric structure of Figure 7.2. These tilts result in disordered ribbons and also unwanted C-C couplings when two adjacent lobes have opposite orientations (Green arrows in Figure 7.4b).

In order to avoid unwanted additional couplings we synthesized again the decorated

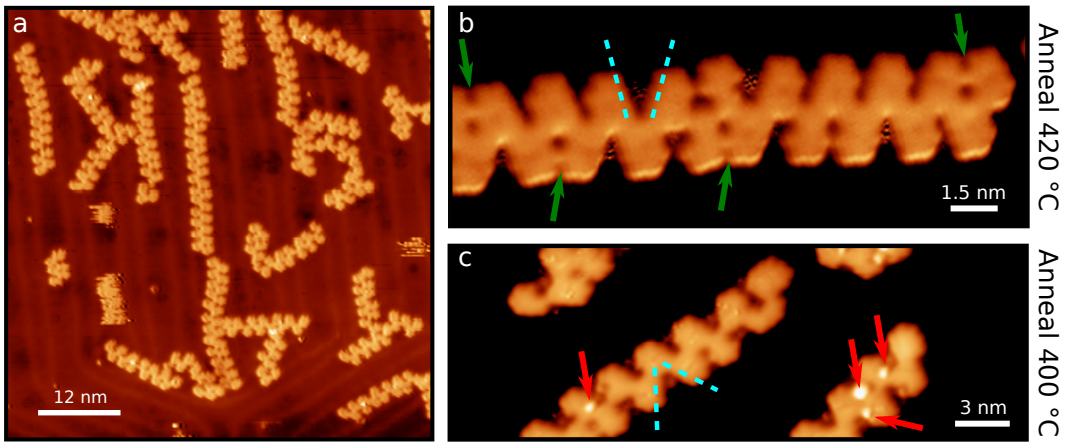

Figure 7.4: (a) STM overview of the planarized decorated CGNRs after annealing to 420 °C. The ribbons appear disperse over the surface, with links between chains (V_s=100 mV I_t=93 pA). (b) Close view of a CGNR after the sample is annealed to 420 °C. Green arrows show the position of interlinked lobes, while dashed light blue rectangles highlight asymmetries in the lobes orientation (V_s=100 mV I_t=74 pA). (c) Close view of the ribbons in panel *a*. Red arrows point the presence of protruding unreacted phenyl rings (V_s=-1 V I_t=100 pA).

CGNRs, this time lowering the cyclodehydrogenation temperature to 400 °C during 5 minutes. The resulting ribbons (Figure 7.4c) still presented the same asymmetries. In addition, numerous bright protrusions appeared within the ribbons (red arrows), indicating the presence of unreacted, non-planar phenyl rings, and thus evidencing the incomplete cyclodehydrogenation of the ribbons.

To summarize, we have shown the growth of decorated CGNRs on top of Au(111). The monomer structure is preserved upon evaporation and the subsequent Ullmann coupling is successful, yielding the expected polymer chains. However, the cyclodehydrogenation step results in heterogeneous ribbons. While the CGNRs are mostly planar, we observe two possible lobe orientations that contribute to the disorder of the ribbons, on occasions leading to C-C couplings between adjacent lobes. This suggests that the growth of homogeneous decorated CGNRs is unlikely.

The asymmetries observed in the lobes could origin from additional cylodehydrogenation reactions occurring within each ribbon subunit. The following chapter shows, indeed, the formation of benzoazulene moieties within the trimer structures resulting from the coupling of three monomers **B** (Figure 6.10). Since **B** is just an isomer of **A**, this hints towards a similar process occurring in the decorated chevron ribbons and in the trimer structures.

Chapter 8

On-surface route for producing planar nanographenes with benzoazulene moieties

So far we have shown that the typical on-surface synthesis approach is based on a sequence of thermally activated Ullmann couplings to polymerize dibromo-substituted monomers. Following this, surface-induced cyclodehydrogenation reactions turn molecular sites with high steric repulsion into benzenoid groups, planarizing the resulting reaction products. A step beyond this method is the controlled on-surface synthesis of other cyclic compounds, such as cyclopentadyenes [133] or azulenes, which hold promise in the growth of strained [127] or three dimensional [134] graphene based nanostructures.

The basic distortion of a graphenoid structure is a Stone-Walles (SW) defect, an azulene motif (a seven- and five-member ring) created from two six-member rings simply by rotating a bond [135, 136]. SW type of cycles do not modify the functional behavior of graphenoid planes, and can add flexibility, adaptability to contacts and strain.

Here, we present the on-surface synthesis of a 64-ring PAH with benzoazulene moieties on Au(111). Our results show a promising new strategy to incorporate pairs of azulene groups inside nanographene structures by suitably introducing small cavities in the structure of the precursor. We describe the on-surface preparation of this exotic nanographene and its structural and electronic characterization by Scanning Tunneling Spectroscopy (STS) and Density Functional Theory (DFT).

8.1 Synthesis of an [18]annulene based PAH

Inspired by the strategy of Gottfried and coworkers [137, 138], we envisaged the preparation of planar nanographene structures consisting on a [18]annulene core from a dibromo polycyclic aromatic compound (Figure 8.1, **B**) by the formation of 3 C-C bonds by Ullmann coupling and 15 C-C bonds by intramolecular cyclodehydrogenation.

The reaction process has two steps (Figure 8.1): first, a sub-monolayer amount of precursor **B** was sublimated onto a clean Au(111) substrate from a Knudsen cell held at

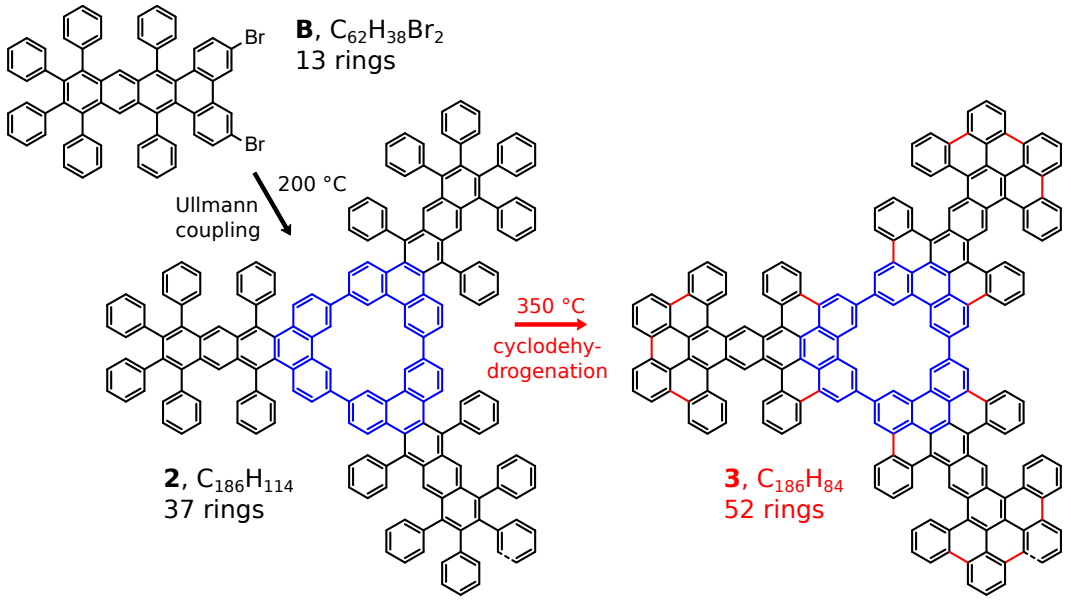

Figure 8.1: Reaction scheme to synthesize a PAH with [18]annulene core. Three monomers (**B**) join through Ullmann coupling creating non planar trimer structures ($C_{186}H_{114}$, **2**). The [18]annulene core, already synthesized at this reaction step, is highlighted in blue. Further annealing triggers the cyclodehydrogenations, which create 15 C-C bonds highlighted in red. The final trimer ($C_{186}H_{84}$, **3**) possesses C3 symmetry.

300 °C. During deposition, the metal sample was held at 200 °C to favor the Ulmann-coupling polymerization of the precursor upon their arrival to the surface, rather than their packing in more complex π-stacked ensembles. Still, STM inspection of the sample finds that the reacted monomers form closed-packed islands of different sizes and shapes (Figure 8.2a). Close-up views resolve polymeric structures of interconnected **1**-forms (inset of Figure 8.2a), among which, the centrosymmetric structure **2** in Figure 8.1 can be occasionally recognized. Similar to the case of monomer **A** in the previous chapter, the presence of small protrusions in **2** indicated that the molecules did not undergo a cyclodehydrogenation process at this temperature [139].

Upon further annealing of a precovered sample (as in Figure 8.2a) to temperatures around 375 °C, the packed molecular islands dissolve and transform into a disperse set of clusters of interconnected flat motifs (Figure 8.2b). The flat appearance of the motif suggests that the majority of the polymers underwent a substrate-induced cyclodehydrogenation, which fused all their phenylenes into a planar carbon structure (a very few amount of unreacted structures can still be distinguished). These new structures favor the interaction with the metal surface against intermolecular π-stacking and, consequently, appear arranged in small disperse structures rather than in packed molecular islands.

A fraction of the reacted polymers correspond to trimers with a structure resembling model **3** depicted in Figure 8.1: three planar motifs surrounding a central pore, forming a planar carbon structure with C3-symmetry. However, a closer inspection reveals that the shape of these trimers does not strictly correspond to compound's **3** structure. All

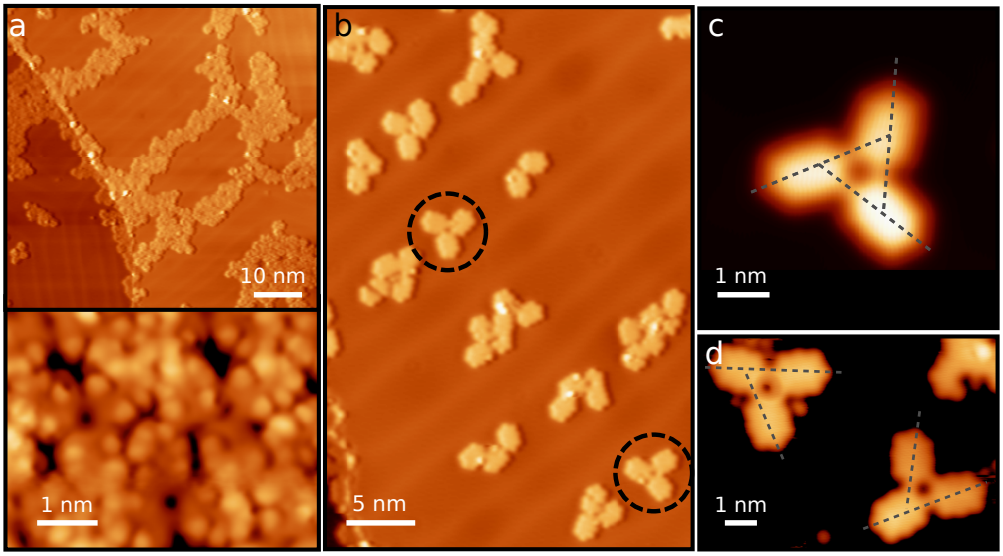

Figure 8.2: (a) Large scale STM topography image of the reacted monomers, arranged in heterogeneous π-stacked islands. Inset shows a small scale STM topography. Each individual monomer subunit can be identified, the protusions coinciding with the positions of phenyl rings project outwards in **2** (V_s=0.6 V I_t=120 pA). (b) Large scale STM topography image of the cyclodehydrogenated phase, characterized by the small disperse arrengements of molecules. Dashed circles highlight trimer structures (V_s=1 V I_t=290 pA). (c) Small scale constant height image of a C3 symmetric trimer, the three lobes share the same relative directionality (gray dashed lines) (V_s=1.2 V Z_{off}=-1.8 Å , OFC: V_s=1.2 V I_t=500 pA)(d) Small scale topography image of two asymmetric chiral enantiomers. Two of the lobes share a common axis, joining their central outward protusion through their connecting bond (grey dashed lines). The third lobe does not display such directionality with the other two lobes (V_s=1 V I_t=290 pA).

trimers show a faint helical shape endowed by the small bend of all three lobes in the same relative orientation with respect to the pore (Figure 8.2c). Additionally, we observe other trimers even deviating from the C3-symmetric forms, in which one of the lobes bends opposite to the other two lobes (Figure 8.2d). The observation of these unexpected shapes suggests that additional cyclization processes occur during the reaction.

8.2 Planarization via benzoazulene formation

To find out the origin of the twisted shapes, we resolved the intramolecular structure of the trimers with high-resolution STM images using a CO-functionalized tip (see chapter 1.2). Figure 8.3a, shows a constant height dI/dV map of a C3-trimer, resolving with high detail its intramolecular ring structure. Each of the three planar motifs is composed of 21 rings instead of the expected 17 rings in **3**. Hence, the resulting trimers (**4** and **5** in Figure 8.3a and c) possess in total 64 carbon rings, 12 more than compound **3**. More importantly, two pairs of five and seven-membered rings, i.e. azulene, appear in each of the three lobes.

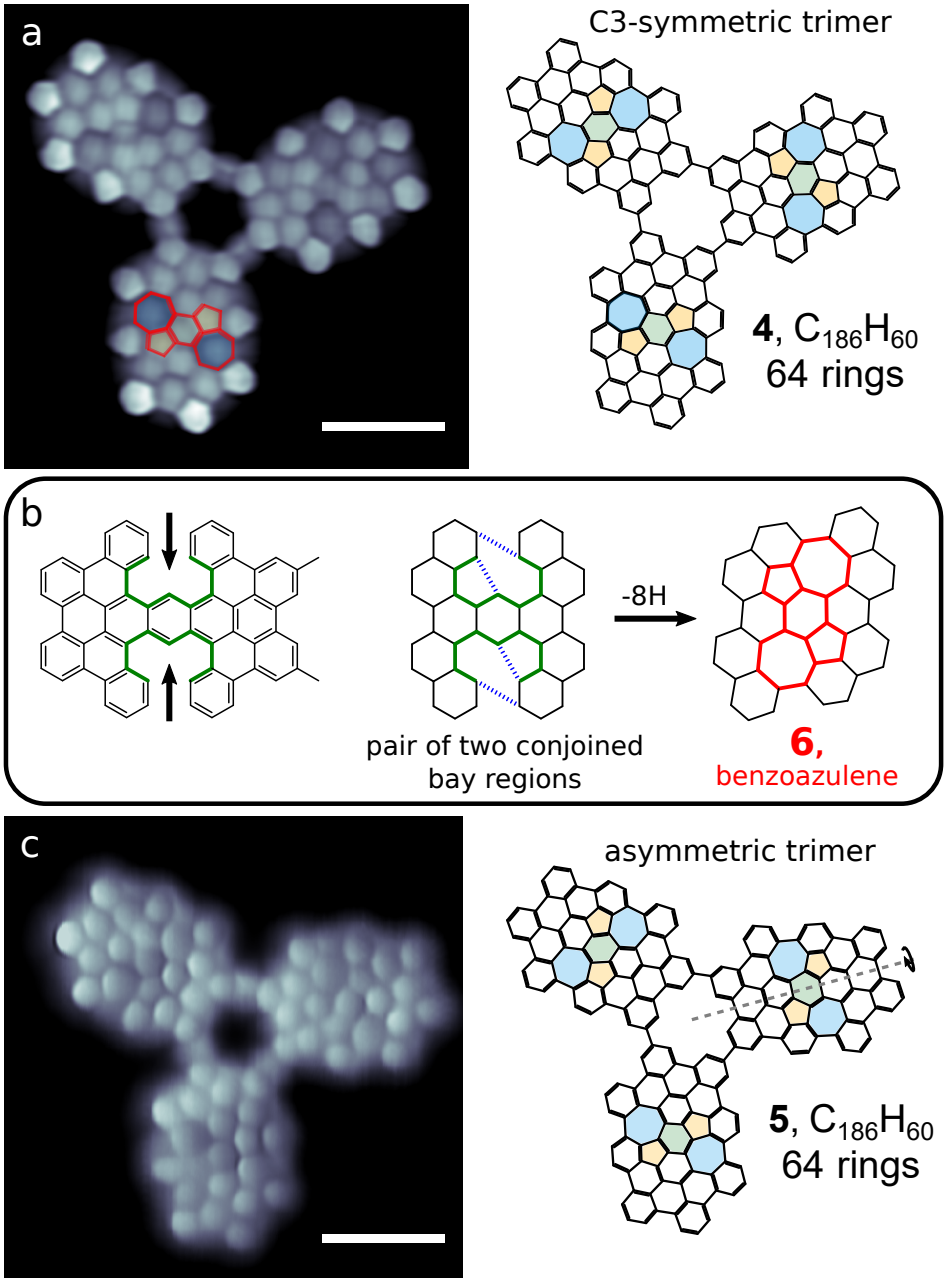

Figure 8.3: (a) Constant height dI/dV map with a CO functionalized tip of a C3-symmetric trimer. The intramolecular structure of the trimer is clearly identified. Each of the lobes possesses a benzoazulene group(**4** C20H12, highlighted in red). The chemical structure of compound **4** unambigously matches to the one revealed by the STM CO imaging. All benzoazulenes share the same orientation respect to the center of the trimer and as a result the trimer has a C3-symmetry (V_s=5 mV Z_{off}=-1.05 Å, V_{rms}= 10 mV, f=699.1 Hz, OFC: V_s=5 mV I_t=100p A). (b) Same as in panel *a*, but for an asymmetric trimer. The high resolution evidences the different orientation of one of the lobes (grey dashed lines) which is the cause of the asymmetry on the trimer (V_s=5 mV Z_{off}=-1.0 Å, V_{rms}= 10 mV, f=699.1 Hz, OFC: V_s=5 mV I_t=110 pA). Scale bars are 1 nm.

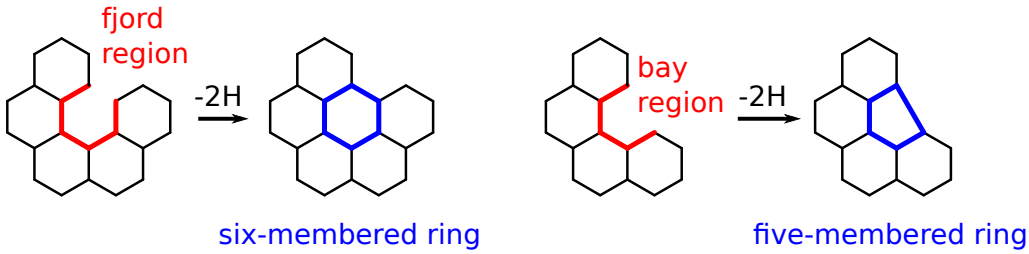

Figure 8.4: Usual cyclization strategies to form: six-membered rings from a fjord region (left) and five-membered rings from bay regions.

These moieties origin from the cyclization of the conjoined bay regions in each cyclodehydrogenated trimer subunit (arrows in Figure 8.2b). In contrast with usual cyclizations in fjord or bay regions, leading to six or five-membered rings, the pairs of conjoined bay regions of our monomer lead to the formation of benzoazulene groups (**6**). This process reduces the steric hyndrance in each of the conjoined bay regions, where three hydrogen atoms overlap at each cavity. Five- and seven-member rings are typically regarded as defects in the graphene structure [133, 140–144] , and appear commonly at the connecting boundaries between two graphene sheets with different alignment [86]. They are also allotropic configurations of graphene, which partially maintain the sp^2 character of the carbon sheet [135, 136]. In the current case, the benzoazulene moieties appearing in the cores of each of the three planar motifs show a well-defined and repetitive configuration, which refrain us from calling them defects. We are not aware of previous synthesis strategies to produce these benzoazulene groups, which play a key role in planarizing our structures.

The benzoazulenes are also the origin of the asymmetric structure of the trimers. They show two possible (mirror-symmetric) orientations with respect to the axis of the carbon motif (the radius of the trimer), imposing the bending distortion apparent already in Figure 8.2c and d. Three equally oriented benzoazulene groups lead to the C3 symmetric trimers (Figure 8.2c and Figure 8.3a, **4**) while the reversed orientation of one of them induces asymmetric structures like in Figure 8.2d (Figure 8.3c, **5**). After STM inspection of the structure of 127 trimers, we found 100 trimers of the form **5** and the rest of the form **4**. The ratio of C3-symmetric vs. asymmetric species is close to the 1 to 3 proportion of possible configurations of each type. Therefore, the formation of benzoazulene in the core of each motif is probably independent of the orientation of benzoazulenes in the other motifs of the trimer, indicating a non cooperative reaction.

8.3 Electronic structure and pore states

The azulene groups inserted in the carbon motifs contribute to the stabilization of the extended aromatic system. We investigate their electronic structure by means of differential conductance (dI/dV) spectroscopy and imaging, exploring the extension of the frontier orbitals. Point spectra acquired over the molecules (Figure 8.5a) identify the HOMO and LUMO derived resonances as spectral features at -0.8 V and 1.2 V. Constant height maps of dI/dV measured at these bias values are shown in Figure 8.5b and 8.5c, respectively. The dI/dV images show a characteristic intramolecular

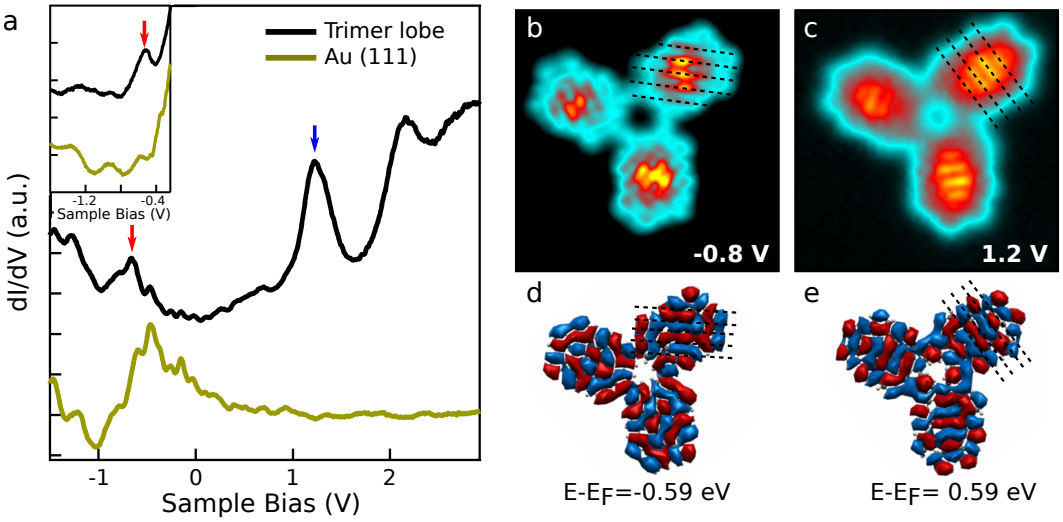

Figure 8.5: (a) dI/dV spectrum taken at the center of a lobe of a trimer (black curve), showing a strong feature at +1.2eV associated to the LUMO orbital of the molecule (blue arrow). The spectrum of the bare Au(111) substrate is shown as a reference (green curve, OFC: V_s=1 V, I_t=770 pA). Inset: constant current spectrum showing a well-marked peak at -0.8eV attributed to the HOMO orbitals of the trimer (red arrows, I_t=300 pA). (Lock-in parameters: V_{rms}= 10 mV, f=930 Hz.) (b) Constant height dI/dV of the HOMO level of a C3 symmetric trimer. The map is acquired with a CO functionalized tipm which allows to resolve the electronic features of the orbital, such as the modes highlighted with black dashed lines (V_s=0.8 V Z_{off}=0.0 Å, OFC: V_s=-0.8 V I_t=100 pA). (c) Same as in panel *b*, but for the LUMO level, at 1.2 V. The modes of the orbital are also observed and highlighted with dashed black lines (V_s=1.2 V Z_{off}=-0.4 Å, OFC: V_s=1.2 V I_t=100 pA). (d) Wavefunction of the HOMO level ($E - E_F$ = -0.59 eV) of a gas phase C3 symmetric trimer. The orientation and number of modes of the orbital (dashed black lines) shows remarkable agreement with the experimental map in panel *a*. (e) Same as in panel *d*, but for the LUMO level ($E - E_F$ = 0.59 eV). Again, both calculations and experimental data show very good agreement. (Lock-in parameters for dI/dV maps: V_{rms}= 10 mV, f=699.1 Hz).

pattern extending all around the carbon platform rather than localized in some parts or edges, supporting the conjugated character of these states. To interpret these maps, we compared them with DFT simulations of the density of states (DOS) of the HOMO (Figure 8.5d) and LUMO (Figure 8.5e) states for a fuly relaxed, planar C3-symmetric trimer in the gas phase. The simulations confirm that the dI/dV modulations in both cases are correlated with the lobes of the orbital wavefunction, which run as axial-wavefronts for the LUMO and tilted-waves for the HOMO. The asymmetric trimers show a very similar dI/dV maps for the LUMO, while the HOMO shows a mirror symmetric wave-pattern in the miss-oriented lobe.

Remarkably, a highly localized conductance feature emerges at the center of the [18]annulene core at high biases. Constant current spectroscopy reveals a series of resonances between 1.8 V and 2.8 V (Figure 8.6a). Constant height dI/dV maps reveal that the state is first localized at the trimer pore, with very little DOS weight in the

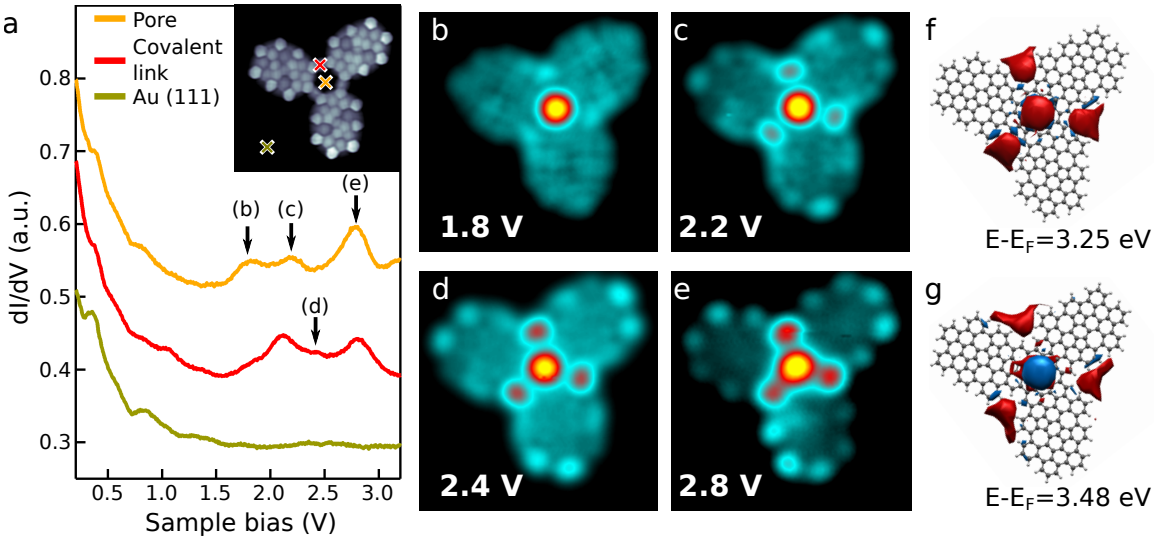

Figure 8.6: (a) Constant current spectra taken at the positions marked with crosses in the inset. At the center of the pore (orange spectra) we observe resonances at 1.8 V, 2.2 V and 2.8 V. On top of the covalent links we observe two broad resonances at 2.1 V and 2.8 V (I_t=300 pA, Lock-in parameters: V_{rms}= 10 mV, f=930 Hz). (b-e) Constant height dI/dV maps at the energies highlighted in panel *a*. At lower biases (b) the state is localized at the pore, with faint features in the outward cavities. As the bias is increased (c-e), the weight of these cavities is also increased. (f) Wavefunction of the lowest energy pore state ($E - E_F$ = 3.25 eV). The wavefunction sign of all cavities is the same. (g) Same as in *f* but for the highest energy pore state ($E - E_F$ = 3.48 eV). In this case the wavefuntion sign in the three outward cavities is opposite to the central pore. The clear resemblance between panel *c-e* and the calculations allows the identification of the pore state. (Z_{off}(b-e)=-0.4 Å, OFC: (b-e) I_t=71 pA), V_s= 1.8 V (b), 2.2 V (c), 2.4 V (d), 2.8 V (e), V_{rms}= 10 mV, f=699.1 Hz).

rest of the carbon platform (Figure 8.6b). As the bias is increased, the state develops a peculiar three fold shape, with weight in the three cavities at the joints between monomers (Figure 8.6c-e). Pore-localized states in non-covalent molecular architectures on surfaces have been detected due to the confinement of surface electrons [18,145–147]. The [18]annulene core is, on the contrary, a rigid structure arising from covalently bonded precursors, and the pore is the smallest possible in graphene, as it basically consists on a missing phenyl ring. Our DFT calculations on the free species find two states that reproduce with high precision the shape of the dI/dV maps, including three smaller maxima at each of the three outward cavities (Figure 8.6f and g). Thus, the observed experimental states are orbitals of the trimer structure, instead of confined surface electrons, and can probably be depicted as a symmetry-adapted overlap of specific motif orbitals.

Interestingly, we find that these states belong to the family of the so-called super-atom molecular orbitals (SAMOs, [149]). These states represent a set of high-lying unoccupied orbitals that extend far from the atomic nuclei. If we describe the potential of the carbon layer as a combination of Coulomb short-range exchange-correlations and long-range polarization interactions, SAMOs correspond to states with principal

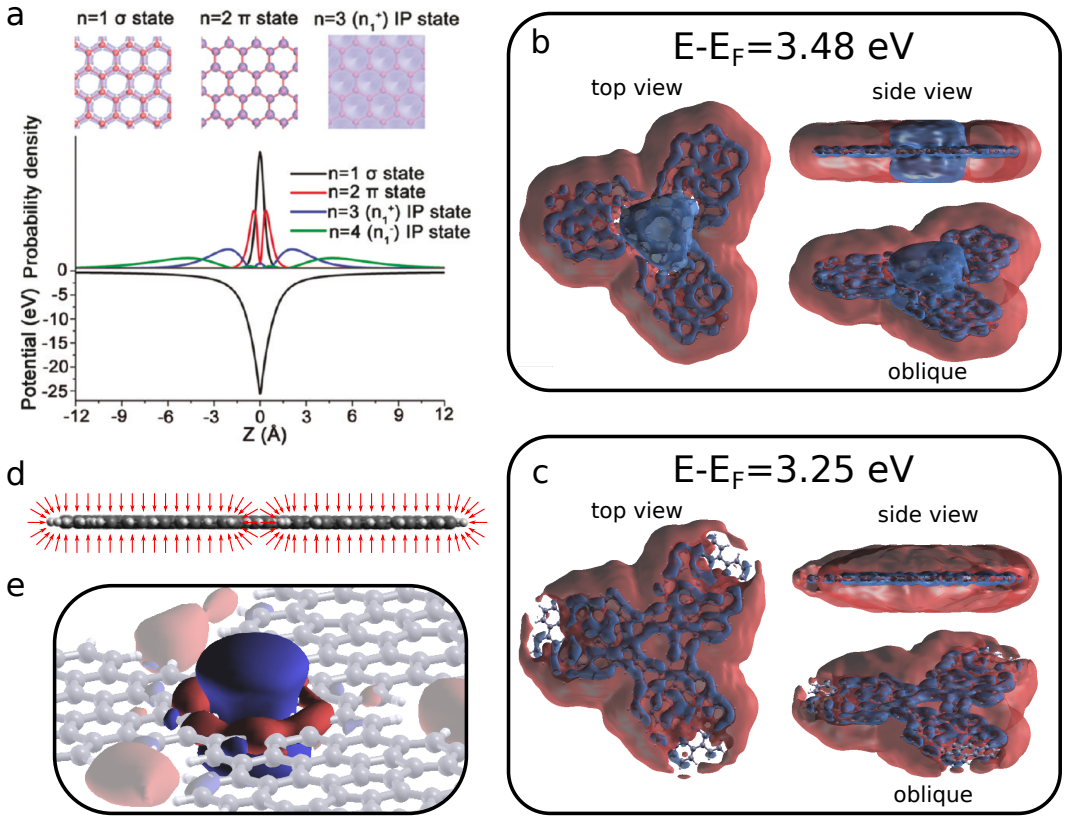

Figure 8.7: (a) Effective surface-normal potential and the corresponding calculated probability densities of n=1-4 states of graphene. Top panels show the top views of the n=1-3 state probabilities at the Γ point. Extracted from [148].(b) Wavefunction of the orbital shown in Figure 8.6g, at a smaller isovalue of 0.001. The SAMO displays weight in the vacuum region surrounding the carbon structure (red) and on top of the carbon network (blue). At the central pore, the n=3 contributions of the [18]annulene core add up shaping the orbital at the pore with a opposite sign (blue). (c) Same as in *b*, but for the SAMO shown in Figure 8.6f. In this case the vacuum components of the orbital share the same sign inside and outside the pore and as a result they merge all over the trimer. (d) Sketch representing the surface-normal potential over the plane of the trimer. The direction shifts upon reaching the edges of the trimer and its central pore. As a result, we expect a strong overlap in the small cavities and central pores, giving rise to the orbitals shown in panels *b* and *c*. (e) Close up view of the central pore in orbital in panel *b* at a higher isovalue (0.02). We observe a ring (red) enclosing the vacuum component of the orbital, suggesting the presence of n=3 orbital components in the trimer in plane direction.

quantum number $n \geqslant 3$ [150]. Figure 8.7a depicts this potential for graphene, projected along direction normal to the graphene surface. n=1 states (corresponding to σ orbitals, black) have their wavefunction amplitude concentrated close to the atomic positions and n=2 states (corresponding to the molecular π orbitals, red) posses a node at the atomic positions with two maxima above and below them. n=3 states (blue) have two nodes situated close to the π orbitals maxima, posses some weight close to the atomic positions and their amplitude extends well outside the molecular backbone.

SAMOs were first detected in C_{60} molecules, where the contributions of n=3 states overlap at the center of the molecule due to its three dimensional structure, resulting in well defined resonances at the hollow C_{60} core [149]. The pore states reported here have the same origin but for a two dimensional (flat) conjugated carbon platform. SAMOs are the molecular analog of Rydberg states [14] of free atoms or image states of metal surfaces. They have the peculiarity of corresponding to unoccupied electron states weakly bound to the almost completely screened atomic/molecular core, and they extend far into vacuum. Thus, they are prone to occupy cavities in the electrostatic potential landscape created by a molecule. As seen in Figure 8.7b and c, the pore state in Figure 8.6g consists in a cloud extended far away of the carbon platform (red). Following the sign of the wavefunction amplitude (color in Figure 8.7b and c), these states are even with respect to the plane of the carbon structure and, thus, are characterized by two nodal planes above and below the platform, consistent with the with the n=3 nature of the states. The remarkable difference between our monomer and the graphene sheet in Figure 8.7a, is the presence of edges. At the edges of our monomer, the atomic radial potential deviates from being out of plane to in plane (respect to the carbon sheet, Figure 8.7d), an thus the vacuum components of the SAMO surround the the whole trimer (Figure 8.7b and c). This is particularly relevant at the central pore and small outward cavities, where SAMO contributions overlap in the same position, giving rise to a well defined resonance, similar to the case of the C_{60} core [150]. Moreover, at smaller orbital isovalues, we observe the presence of orbital weight in the [18]Annulene core, consistent with the presence of a SAMO state extending towards the cavities (Figure 8.7e).

8.4 Conclusions

In conclusion, we have shown the on-surface synthesis of a unique large nanographene molecule, with the remarkable formation of three benzoazulene groups at its core. The catalytic properties of the surface allow the creation of these groups, which provide the trimers their chiral and planar conformation. Our work highlights additional reaction pathways allowed by the on-surface synthesis that can be exploited by clever precursor design, opening new possibilities in the growth of graphene-like structures.

The results presented in this chapter also allow us to understand the defect-like structures observed in the decorated chevron ribbons of chapter 7. Since both used monomers are isomers, it is highly probable that both can undergo the same additional cyclization processes.

Additionally, the [18]Annulene core formed by the trimers displays clearly defined SAMOs at the pores and cavities of the trimer. In contrast to SAMOs appearing in hollow three dimensional structures, such as C60 or nanotubes, the pore states reported here origin in a finite 2D structure.

Chapter 9

Conclusions and Outlooks

This thesis has presented the study of the electronic properties of GNRs grown by on-surface synthesis. This synthesis process allowed growing pristine 7-AGNRs, CN functionalized 7-AGNRs, boron substituted 7-AGNRs and hybrid 7-AGNRs; with atomic precision. We have structurally characterized the majority of these ribbons down to the atomic scale by LT-STM using CO-functionalized tips. Most importantly, by means of STS and DFT calculations, we have provided a description of their electronic structure and the underlying physics behind new properties that arise from the chemical modificaton of GNRs.

The study of 7-AGNR modified by edge CN groups showed a case study on the use of chemical moieties to alter the properties of GNRs by using functional groups instead of substitutional heteroatoms. Nitrile edge groups act as very efficient n-dopants, significantly downshifting the bands of 7-AGNRs. The charge redistribution induced by the CN groups creates an electrostatic background on the ribbon backbone, increasing its electronegativity.

Using functional groups in GNRs is a promising tool to precisely tune the physical and also chemical properties of GNRs. Given that the observed n-like doping in CN modified ribbons is driven by the dipolar moment and electron withdrawing properties of CN groups, using polar electron donor groups could induce the opposite behavior and p dope the ribbon. An interesting possibility is NH_2, which behaves as an electron donor in benzenoid rings. Moreover, its nitrogen lone pair is delocalized in these compounds, which could translate to in gap states in the ribbon. Functional groups could be used to bring additional properties to GNRs, such as additional reaction centers or optically active nodes. This work has to necessarily be paired with strategies to protect these groups during the on-surface reaction steps.

The analysis of boron substituted 7-AGNRs reported a more complete picture of the electronic structure of borylated 7-AGNRs. In particular, we addressed the lack of information concerning the valence band of these ribbons. The highlight of this research is, however, the importance of substrate-ribbon interactions, even on Au(111) supported GNRs. The higher interaction between boron and gold derives into corrugated ribbons and triggers the hybridization of the boron induced acceptor band with the surface.

Our work suggests that the introduction of heteroatoms in the ribbon backbone has further implications than the predicted electronic changes. For example, following

the hints provided by our ARPES measurments, borylated nanoribbons might become strained by choosing more reactive substrates with adequate lattice parameters. The increased interaction between the substrate and chemically modified ribbons is particularly important if the GNRs are to be transferred onto more reactive substrates. The use of insulators or other non noble metals might result in substantial ribbon-substrate hybridizations impacting the GNR's electronic properties.

The research on hybrid 7-AGNRs showcased the embedding of quantum dots within these heterostructures. The quantum wells originated from the merely substitution of a pair of carbon atoms by a pair of boron atoms. The boron pairs act as very efficient scatterers, confining the valence band of 7-AGNRs. Moreover, our results highlighted that this confinement was selective: while VB electrons were confined, their VB-1 counterparts were able to traverse the boron barriers unaffected. This results portray AGNRs as attractive systems for future electronic devices.

Selective band confinement presents new opportunities for embedding functional devices in GNRs. In this regard, future work considering different impurity number, nature or lattice position would provide further understanding in the band confinement selectivity. Additionally, electron transport measurements on hybrid ribbons supported between tip and sample would offer a unique experiment for demonstrating the band selective transport through QWs between boron pairs.

Finally, we have discovered a new on-surface strategy to planarize large polycyclic aromatic hydrocarbons (PAHs). Benzoazulene moieties were synthesized as a result of using a molecular precursor presenting conjoined bay regions. This new route may proof useful to create strained nanographenes or even create localized spins in the form of radicals, due to aromaticity constraints, within these structures. Moreover, the presence of super atom molecular orbitals (SAMOs) in the core of our [18]annulene core opens new possibilities concerning porous graphene, such as the potential coupling of SAMOs between adjacent pores. In this regard, using a regular porous lattice, similar to the one created by cyclohexa-*m*-phenylene [66], would provide the perfect framework to answer these questions.

In conclusion, our work has improved the overall knowledge on the electronic properties of GNRs and, in particular, chemically modified AGNRs. This knowledge has been gained hand in hand with the exploration of novel molecular precursors and new on-surface chemistry strategies.

Bibliography

[1] N. Savage, "Materials science: Super carbon," *Nature*, vol. 483, no. 7389, pp. S30–S31, 2012.

[2] K. Wakabayashi, K.-i. Sasaki, T. Nakanishi, and T. Enoki, "Electronic states of graphene nanoribbons and analytical solutions," *Science and Technology of Advanced Materials*, vol. 11, p. 054504, Oct. 2010.

[3] C. Stampfer, J. Güttinger, S. Hellmüller, F. Molitor, K. Ensslin, and T. Ihn, "Energy Gaps in Etched Graphene Nanoribbons," *Physical Review Letters*, vol. 102, p. 056403, Feb. 2009.

[4] D. Querlioz, Y. Apertet, A. Valentin, K. Huet, A. Bournel, S. Galdin-Retailleau, and P. Dollfus, "Suppression of the orientation effects on bandgap in graphene nanoribbons in the presence of edge disorder," *Applied Physics Letters*, vol. 92, p. 042108, Jan. 2008.

[5] J. Cai, P. Ruffieux, R. Jaafar, M. Bieri, T. Braun, S. Blankenburg, M. Muoth, A. P. Seitsonen, M. Saleh, X. Feng, K. Müllen, and R. Fasel, "Atomically precise bottom-up fabrication of graphene nanoribbons," *Nature*, vol. 466, pp. 470–473, July 2010.

[6] J. Cai, C. A. Pignedoli, L. Talirz, P. Ruffieux, H. Söde, L. Liang, V. Meunier, R. Berger, R. Li, X. Feng, K. Müllen, and R. Fasel, "Graphene nanoribbon heterojunctions," *Nature Nanotechnology*, vol. 9, pp. 896–900, Sept. 2014.

[7] Y.-C. Chen, T. Cao, C. Chen, Z. Pedramrazi, D. Haberer, D. G. de Oteyza, F. R. Fischer, S. G. Louie, and M. F. Crommie, "Molecular bandgap engineering of bottom-up synthesized graphene nanoribbon heterojunctions," *Nature Nanotechnology*, vol. 10, pp. 156–160, Jan. 2015.

[8] E. Carbonell-Sanromà, P. Brandimarte, R. Balog, M. Corso, S. Kawai, A. Garcia-Lekue, S. Saito, S. Yamaguchi, E. Meyer, D. Sánchez-Portal, and J. I. Pascual, "Quantum Dots Embedded in Graphene Nanoribbons by Chemical Substitution," *Nano Letters*, vol. 17, pp. 50–56, Jan. 2017.

[9] G. Binnig, H. Rohrer, C. Gerber, and E. Weibel, "Tunneling through a controllable vacuum gap," *Applied Physics Letters*, vol. 40, pp. 178–180, Jan. 1982.

[10] G. Binnig, H. Rohrer, C. Gerber, and E. Weibel, "7×7 reconstruction on Si (111) resolved in real space," *Physical Review Letters*, vol. 50, no. 2, p. 120, 1983.

[11] D. M. Eigler and E. K. Schweizer, "Positioning single atoms with a scanning tunnelling microscope," *Nature*, vol. 344, pp. 524–526, Apr. 1990.

[12] R. Feynman, R. Leighton, and M. Sands, *The Feynman lectures on physics. Vol. 3: Quantum mechanics.*
Addison-Wesley Publishing Co., Inc., Reading, Mass.-London, 1965.

[13] J. Bardeen, "Tunnelling from a Many-Particle Point of View," *Physical Review Letters*, vol. 6, pp. 57–59, Jan. 1961.

[14] C. Kittel, *Introduction to solid state physics.*
Hoboken, NJ: Wiley, 8th ed ed., 2005.

[15] J. Tersoff and D. R. Hamann, "Theory and Application for the Scanning Tunneling Microscope," *Physical Review Letters*, vol. 50, pp. 1998–2001, June 1983.

[16] J. Repp, G. Meyer, S. M. Stojković, A. Gourdon, and C. Joachim, "Molecules on Insulating Films: Scanning-Tunneling Microscopy Imaging of Individual Molecular Orbitals," *Physical Review Letters*, vol. 94, p. 026803, Jan. 2005.

[17] J. Li, W.-D. Schneider, and R. Berndt, "Local density of states from spectroscopic scanning-tunneling-microscope images: Ag (111)," *Physical Review B*, vol. 56, no. 12, p. 7656, 1997.

[18] W. Krenner, D. Kühne, F. Klappenberger, and J. V. Barth, "Assessment of Scanning Tunneling Spectroscopy Modes Inspecting Electron Confinement in Surface-Confined Supramolecular Networks," *Scientific Reports*, vol. 3, Dec. 2013.

[19] L. Gross, F. Mohn, N. Moll, P. Liljeroth, and G. Meyer, "The Chemical Structure of a Molecule Resolved by Atomic Force Microscopy," *Science*, vol. 325, pp. 1110–1114, Aug. 2009.

[20] N. D. Lang, "Spectroscopy of single atoms in the scanning tunneling microscope," *Physical Review B*, vol. 34, pp. 5947–5950, Oct. 1986.

[21] A. Selloni, P. Carnevali, E. Tosatti, and C. D. Chen, "Voltage-dependent scanning-tunneling microscopy of a crystal surface: Graphite," *Physical Review B*, vol. 31, pp. 2602–2605, Feb. 1985.

[22] L. Gross, N. Moll, F. Mohn, A. Curioni, G. Meyer, F. Hanke, and M. Persson, "High-Resolution Molecular Orbital Imaging Using a p -Wave STM Tip," *Physical Review Letters*, vol. 107, p. 086101, Aug. 2011.

[23] R. Temirov, S. Soubatch, O. Neucheva, A. C. Lassise, and F. S. Tautz, "A novel method achieving ultra-high geometrical resolution in scanning tunnelling microscopy," *New Journal of Physics*, vol. 10, p. 053012, May 2008.

[24] F. Giessibl, "Device for noncontact intermittent contact scanning of a surface and a process therefore," June 2001.
Patent US6240771 B1.

[25] N. Moll, L. Gross, F. Mohn, A. Curioni, and G. Meyer, "The mechanisms underlying the enhanced resolution of atomic force microscopy with functionalized tips," *New Journal of Physics*, vol. 12, p. 125020, Dec. 2010.

[26] J. A. Gupta, C. P. Lutz, A. J. Heinrich, and D. M. Eigler, "Strongly coverage-dependent excitations of adsorbed molecular hydrogen," *Physical Review B*, vol. 71, p. 115416, Mar. 2005.

[27] C. Weiss, C. Wagner, C. Kleimann, M. Rohlfing, F. S. Tautz, and R. Temirov, "Imaging Pauli Repulsion in Scanning Tunneling Microscopy," *Physical Review Letters*, vol. 105, p. 086103, Aug. 2010.

[28] S. Li, A. Yu, F. Toledo, Z. Han, H. Wang, H. Y. He, R. Wu, and W. Ho, "Rotational and Vibrational Excitations of a Hydrogen Molecule Trapped within a Nanocavity of Tunable Dimension," *Physical Review Letters*, vol. 111, p. 146102, Oct. 2013.

[29] F. D. Natterer, F. Patthey, and H. Brune, "Distinction of Nuclear Spin States with the Scanning Tunneling Microscope," *Physical Review Letters*, vol. 111, p. 175303, Oct. 2013.

[30] G. Kichin, C. Weiss, C. Wagner, F. S. Tautz, and R. Temirov, "Single Molecule and Single Atom Sensors for Atomic Resolution Imaging of Chemically Complex Surfaces," *Journal of the American Chemical Society*, vol. 133, pp. 16847–16851, Oct. 2011.

[31] P. Hapala, G. Kichin, C. Wagner, F. S. Tautz, R. Temirov, and P. Jelínek, "Mechanism of high-resolution STM/AFM imaging with functionalized tips," *Physical Review B*, vol. 90, p. 085421, Aug. 2014.

[32] P. Hapala, R. Temirov, F. S. Tautz, and P. Jelínek, "Origin of High-Resolution IETS-STM Images of Organic Molecules with Functionalized Tips," *Physical Review Letters*, vol. 113, p. 226101, Nov. 2014.

[33] K. Besocke, "An easily operable scanning tunneling microscope," *Surface Science*, vol. 181, pp. 145–153, Mar. 1987.

[34] I. Horcas, R. Fernández, J. M. Gómez-Rodríguez, J. Colchero, J. Gómez-Herrero, and A. M. Baro, "Wsxm: A software for scanning probe microscopy and a tool for nanotechnology," *Review of Scientific Instruments*, vol. 78, p. 013705, Jan. 2007.

[35] M. Corso, L. Fernández, F. Schiller, and J. E. Ortega, "Au(111)-Based Nanotemplates by Gd Alloying," *ACS Nano*, vol. 4, pp. 1603–1611, Mar. 2010.

[36] M. Baldoni, A. Sgamellotti, and F. Mercuri, "Electronic properties and stability of graphene nanoribbons: An interpretation based on Clar sextet theory," *Chemical Physics Letters*, vol. 464, pp. 202–207, Oct. 2008.

[37] T. Wassmann, A. P. Seitsonen, A. M. Saitta, M. Lazzeri, and F. Mauri, "Clar's Theory, π-Electron Distribution, and Geometry of Graphene Nanoribbons," *Journal of the American Chemical Society*, vol. 132, pp. 3440–3451, Mar. 2010.

[38] F. J. Martín-Martínez, S. Fias, G. Van Lier, F. De Proft, and P. Geerlings, "Electronic Structure and Aromaticity of Graphene Nanoribbons," *Chemistry - A European Journal*, vol. 18, pp. 6183–6194, May 2012.

[39] Y.-C. Chen, D. G. de Oteyza, Z. Pedramrazi, C. Chen, F. R. Fischer, and M. F. Crommie, "Tuning the Band Gap of Graphene Nanoribbons Synthesized from Molecular Precursors," *ACS Nano*, vol. 7, pp. 6123–6128, July 2013.

[40] A. Basagni, F. Sedona, C. A. Pignedoli, M. Cattelan, L. Nicolas, M. Casarin, and M. Sambi, "Molecules-Oligomers-Nanowires-Graphene Nanoribbons: A Bottom-Up Stepwise On-Surface Covalent Synthesis Preserving Long-Range Order," *Journal of the American Chemical Society*, vol. 137, pp. 1802–1808, Feb. 2015.

[41] J. Liu, B.-W. Li, Y.-Z. Tan, A. Giannakopoulos, C. Sanchez-Sanchez, D. Beljonne, P. Ruffieux, R. Fasel, X. Feng, and K. Müllen, "Toward Cove-Edged Low Band Gap Graphene Nanoribbons," *Journal of the American Chemical Society*, vol. 137, pp. 6097–6103, May 2015.

[42] A. Kimouche, M. M. Ervasti, R. Drost, S. Halonen, A. Harju, P. M. Joensuu, J. Sainio, and P. Liljeroth, "Ultra-narrow metallic armchair graphene nanoribbons," *Nature Communications*, vol. 6, p. 10177, Dec. 2015.

[43] P. Ruffieux, S. Wang, B. Yang, C. Sánchez-Sánchez, J. Liu, T. Dienel, L. Talirz, P. Shinde, C. A. Pignedoli, D. Passerone, T. Dumslaff, X. Feng, K. Müllen, and R. Fasel, "On-surface synthesis of graphene nanoribbons with zigzag edge topology," *Nature*, vol. 531, pp. 489–492, Mar. 2016.

[44] L. Talirz, H. Söde, T. Dumslaff, S. Wang, J. R. Sanchez-Valencia, J. Liu, P. Shinde, C. A. Pignedoli, L. Liang, V. Meunier, N. C. Plumb, M. Shi, X. Feng, A. Narita, K. Müllen, R. Fasel, and P. Ruffieux, "On-Surface Synthesis and Characterization of 9-Atom Wide Armchair Graphene Nanoribbons," *ACS Nano*, Feb. 2017.

[45] P. Ruffieux, J. Cai, N. C. Plumb, L. Patthey, D. Prezzi, A. Ferretti, E. Molinari, X. Feng, K. Müllen, C. A. Pignedoli, and R. Fasel, "Electronic Structure of Atomically Precise Graphene Nanoribbons," *ACS Nano*, vol. 6, pp. 6930–6935, Aug. 2012.

[46] H. Söde, L. Talirz, O. Gröning, C. A. Pignedoli, R. Berger, X. Feng, K. Müllen, R. Fasel, and P. Ruffieux, "Electronic band dispersion of graphene nanoribbons via Fourier-transformed scanning tunneling spectroscopy," *Physical Review B*, vol. 91, p. 045429, Jan. 2015.

[47] A. H. Castro Neto, F. Guinea, N. M. R. Peres, K. S. Novoselov, and A. K. Geim, "The electronic properties of graphene," *Reviews of Modern Physics*, vol. 81, pp. 109–162, Jan. 2009.

[48] P. R. Wallace, "The Band Theory of Graphite," *Physical Review*, vol. 71, pp. 622–634, May 1947.

[49] Y.-W. Son, M. L. Cohen, and S. G. Louie, "Energy Gaps in Graphene Nanoribbons," *Physical Review Letters*, vol. 97, p. 216803, Nov. 2006.

[50] L. Yang, C.-H. Park, Y.-W. Son, M. L. Cohen, and S. G. Louie, "Quasiparticle Energies and Band Gaps in Graphene Nanoribbons," *Physical Review Letters*, vol. 99, p. 186801, Nov. 2007.

[51] L. Liang and V. Meunier, "Electronic structure of assembled graphene nanoribbons: Substrate and many-body effects," *Physical Review B*, vol. 86, p. 195404, Nov. 2012.

[52] M. Fujita, K. Wakabayashi, K. Nakada, and K. Kusakabe, "Peculiar Localized State at Zigzag Graphite Edge," *Journal of the Physical Society of Japan*, vol. 65, pp. 1920–1923, July 1996.

[53] K. Nakada, M. Fujita, G. Dresselhaus, and M. S. Dresselhaus, "Edge state in graphene ribbons: Nanometer size effect and edge shape dependence," *Physical Review B*, vol. 54, no. 24, p. 17954, 1996.

[54] K. Wakabayashi, M. Fujita, H. Ajiki, and M. Sigrist, "Electronic and magnetic properties of nanographite ribbons," *Physical Review B*, vol. 59, no. 12, p. 8271, 1999.

[55] Y. Zhang, Y. Zhang, G. Li, J. Lu, X. Lin, S. Du, R. Berger, X. Feng, K. Müllen, and H.-J. Gao, "Direct visualization of atomically precise nitrogen-doped graphene nanoribbons," *Applied Physics Letters*, vol. 105, p. 023101, July 2014.

[56] E. Clar, *The aromatic sextet*.
J. Wiley, 1972.

[57] Z. B. Maksić, D. Barić, and T. Müller, "Clar's Sextet Rule Is a Consequence of the σ-Electron Framework," *The Journal of Physical Chemistry A*, vol. 110, pp. 10135–10147, Aug. 2006.

[58] I. Gutman, . Z. Tomović, K. Müllen, and J. P. Rabe, "On the distribution of π-electrons in large polycyclic aromatic hydrocarbons," *Chemical Physics Letters*, vol. 397, pp. 412–416, Oct. 2004.

[59] T. M. Krygowski and M. K. Cyranski, "Structural Aspects of Aromaticity," *Chemical Reviews*, vol. 101, pp. 1385–1420, May 2001.

[60] J. Campos-Delgado, J. M. Romo-Herrera, X. Jia, D. A. Cullen, H. Muramatsu, Y. A. Kim, T. Hayashi, Z. Ren, D. J. Smith, Y. Okuno, T. Ohba, H. Kanoh, K. Kaneko, M. Endo, H. Terrones, M. S. Dresselhaus, and M. Terrones, "Bulk Production of a New Form of sp^2 Carbon: Crystalline Graphene Nanoribbons," *Nano Letters*, vol. 8, pp. 2773–2778, Sept. 2008.

[61] X. Li, X. Wang, L. Zhang, S. Lee, and H. Dai, "Chemically Derived, Ultrasmooth Graphene Nanoribbon Semiconductors," *Science*, vol. 319, pp. 1229–1232, Feb. 2008.

[62] L. Tapasztó, G. Dobrik, P. Lambin, and L. P. Biró, "Tailoring the atomic structure of graphene nanoribbons by scanning tunnelling microscope lithography," *Nature Nanotechnology*, vol. 3, pp. 397–401, July 2008.

[63] D. V. Kosynkin, A. L. Higginbotham, A. Sinitskii, J. R. Lomeda, A. Dimiev, B. K. Price, and J. M. Tour, "Longitudinal unzipping of carbon nanotubes to form graphene nanoribbons," *Nature*, vol. 458, pp. 872–876, Apr. 2009.

[64] G. Vasseur, M. Abadia, L. A. Miccio, J. Brede, A. Garcia-Lekue, D. G. de Oteyza, C. Rogero, J. Lobo-Checa, and J. E. Ortega, "π Band Dispersion along Conjugated Organic Nanowires Synthesized on a Metal Oxide Semiconductor," *Journal of the American Chemical Society*, vol. 138, pp. 5685–5692, May 2016.

[65] F. Ullmann and J. Bielecki, "Ueber synthesen in der biphenylreihe," *European Journal of Inorganic Chemistry*, vol. 34, no. 2, pp. 2174–2185, 1901.

[66] M. Bieri, M.-T. Nguyen, O. Gröning, J. Cai, M. Treier, K. Aït-Mansour, P. Ruffieux, C. A. Pignedoli, D. Passerone, M. Kastler, K. Müllen, and R. Fasel, "Two-Dimensional Polymer Formation on Surfaces: Insight into the Roles of Precursor Mobility and Reactivity," *Journal of the American Chemical Society*, vol. 132, pp. 16669–16676, Nov. 2010.

[67] J. Björk, F. Hanke, and S. Stafström, "Mechanisms of Halogen-Based Covalent Self-Assembly on Metal Surfaces," *Journal of the American Chemical Society*, vol. 135, pp. 5768–5775, Apr. 2013.

[68] R. Gutzler, L. Cardenas, J. Lipton-Duffin, M. El Garah, L. E. Dinca, C. E. Szakacs, C. Fu, M. Gallagher, M. Vondráček, M. Rybachuk, D. F. Perepichka, and F. Rosei, "Ullmann-type coupling of brominated tetrathienoanthracene on copper and silver," *Nanoscale*, vol. 6, no. 5, p. 2660, 2014.

[69] K. A. Simonov, N. A. Vinogradov, A. S. Vinogradov, A. V. Generalov, E. M. Zagrebina, N. Mårtensson, A. A. Cafolla, T. Carpy, J. P. Cunniffe, and A. B. Preobrajenski, "Effect of Substrate Chemistry on the Bottom-Up Fabrication of Graphene Nanoribbons: Combined Core-Level Spectroscopy and STM Study," *The Journal of Physical Chemistry C*, vol. 118, pp. 12532–12540, June 2014.

[70] A. Batra, D. Cvetko, G. Kladnik, O. Adak, C. Cardoso, A. Ferretti, D. Prezzi, E. Molinari, A. Morgante, and L. Venkataraman, "Probing the mechanism for graphene nanoribbon formation on gold surfaces through X-ray spectroscopy," *Chem. Sci.*, vol. 5, pp. 4419–4423, July 2014.

[71] L. Massimi, O. Ourdjini, L. Lafferentz, M. Koch, L. Grill, E. Cavaliere, L. Gavioli, C. Cardoso, D. Prezzi, E. Molinari, A. Ferretti, C. Mariani, and M. G. Betti, "Surface-Assisted Reactions toward Formation of Graphene Nanoribbons on Au(110) Surface," *The Journal of Physical Chemistry C*, pp. 2427–2437, Jan. 2015.

[72] F. Schulz, P. H. Jacobse, F. F. Canova, J. van der Lit, D. Z. Gao, A. van den Hoogenband, P. Han, R. J. Klein Gebbink, M.-E. Moret, P. M. Joensuu, I. Swart, and P. Liljeroth, "Precursor Geometry Determines the Growth Mechanism in Graphene Nanoribbons," *The Journal of Physical Chemistry C*, Jan. 2017.

[73] D. G. de Oteyza, A. García-Lekue, M. Vilas-Varela, N. Merino-Díez, E. Carbonell-Sanromà, M. Corso, G. Vasseur, C. Rogero, E. Guitián, J. I. Pascual, J. E. Ortega, Y. Wakayama, and D. Peña, "Substrate-Independent Growth of Atomically Precise Chiral Graphene Nanoribbons," *ACS Nano*, vol. 10, pp. 9000–9008, Sept. 2016.

[74] J. A. Lipton-Duffin, O. Ivasenko, D. F. Perepichka, and F. Rosei, "Synthesis of Polyphenylene Molecular Wires by Surface-Confined Polymerization," *Small*, vol. 5, pp. 592–597, Mar. 2009.

[75] H. Zhang, H. Lin, K. Sun, L. Chen, Y. Zagranyarski, N. Aghdassi, S. Duhm, Q. Li, D. Zhong, Y. Li, K. Müllen, H. Fuchs, and L. Chi, "On-Surface Synthesis of Rylene-Type Graphene Nanoribbons," *Journal of the American Chemical Society*, vol. 137, pp. 4022–4025, Apr. 2015.

[76] J. Björk, S. Stafström, and F. Hanke, "Zipping up: cooperativity drives the synthesis of graphene nanoribbons," *Journal of the American Chemical Society*, vol. 133, no. 38, pp. 14884–14887, 2011.

[77] H. Huang, D. Wei, J. Sun, S. L. Wong, Y. P. Feng, A. H. C. Neto, and A. T. S. Wee, "Spatially Resolved Electronic Structures of Atomically Precise Armchair Graphene Nanoribbons," *Scientific Reports*, vol. 2, Dec. 2012.

[78] J. van der Lit, M. P. Boneschanscher, D. Vanmaekelbergh, M. Ijäs, A. Uppstu, M. Ervasti, A. Harju, P. Liljeroth, and I. Swart, "Suppression of electron-vibron coupling in graphene nanoribbons contacted via a single atom," *Nature Communications*, vol. 4, June 2013.

[79] J. van der Lit, P. H. Jacobse, D. Vanmaekelbergh, and I. Swart, "Bending and buckling of narrow armchair graphene nanoribbons via STM manipulation," *New Journal of Physics*, vol. 17, p. 053013, May 2015.

[80] S. Wang, L. Talirz, C. A. Pignedoli, X. Feng, K. Müllen, R. Fasel, and P. Ruffieux, "Giant edge state splitting at atomically precise graphene zigzag edges," *Nature Communications*, vol. 7, p. 11507, May 2016.

[81] M. Ijäs, M. Ervasti, A. Uppstu, P. Liljeroth, J. van der Lit, I. Swart, and A. Harju, "Electronic states in finite graphene nanoribbons: Effect of charging and defects," *Physical Review B*, vol. 88, p. 075429, Aug. 2013.

[82] S. Linden, D. Zhong, A. Timmer, N. Aghdassi, J. H. Franke, H. Zhang, X. Feng, K. Müllen, H. Fuchs, L. Chi, and H. Zacharias, "Electronic Structure of Spatially Aligned Graphene Nanoribbons on Au(788)," *Physical Review Letters*, vol. 108, p. 216801, May 2012.

[83] C. Bronner, F. Leyssner, S. Stremlau, M. Utecht, P. Saalfrank, T. Klamroth, and P. Tegeder, "Electronic structure of a subnanometer wide bottom-up fabricated graphene nanoribbon: End states, band gap, and dispersion," *Physical Review B*, vol. 86, p. 085444, Aug. 2012.

[84] C. Bronner, M. Utecht, A. Haase, P. Saalfrank, T. Klamroth, and P. Tegeder, "Electronic structure changes during the surface-assisted formation of a graphene nanoribbon," *The Journal of Chemical Physics*, vol. 140, p. 024701, Jan. 2014.

[85] R. Denk, M. Hohage, P. Zeppenfeld, J. Cai, C. A. Pignedoli, H. Söde, R. Fasel, X. Feng, K. Müllen, S. Wang, D. Prezzi, A. Ferretti, A. Ruini, E. Molinari, and P. Ruffieux, "Exciton-dominated optical response of ultra-narrow graphene nanoribbons," *Nature Communications*, vol. 5, July 2014.

[86] T. Dienel, S. Kawai, H. Söde, X. Feng, K. Müllen, P. Ruffieux, R. Fasel, and O. Gröning, "Resolving Atomic Connectivity in Graphene Nanostructure Junctions," *Nano Letters*, vol. 15, pp. 5185–5190, Aug. 2015.

[87] A. Shiotari, T. Kumagai, and M. Wolf, "Tip-Enhanced Raman Spectroscopy of Graphene Nanoribbons on Au(111)," *The Journal of Physical Chemistry C*, vol. 118, pp. 11806–11812, June 2014.

[88] L. Talirz, H. Söde, J. Cai, P. Ruffieux, S. Blankenburg, R. Jafaar, R. Berger, X. Feng, K. Müllen, D. Passerone, R. Fasel, and C. A. Pignedoli, "Termini of Bottom-Up Fabricated Graphene Nanoribbons," *Journal of the American Chemical Society*, vol. 135, pp. 2060–2063, Feb. 2013.

[89] C. Bronner, J. Björk, and P. Tegeder, "Tracking and Removing Br during the On-Surface Synthesis of a Graphene Nanoribbon," *The Journal of Physical Chemistry C*, vol. 119, pp. 486–493, Jan. 2015.

[90] M. Koch, F. Ample, C. Joachim, and L. Grill, "Voltage-dependent conductance of a single graphene nanoribbon," *Nature Nanotechnology*, vol. 7, pp. 713–717, Oct. 2012.

[91] S. Kawai, A. Benassi, E. Gnecco, H. Söde, R. Pawlak, X. Feng, K. Müllen, D. Passerone, C. A. Pignedoli, P. Ruffieux, R. Fasel, and E. Meyer, "Superlubricity of graphene nanoribbons on gold surfaces," *Science*, vol. 351, no. 6276, pp. 957–961, 2016.

[92] Z. Yang, M. Corso, R. Robles, C. Lotze, R. Fitzner, E. Mena-Osteritz, P. Bäuerle, K. J. Franke, and J. I. Pascual, "Orbital Redistribution in Molecular Nanostructures Mediated by Metal-Organic Bonds," *ACS Nano*, vol. 8, pp. 10715–10722, Oct. 2014.

[93] N. Kocić, X. Liu, S. Chen, S. Decurtins, O. Krejčí, P. Jelínek, J. Repp, and S.-X. Liu, "Control of Reactivity and Regioselectivity for On-Surface Dehydrogenative Aryl-Aryl Bond Formation," *Journal of the American Chemical Society*, vol. 138, pp. 5585–5593, May 2016.

[94] J. B. Neaton, M. S. Hybertsen, and S. G. Louie, "Renormalization of Molecular Electronic Levels at Metal-Molecule Interfaces," *Physical Review Letters*, vol. 97, p. 216405, Nov. 2006.

[95] K. S. Thygesen and A. Rubio, "Renormalization of Molecular Quasiparticle Levels at Metal-Molecule Interfaces: Trends across Binding Regimes," *Physical Review Letters*, vol. 102, p. 046802, Jan. 2009.

[96] W. Chen, V. Madhavan, T. Jamneala, and M. F. Crommie, "Scanning tunneling microscopy observation of an electronic superlattice at the surface of clean gold," *Physical Review Letters*, vol. 80, no. 7, p. 1469, 1998.

[97] J.-Y. Park, U. D. Ham, S.-J. Kahng, Y. Kuk, K. Miyake, K. Hata, and H. Shigekawa, "Modification of surface-state dispersion upon Xe adsorption: A scanning tunneling microscope study," *Physical review B*, vol. 62, no. 24, p. R16341, 2000.

[98] T. Andreev, I. Barke, and H. Hövel, "Adsorbed rare-gas layers on Au(111): Shift of the Shockley surface state studied with ultraviolet photoelectron spectroscopy and scanning tunneling spectroscopy," *Physical Review B*, vol. 70, p. 205426, Nov. 2004.

[99] N. Nicoara, E. Román, J. M. Gómez-Rodríguez, J. A. Martín-Gago, and J. Méndez, "Scanning tunneling and photoemission spectroscopies at the PTCDA/Au(111) interface," *Organic Electronics*, vol. 7, pp. 287–294, Oct. 2006.

[100] D. Malterre, B. Kierren, Y. Fagot-Revurat, S. Pons, A. Tejeda, C. Didiot, H. Cercellier, and A. Bendounan, "ARPES and STS investigation of Shockley states in thin metallic films and periodic nanostructures," *New Journal of Physics*, vol. 9, pp. 391–391, Oct. 2007.

[101] M. Golor, C. Koop, T. C. Lang, S. Wessel, and M. J. Schmidt, "Magnetic Correlations in Short and Narrow Graphene Armchair Nanoribbons," *Physical Review Letters*, vol. 111, p. 085504, Aug. 2013.

[102] C. Bronner, S. Stremlau, M. Gille, F. Braußе, A. Haase, S. Hecht, and P. Tegeder, "Aligning the Band Gap of Graphene Nanoribbons by Monomer Doping," *Angewandte Chemie International Edition*, vol. 52, pp. 4422–4425, Apr. 2013.

[103] G. D. Nguyen, F. M. Toma, T. Cao, Z. Pedramrazi, C. Chen, D. J. Rizzo, T. Joshi, C. Bronner, Y.-C. Chen, M. Favaro, S. G. Louie, F. R. Fischer, and M. F. Crommie, "Bottom-Up Synthesis of $N = 13$ Sulfur-Doped Graphene Nanoribbons," *The Journal of Physical Chemistry C*, vol. 120, pp. 2684–2687, Feb. 2016.

[104] S. Kawai, S. Saito, S. Osumi, S. Yamaguchi, A. S. Foster, P. Spijker, and E. Meyer, "Atomically controlled substitutional boron-doping of graphene nanoribbons," *Nature Communications*, vol. 6, p. 8098, Aug. 2015.

[105] R. R. Cloke, T. Marangoni, G. D. Nguyen, T. Joshi, D. J. Rizzo, C. Bronner, T. Cao, S. G. Louie, M. F. Crommie, and F. R. Fischer, "Site-Specific Substitutional Boron Doping of Semiconducting Armchair Graphene Nanoribbons," *Journal of the American Chemical Society*, vol. 137, pp. 8872–8875, July 2015.

[106] C. Sanchez-Sanchez, N. Orozco, J. P. Holgado, S. K. Beaumont, G. Kyriakou, D. J. Watson, A. R. Gonzalez-Elipe, L. Feria, J. Fernández Sanz, and R. M. Lambert, "Sonogashira Cross-Coupling and Homocoupling on a Silver Surface: Chlorobenzene and Phenylacetylene on Ag(100)," *Journal of the American Chemical Society*, vol. 137, pp. 940–947, Jan. 2015.

[107] H.-Y. Gao, J.-H. Franke, H. Wagner, D. Zhong, P.-A. Held, A. Studer, and H. Fuchs, "Effect of Metal Surfaces in On-Surface Glaser Coupling," *The Journal of Physical Chemistry C*, vol. 117, pp. 18595–18602, Sept. 2013.

[108] M. C. Chong, G. Reecht, H. Bulou, A. Boeglin, F. Scheurer, F. Mathevet, and G. Schull, "Narrow-Line Single-Molecule Transducer between Electronic Circuits and Surface Plasmons," *Physical Review Letters*, vol. 116, p. 036802, Jan. 2016.

[109] M. C. Chong, L. Sosa-Vargas, H. Bulou, A. Boeglin, F. Scheurer, F. Mathevet, and G. Schull, "Ordinary and Hot Electroluminescence from Single-Molecule Devices: Controlling the Emission Color by Chemical Engineering," *Nano Letters*, vol. 16, pp. 6480–6484, Oct. 2016.

[110] S. K. Hämäläinen, N. van der Heijden, J. van der Lit, S. den Hartog, P. Liljeroth, and I. Swart, "Intermolecular Contrast in Atomic Force Microscopy Images without Intermolecular Bonds," *Physical Review Letters*, vol. 113, p. 186102, Oct. 2014.

[111] L. Zhang, G. Y. Ang, and S. Chiba, "Copper-Catalyzed Synthesis of Phenanthridine Derivatives under an Oxygen Atmosphere Starting from Biaryl-2-carbonitriles and Grignard Reagents," *Organic Letters*, vol. 12, pp. 3682–3685, Aug. 2010.

[112] F. Cervantes-Sodi, G. Csányi, S. Piscanec, and A. C. Ferrari, "Edge-functionalized and substitutionally doped graphene nanoribbons: Electronic and spin properties," *Physical Review B*, vol. 77, p. 165427, Apr. 2008.

[113] K. Iguchi, "Dipole Moment of the HCN Molecule," *The Journal of Chemical Physics*, vol. 25, pp. 217–219, Aug. 1956.

[114] P. Hofmann, *Solid state physics: an introduction*.
John Wiley & Sons, 2015.

[115] K. Besocke, B. Krahl-Urban, and H. Wagner, "Dipole moments associated with edge atoms; A comparative study on stepped Pt, Au and W surfaces," *Surface Science*, vol. 68, pp. 39–46, Nov. 1977.

[116] N. Gonzalez-Lakunza, I. Fernández-Torrente, K. J. Franke, N. Lorente, A. Arnau, and J. I. Pascual, "Formation of Dispersive Hybrid Bands at an Organic-Metal Interface," *Physical Review Letters*, vol. 100, p. 156805, Apr. 2008.

[117] B. Biel, X. Blase, F. Triozon, and S. Roche, "Anomalous Doping Effects on Charge Transport in Graphene Nanoribbons," *Physical Review Letters*, vol. 102, p. 096803, Mar. 2009.

[118] L. Bürgi, O. Jeandupeux, A. Hirstein, H. Brune, and K. Kern, "Confinement of surface state electrons in Fabry-Pérot resonators," *Physical Review Letters*, vol. 81, no. 24, p. 5370, 1998.

[119] S. Schirone, E. Krasovskii, G. Bihlmayer, R. Piquerel, P. Gambardella, and A. Mugarza, "Spin-Flip and Element-Sensitive Electron Scattering in the BiAg 2 Surface Alloy," *Physical Review Letters*, vol. 114, p. 166801, Apr. 2015.

[120] K.-F. Braun and K.-H. Rieder, "Engineering Electronic Lifetimes in Artificial Atomic Structures," *Physical Review Letters*, vol. 88, p. 096801, Feb. 2002.

[121] G. Hadziioannou and P. F. v. Hutten, eds., *Semiconducting polymers: chemistry, physics, and engineering*.
Weinheim ; New York: Wiley-VCH, 2000.

[122] T. A. Skotheim and J. R. Reynolds, eds., *Handbook of conducting polymers. Conjugated polymers: theory, synthesis, properties, and characterization*.

Boca Raton: CRC Press, 3rd ed ed., 2007.

[123] J. Wu, W. Pisula, and K. Müllen, "Graphenes as Potential Material for Electronics," *Chemical Reviews*, vol. 107, pp. 718–747, Mar. 2007.

[124] D. Peña, "Bottom-up Approaches to Nanographenes through Organic Synthesis," in *Ideas in Chemistry and Molecular Sciences*, pp. 235–261, Wiley-VCH Verlag GmbH & Co. KGaA, 2010.
DOI: 10.1002/9783527630554.ch11.

[125] L. Chen, Y. Hernandez, X. Feng, and K. Müllen, "From Nanographene and Graphene Nanoribbons to Graphene Sheets: Chemical Synthesis," *Angewandte Chemie International Edition*, vol. 51, pp. 7640–7654, July 2012.

[126] A. Narita, X.-Y. Wang, X. Feng, and K. Mullen, "New advances in nanographene chemistry," *Chemical Society Reviews*, vol. 44, no. 18, pp. 6616–6643, 2015.

[127] Y. Segawa, H. Ito, and K. Itami, "Structurally uniform and atomically precise carbon nanostructures," *Nature Reviews Materials*, vol. 1, p. 15002, Jan. 2016.

[128] B. Schuler, S. Collazos, L. Gross, G. Meyer, D. Pérez, E. Guitián, and D. Peña, "From Perylene to a 22-Ring Aromatic Hydrocarbon in One-Pot," *Angewandte Chemie International Edition*, vol. 53, pp. 9004–9006, Aug. 2014.

[129] C. Rogers, C. Chen, Z. Pedramrazi, A. A. Omrani, H.-Z. Tsai, H. S. Jung, S. Lin, M. F. Crommie, and F. R. Fischer, "Closing the Nanographene Gap: Surface-Assisted Synthesis of Peripentacene from 6,6'-Bipentacene Precursors," *Angewandte Chemie International Edition*, vol. 54, pp. 15143–15146, Dec. 2015.

[130] H. Mönig, D. R. Hermoso, O. Díaz Arado, M. Todorović, A. Timmer, S. Schüer, G. Langewisch, R. Pérez, and H. Fuchs, "Submolecular Imaging by Noncontact Atomic Force Microscopy with an Oxygen Atom Rigidly Connected to a Metallic Probe," *ACS Nano*, vol. 10, pp. 1201–1209, Jan. 2016.

[131] N. Pavliček and L. Gross, "Generation, manipulation and characterization of molecules by atomic force microscopy," *Nature Reviews Chemistry*, vol. 1, p. 0005, Jan. 2017.

[132] E. Costa Girão, L. Liang, E. Cruz-Silva, A. G. S. Filho, and V. Meunier, "Emergence of Atypical Properties in Assembled Graphene Nanoribbons," *Physical Review Letters*, vol. 107, p. 135501, Sept. 2011.

[133] J. Liu, T. Dienel, J. Liu, O. Groening, J. Cai, X. Feng, K. Müllen, P. Ruffieux, and R. Fasel, "Building Pentagons into Graphenic Structures by On-Surface Polymerization and Aromatic Cyclodehydrogenation of Phenyl-Substituted Polycyclic Aromatic Hydrocarbons," *The Journal of Physical Chemistry C*, vol. 120, pp. 17588–17593, Aug. 2016.

[134] G. Otero, G. Biddau, C. Sánchez-Sánchez, R. Caillard, M. F. López, C. Rogero, F. J. Palomares, N. Cabello, M. A. Basanta, J. Ortega, J. Méndez, A. M. Echavarren, R. Pérez, B. Gómez-Lor, and J. A. Martín-Gago, "Fullerenes from aromatic precursors by surface-catalysed cyclodehydrogenation," *Nature*, vol. 454, pp. 865–868, Aug. 2008.

[135] H. Terrones, M. Terrones, E. Hernández, N. Grobert, J. C. Charlier, and P. M. Ajayan, "New metallic allotropes of planar and tubular carbon," *Physical Review Letters*, vol. 84, no. 8, p. 1716, 2000.

[136] J. Ma, D. Alfè, A. Michaelides, and E. Wang, "Stone-Wales defects in graphene and other planar sp^2 -bonded materials," *Physical Review B*, vol. 80, p. 033407, July 2009.

[137] Q. Fan, C. Wang, Y. Han, J. Zhu, W. Hieringer, J. Kuttner, G. Hilt, and J. M. Gottfried, "Surface-Assisted Organic Synthesis of Hyperbenzene Nanotroughs," *Angewandte Chemie International Edition*, vol. 52, pp. 4668–4672, Apr. 2013.

[138] M. Chen, J. Shang, Y. Wang, K. Wu, J. Kuttner, G. Hilt, W. Hieringer, and J. M. Gottfried, "On-Surface Synthesis and Characterization of Honeycombene Oligophenylene Macrocycles," *ACS Nano*, vol. 11, pp. 134–143, Jan. 2017.

[139] M. Treier, C. A. Pignedoli, T. Laino, R. Rieger, K. Müllen, D. Passerone, and R. Fasel, "Surface-assisted cyclodehydrogenation provides a synthetic route towards easily processable and chemically tailored nanographenes," *Nature Chemistry*, vol. 3, pp. 61–67, Jan. 2011.

[140] E. Cockayne, G. M. Rutter, N. P. Guisinger, J. N. Crain, P. N. First, and J. A. Stroscio, "Grain boundary loops in graphene," *Physical Review B*, vol. 83, p. 195425, May 2011.

[141] H. I. Rasool, E. B. Song, M. Mecklenburg, B. C. Regan, K. L. Wang, B. H. Weiller, and J. K. Gimzewski, "Atomic-Scale Characterization of Graphene Grown on Copper (100) Single Crystals," *Journal of the American Chemical Society*, vol. 133, pp. 12536–12543, Aug. 2011.

[142] F. Banhart, J. Kotakoski, and A. V. Krasheninnikov, "Structural Defects in Graphene," *ACS Nano*, vol. 5, pp. 26–41, Jan. 2011.

[143] L. P. Biró and P. Lambin, "Grain boundaries in graphene grown by chemical vapor deposition," *New Journal of Physics*, vol. 15, p. 035024, Mar. 2013.

[144] O. V. Yazyev and Y. P. Chen, "Polycrystalline graphene and other two-dimensional materials," *Nature Nanotechnology*, vol. 9, pp. 755–767, Aug. 2014.

[145] Y. Pennec, W. Auwärter, A. Schiffrin, A. Weber-Bargioni, A. Riemann, and J. V. Barth, "Supramolecular gratings for tuneable confinement of electrons on metal surfaces," *Nature Nanotechnology*, vol. 2, pp. 99–103, Feb. 2007.

[146] J. Lobo-Checa, M. Matena, K. Muller, J. H. Dil, F. Meier, L. H. Gade, T. A. Jung, and M. Stohr, "Band Formation from Coupled Quantum Dots Formed by a Nanoporous Network on a Copper Surface," *Science*, vol. 325, pp. 300–303, July 2009.

[147] F. Klappenberger, D. Kühne, W. Krenner, I. n. Silanes, A. Arnau, F. J. García de Abajo, S. Klyatskaya, M. Ruben, and J. V. Barth, "Dichotomous Array of

Chiral Quantum Corrals by a Self-Assembled Nanoporous Kagomé Network," *Nano Letters*, vol. 9, pp. 3509–3514, Oct. 2009.

[148] M. Feng, J. Zhao, T. Huang, X. Zhu, and H. Petek, "The Electronic Properties of Superatom States of Hollow Molecules," *Accounts of Chemical Research*, vol. 44, pp. 360–368, May 2011.

[149] M. Feng, J. Zhao, and H. Petek, "Atomlike, Hollow-Core-Bound Molecular Orbitals of C_{60}," *Science*, vol. 320, p. 359, Apr. 2008.

[150] J. Zhao, M. Feng, J. Yang, and H. Petek, "The Superatom States of Fullerenes and Their Hybridization into the Nearly Free Electron Bands of Fullerites," *ACS Nano*, vol. 3, pp. 853–864, Apr. 2009.

Publications

Quantum Dots Embedded in Graphene Nanoribbons by Chemical Substitution
E. Carbonell-Sanromà, P. Brandimarte, M. Corso, S. Kawai, A. García-Lekue, S. Saito, S. Yamaguchi, E. Meyer, D. Sánchez-Portal and J.I. Pascual.
Nanoletters, **17**, 50-56 (2016)

Doping of Graphene Nanoribbons via Functional Group Edge Modification
E. Carbonell-Sanromà, J. Hieulle, M. Vilas-Varela, P. Brandimarte, M. Iraola, A. Barragán, J. Li, M. Abadia, M. Corso, D. Sánchez-Portal, D. Peña and J.I. Pascual.
submitted, arXiv:1705.07045

Substrate-Independent Growth of Atomically Precise Chiral Graphene Nanoribbons
D.G. de Oteyza, A. García-Lekue, M. Vilas-Varela, Merino-Díez, E. Carbonell-Sanromà, M. Corso, G. Vasseur, C. Rogero, E. Guitián, J.I. Pascual, J.E. Ortega, Y. Wakayama and D. Peña.
ACS Nano, **10**, 9000-9008 (2016)

Acknowledgments

Writing this final chapter is possible because of the many people that helped, encouraged and supported me during these thesis years. It's difficult to put so many emotions and feelings into words but its the least I can do to show my gratitude to everyone who has stood by me.

First of all I want to thank Nacho Pascual, who has shared with me so much of his knowledge. For giving me this opportunity and for showing me that the impossible can become possible through force of will and effort (sometimes!).

To Richard, who taught me so much during the most difficult moments of this journey. For teaching me no question is stupid. For all the coffees shared and the good laughs at the lab. Saying thank you is not enough but...Thank you so much!

To Martina, for her helping hand, her counsel and her positive attitude at all times. You have always been there when I needed a pinch of your optimism.

To my little PhD sister Carmen, for all the absurd laughs, funny moments and your friendship inside and outside our labs. For all our shed tears, discussions and her never-ending support. This ride would have been really boring without you!

To Li for teaching me all about Milano when I just arrived, always with a smile. And for coming back later so I could show him he did great! To Jeremy, for his drive and calm during the last year of the thesis. To Zsolt and David for all their help with all sorts of technical problems and being patient whenever I nagged at them again and again. To Miguel and Reyes for the all the gin tonics vanidosos we had and to Javi for his helping hand at all times. To Pedro and Aran who were so patient with me no matter how many times I asked them about their DFT thingies!

To Juan and Saul, my flatmates, with whom I shared laughs, all sorts of good and bad moments and lots of hours of geekiness. For all their counsels and experiences that helped me through my PhD. To all the nice people in nanoGUNE, who always managed to make me smile, Álvaro, Mikel, Jon, Santi, Ilargi, Maria and Oihana and many others.

A la Mireia, per haver estat al meu costat sempre que l'he necessitat i haver-me aguantat en els meus pitjors moments. Per haver estat la meva companya de viatge aquests 4 anys. A la meva mare, per donar-me forces quan ja no me'n quedaven, per donar-me calma i empenta. Al meu pare, per escoltar-me sempre que ho necessitava i per recordar-me que sempre, sempre, hi ha una llumeta al final del túnel. I al meu germá, per tot el seu suport i el seu punt de vista optimista en els moments més durs.

MOLTES GRÀCIES A TOTS!